Department of Physics and Astronomy

University of Heidelberg

Master thesis

in Physics

submitted by

Paulus Salomon Bauer

born in Salzburg

2013

Development of an imaging polarimeter for water wave slope measurements

This Master thesis has been carried out by Paulus Salomon Bauer

at the

Institute of Environmental Physics

under the supervision of

Prof. Dr. Bernd Jähne

Abstract:

An imaging polarimetric slope sensing instrument for measuring water waves has been developed. From the measurement of the intensities of three different linear polarization states, it is possible to determine the first three components of the polarization Stokes vector. The slope of the water surface is computed from the measurement of the polarization of reflected light. Unlike in common polarimeters, custom optics are not required in this simple setup consisting of three cameras aligned in parallel and each equipped with a standard polarization filter. The trade-off for the simple setup is the need for more extensive system calibration and image post-processing. The camera setup was fully calibrated (extrinsic, intrinsic, and distortion parameters) with a specialized calibration procedure using a custom built target. The analyzer matrix, which transforms the intensities of the measured polarization states into the Stokes vector components was determined and verified experimentally. A data set collected during an experiment on board the research vessel Meteor is analyzed. In an experiment at the Hamburgische Schiffsbau-Versuchsanstalt, the polarimeter was successfully operated under laboratory conditions. It is shown to be capable of measuring the slope distribution of mechanically generated waves. Elevation power spectra, determined by integration of the slope measurements, show good agreement with reference measurements with a wave wire. Deviations at low wave frequencies due the small size of the polarimeter footprint can be compensated with a transfer function that is derived from the measurements.

Zusammenfassung:

Ein bildgebendes polarimetrisches Instrument zur Messung der Neigung von Wasserwellen wurde entwickelt. Aus der Messung von drei linearen Polarisationszuständen werden die ersten drei Komponenten des Stokes-Vektors bestimmt. Die Neigung der Wasseroberfläche wird aus der Messung der Polarisation von reflektiertem Licht berechnet. Im Gegensatz zu herkömmlichen Polarimetern werden keine spezialisierten optischen Elemente benötigt, es kommt ein einfacher Aufbau aus drei parallel angeordneten Kameras mit Polarisationsfiltern zum Einsatz. Ein Mehraufwand in der Kalibrierung und Bildverarbeitung wird dabei in Kauf genommen. Der Kamera-Aufbau wurde mit einer dafür entwickelten Methode und einem eigens angefertigten Kalibriertarget kalibriert (extrinsische, intrinsische und Verzerrungs-Parameter). Die Analyse-Matrix, die die gemessenen Polarisationszustände in die Komponenten des Stokes-Vektors überführt, wurde bestimmt und experimentell verifiziert. Ein Datensatz, der während eines Experiments an Bord des Forschungsschiffs Meteor aufgenommen wurde, wurde analysiert. In einem Experiment an der Hamburgische Schiffsbau-Versuchsanstalt wurde das Polarimeter erfolgreich unter Laborbedingungen eingesetzt. Seine Fähigkeit, die Neigungsverteilung mechanisch erzeugter Wellen zu messen, wird demonstriert. Aus der Integration der Neigungsmessungen gewonnene Wellenhöhen-Leistungsspektren stimmen gut mit Referenzmessungen mit einem Wellendraht überein. Abweichungen, die bei niedrigen Frequenzen durch die kleine Größe des Polarimeter-Messfelds auftreten, können durch eine experimentell bestimmte Transferfunktion korrigiert werden.

Contents

1. Introduction

Figure 1.1.: The blue marble, earth. Source: NASA http://visibleearth.nasa.gov/view.php?id=57723

From a satellite's view, Earth seems to be a beautiful blue marble. This is because about 71 percent of the Earth are covered with water. The vast ocean not only determines the color of our planet but also influences the climate of the Earth in a profound way[1].

Especially the exchange of gases, momentum, heat and energy between ocean and atmosphere plays an important role for our climate. This can be exemplarily depicted by the uptake of 30-40% of the anthropogenic CO_2 (Donelan and Wanninkhof, 2002). Even after decades of intensive research, the exchange processes and its physical parametrization are still not fully understood. It was pointed out that the near-surface turbulence has a significant influence on the exchange processes (Frew et al., 2004). The mean squared slope, which is a measurement for small scale waves, describes the near-surface turbulence (Jähne et al., 1987). Hence, the simultaneous acquisition of wave and gas exchange data is necessary to obtain a physically based parametrization of the exchange processes.

Traditional instruments exist, like wave wires (Donelan et al., 1985) or floating buoys (Longuet-Higgins et al., 1963), measuring the elevation of the water surface, which is useful for swell and long wind waves. To resolve the small scale waves, which have a small amplitude and are superimposed on the large scale waves, an amplitude measurement technique must have a high dynamic range. The preferred solution is to measure the slope of the surface, since the slope has a much smaller dynamic range due to the wave breaking of steep waves.

[1] NASA Ocean Motion: http://oceanmotion.org/html/background/climate.htm
Surface Ocean Lower Atmosphere Study (SOLAS): http://www.solas-int.org

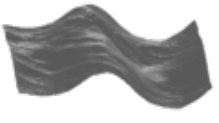

In the laboratory, the slope of small scale waves can be measured with high temporal and spatial resolution using an imaging slope gauge (ISG, Rocholz (2008)). This instrument can measure the slope of the surface from the refraction of light coming from an underwater light source. For field measurements, installing a light source underwater is often not feasible. Thus, it is more convenient to use light that is reflected at the water surface for the measurements. Stilwell (1969) developed a measurement technique that relies on the dependence of the reflection coefficient on the incidence angle of light (known as *Stilwell photography*). This method has strong limitations because it requires very homogeneous illumination. Furthermore, the relation between the slope and the intensity of the reflected light is highly nonlinear (Jähne et al., 1994).

Another approach that overcomes many problems of the Stilwell photography does not rely on the intensity of the reflected light, but measures its polarization state (Zappa et al., 2008). This has two significant advantages: First, the dependence of the used polarization measures (degree of linear polarization and orientation of polarization) on the incidence angle is not as nonlinear as the reflected intensity. Second, the measurements are based on the ratio of measured intensities. This makes the measurement independent of inhomogeneities in the illumination.

Studies that have applied polarimetric slope sensing to small scale water waves so far used very expensive instruments including custom lenses and complex optical setups containing polarizing beam splitters (Pezzaniti et al., 2008, 2009; Zappa et al., 2012). While this is an elegant solution, it is also very expensive.

For this work, a new approach to an imaging polarimeter was tested, using three cameras placed next to each other. Each camera is equipped with a standard polarization filter, which makes the whole setup quite cheap. The disadvantage of this setup is a larger necessity of profound image processing. The aim of this thesis was to build the newly designed polarimeter, to calibrate the whole system, to develop a data processing structure and to characterize its performance.

2. Theory

2.1. The electrodynamics of continuous media

2.1.1. Maxwell's equations

The basic principles of optics and phenomena of the electromagnetic field is, except of quantum effects, completely described by the Maxwell's equation along with the Lorentz's equation. Hence, to get a deeper understanding of the interaction between light and matter and the polarization of light, some general entities of electrodynamics will be stated or derived in the next sections. But first and foremost the Maxwell's equations will be stated in a general form, independent of the choice of the electrodynamic units.

Homogeneous equations

$$\nabla \cdot \boldsymbol{B} = 0 \tag{2.1}$$

which equals to, that there are no magnetic monopoles.

$$\nabla \times \boldsymbol{E} + \frac{\partial \boldsymbol{B}}{\partial t} = 0 \tag{2.2}$$

which correspond to Faraday's law of induction.

Inhomogeneous equations

$$\nabla \cdot \boldsymbol{E} = \frac{\rho}{\varepsilon_0} \tag{2.3}$$

which relate to to the divergence theorem (or Gauss's theorem).

$$\nabla \times \boldsymbol{B} - \mu_0 \varepsilon_0 \frac{\partial \boldsymbol{E}}{\partial t} = \mu_0 \boldsymbol{j} \tag{2.4}$$

which is equal to Ampère's circuital law with Maxwell's correction.

Together with the Lorentz-force

$$\boldsymbol{F}_L = q \cdot [\boldsymbol{E} + (\boldsymbol{v} \times \boldsymbol{B})] \tag{2.5}$$

Maxwell's equations gather all classical phenomena of the electromagnetic interactions in vacuum. Here, $\boldsymbol{E}$ denotes the *electric field vector*, $\boldsymbol{B}$ the *magnetic induction vector*, ρ the *electric charge density*, $\boldsymbol{j}$ the *electric current density*, ε_0 the permittivity of vacuum, μ_0 the permeability of vacuum and q the electrical charge of the particle, on which the electromagnetic field is acting.

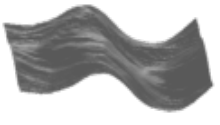

2.1.2. The electromagnetic wave equations or Light

In vacuum there is neither an electric charge density $\rho = 0$ nor any electrical current density $\boldsymbol{j} = 0$. So Maxwell's equations look like this:

$$\nabla \cdot \boldsymbol{E} = 0; \qquad \nabla \cdot \boldsymbol{B} = 0; \qquad \nabla \times \boldsymbol{E} = -\frac{\partial \boldsymbol{B}}{\partial t}; \qquad \nabla \times \boldsymbol{B} = \varepsilon_0 \mu_0 \frac{\partial \boldsymbol{E}}{\partial t} \tag{2.6}$$

These partial differential equations can be decoupled by some vectorial identities, which is shown in many textbooks[1] and give as result the homogeneous wave equation for the E-filed as well for the B-field.

$$\left(\frac{1}{c_0^2} \frac{\partial^2}{\partial t^2} - \nabla^2 \right) \boldsymbol{E} = \Box \boldsymbol{E} = 0 \qquad \text{with} \qquad \frac{1}{c_0^2} = \varepsilon_0 \mu_0 \tag{2.7}$$

where $\Box$ is the *d'Alembert-Operator* and c_0 is the speed of light in vacuum. With these substitutions, equations (2.6) reduce to:

$$\begin{aligned} \Box \boldsymbol{E} &= 0 & \nabla \cdot \boldsymbol{E} &= 0 \\ \Box \boldsymbol{B} &= 0 & \nabla \cdot \boldsymbol{B} &= 0 \end{aligned} \tag{2.8}$$

The solution to these equations is given by a plane wave.

$$\boldsymbol{E}(\boldsymbol{x}, t) = \Re\left(\boldsymbol{E}_0 \exp(i(\boldsymbol{k} \cdot \boldsymbol{x} - \omega t)) \right) \tag{2.9}$$

$$\boldsymbol{B}(\boldsymbol{x}, t) = \Re\left(\boldsymbol{B}_0 \exp(i(\boldsymbol{k} \cdot \boldsymbol{x} - \omega t)) \right) \tag{2.10}$$

Here $\Re$ denotes the real part of the solution and $\boldsymbol{k}$ and ω the wave vector and the angular frequency respectively.

Properties of the wave solution

This section shows some important properties of the wave solution which will be used in further derivations.

Dispersion relation The dispersion relation is one of the easiest to derive. Inserting Eq. (2.9) into the Eq. (2.7), the dispersion relation in vacuum gives

$$\omega^2 = k^2 c_0^2, \tag{2.11}$$

where $k = |\boldsymbol{k}|$.

Transversality of electromagnetic waves From $\nabla \cdot \boldsymbol{E} = 0$ and Eq. (2.9) we obtain

$$\boldsymbol{k} \cdot \boldsymbol{E} = 0 \tag{2.12}$$

and the same for $\boldsymbol{B}$. This means the field vectors $\boldsymbol{E}$ and $\boldsymbol{B}$ are transversal to the propagation direction $\boldsymbol{k}$.

Orthogonality of $\boldsymbol{E}$ and $\boldsymbol{B}$ From the wave solution Eq. (2.9) and from the Maxwell equation

$$\nabla \times \boldsymbol{E} = -\frac{\partial \boldsymbol{B}}{\partial t} \tag{2.13}$$

[1] recommended textbook Jackson (1998)

follows

$$\boldsymbol{k} \times \boldsymbol{E} = \omega \boldsymbol{B} \tag{2.14}$$

This means that $\boldsymbol{E} \perp \boldsymbol{B}$ and $\boldsymbol{E}$,$\boldsymbol{B}$ and $\boldsymbol{k}$ span an orthogonal coordinate system. The normalization of $\boldsymbol{E}$ and $\boldsymbol{B}$ are fixed through this equation as well:

$$|\boldsymbol{B}| = |\boldsymbol{E}|/c_0 \tag{2.15}$$

2.1.3. Electromagnetic fields in matter

In principle, it is possible to use the same equations as in Sec. 2.1.1 to calculate the electromagnetic field in any kind of material composition. Because this assignment is linked to a huge computational effort we will just consider temporal and spatial averages of the field, which is then called the macroscopic view. The effort to compute a microscopic solution is as well not necessary for most experiments, since in the laboratory it is only possible to control temporal and spatial averages of the field. Hence we have to distinguish between the microscopic field and the macroscopic (average) field[2].
Another simplification is that we will only examine linear and isotropic optical materials, where the *electric displacement density* $\boldsymbol{D}$ and the *magnetic field vector* $\boldsymbol{H}$ are proportional to $\boldsymbol{E}$ and $\boldsymbol{B}$. We define $\boldsymbol{D}$ and $\boldsymbol{H}$ as:

$$\boldsymbol{D} = \varepsilon_r \varepsilon_0 \boldsymbol{E} = \varepsilon \boldsymbol{E} \tag{2.16}$$

$$\boldsymbol{H} = \frac{\boldsymbol{B}}{\mu_r \mu_0} = \frac{\boldsymbol{B}}{\mu} \tag{2.17}$$

Here ε is the *permittivity* and μ is the *permeability* of the material (ε_r and μ_r are called *relative permittivity* and *relative permeability* respectively).
With these new fields we can rewrite the Maxwell equations as:

Homogeneous Equations

$$\nabla \cdot \boldsymbol{B} = 0 \qquad\qquad \nabla \times \boldsymbol{E} + \frac{\partial \boldsymbol{B}}{\partial t} = 0 \tag{2.18}$$

Inhomogeneous Equations

$$\nabla \cdot \boldsymbol{D} = \rho_f \qquad\qquad \nabla \times \boldsymbol{H} - \frac{\partial \boldsymbol{D}}{\partial t} = \boldsymbol{j}_f \tag{2.19}$$

As one can see, there is no change in the homogeneous equations (Eq. (2.18)) since the properties of the matter have no influence on them, but the inhomogeneous equations have changed. Here ρ_f and $\boldsymbol{j}_f$ denote the *electric charge density* and the *electric current density* of the free charge carrier. The bound charge carrier are polarized by the field, which is included in the $\boldsymbol{D}$- and $\boldsymbol{H}$-field, by the *relative permittivity* ε_r and the *relative permeability* μ_r. Another note is that $\boldsymbol{E}$- and $\boldsymbol{B}$-field are defined asymmetric, as in Eq. (2.16) and (2.17) shows (ε is in the nominator and μ is in the denominator). This unluckily seeming cause has a practical meaning, that in experiments it is easier to control the $\boldsymbol{E}$- and $\boldsymbol{H}$-field, which are the two independent fields.

[2] There will be no change in notation between the microscopic field labels of Sec. 2.1.1 and the macroscopic field labels of this section, even if the latter one is averaged over time and space

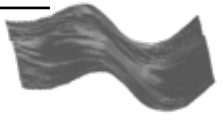

2.1.4. Electromagnetic Fields at a boundary

Because we want to deal with at least two different materials, it is not enough to know what happens inside these two materials (which is given by the equations of Sec. 2.1.3), but as well to understands the effects of the boundary. The most interesting question at a boundary is, which component of the field is continuous. Therefore we will first investigate the homogeneous equations (Eq. (2.18)) at a boundary. With the *divergence theorem* and $\nabla \cdot \boldsymbol{B} = 0$ it is possible to show that the normal component of $\boldsymbol{B}_n$ is continuous at a boundary. With *Stokes' theorem* we can find out from the second homogeneous equation that the tangential component $\boldsymbol{E}_t$ is continuous there.
The same can be done with the inhomogeneous equations (Eq. (2.19)) by using these two theorems. Thus, we get

$$(\boldsymbol{D}_n^{(1)} - \boldsymbol{D}_n^{(2)}) = \gamma_f \qquad \boldsymbol{n} \times (\boldsymbol{H}_t^{(1)} - \boldsymbol{H}_t^{(2)}) = \boldsymbol{i}_f \tag{2.20}$$

where the subscript $_{n,t}$ denote the normal or tangential component, $\boldsymbol{n}$ the normal vector of the surface, γ_f and $\boldsymbol{i}_f$ the *free surface charge* and the *free surface current* respectively of the two materials.

2.1.5. Electromagnetic Fields in Dielectric Materials

In nature, we can sort materials roughly in conductors and isolators (also called dielectric materials). Because conductors are not transparent and act mostly as a mirror, the main focus in optics is on dielectric materials. What is so special about them? A dielectric material can be a gas, a fluid or a solid, in which all charge carriers are normally fixed and therefore can't move. This has as consequence:

$$\rho_f = 0 \quad \Rightarrow \quad \gamma_f = 0 \quad \text{and} \quad \boldsymbol{j}_f = 0 \quad \Rightarrow \quad \boldsymbol{i}_f = 0 \tag{2.21}$$

This means that at the boundary of a dielectric material the normal component of the $\boldsymbol{B}$- and $\boldsymbol{D}$-field and the tangential component of the $\boldsymbol{E}$- and $\boldsymbol{H}$-field are continuous. The continuity is formulated mathematically like this

$$\boldsymbol{n} \cdot \boldsymbol{B} \qquad \boldsymbol{n} \cdot \boldsymbol{D} \qquad \boldsymbol{n} \times \boldsymbol{E} \qquad \boldsymbol{n} \times \boldsymbol{H} \tag{2.22}$$

where $\boldsymbol{n}$ is the normal vector to the surface area.
Another interesting property of dielectric materials is, that they are normally not magnetic. This means that we can ignore the *permeability* and set $\mu_r = 1$.

2.1.6. Electromagnetic Waves in Matter

If the macroscopic field equations of Sec. 2.1.3 are combined with the knowledge of Sec. 2.1.5 (especially Eq. (2.21)), the solution looks much like the microscopic wave equation Eq. (2.6) in vacuum of Sec. 2.1.2. Thus, after some decoupling of the equations they are written like this:

$$\begin{aligned} \Box \boldsymbol{E} &= 0 & \Box \boldsymbol{D} &= 0 & \nabla \cdot \boldsymbol{D} &= 0 \\ \Box \boldsymbol{B} &= 0 & \Box \boldsymbol{H} &= 0 & \nabla \cdot \boldsymbol{B} &= 0 \end{aligned} \tag{2.23}$$

As mentioned in Sec. 2.1.3, we are mostly interested in $\boldsymbol{E}$- and $\boldsymbol{H}$ fields. Therefore we will only use these two fields in our further considerations. The solution of the wave equation in matter for $\boldsymbol{E}$ and $\boldsymbol{H}$ is

$$\boldsymbol{E}(\boldsymbol{x}, t) = \Re\left(\boldsymbol{E}_0 \exp(i(\boldsymbol{k} \cdot \boldsymbol{x} - \omega t))\right) \tag{2.24}$$

$$\boldsymbol{H}(\boldsymbol{x}, t) = \Re\left(\boldsymbol{H}_0 \exp(i(\boldsymbol{k} \cdot \boldsymbol{x} - \omega t))\right) \tag{2.25}$$

The waves have the same properties as discussed in Sec. 2.1.2. Especially the **transversality** and the **orthogonality of $\boldsymbol{E}$ and $\boldsymbol{H}$** stay the same. These two properties will be important for the polarization of light (Sec. 2.2) and for the Fresnel equations (Sec. 2.3). The **dispersion relation** will be used in the next section.

Phase and Group velocity

As we have seen in Sec. 2.1.2 in Eq. (2.7), a phase velocity is already included in the *d'Alembert-Operator*. For a macroscopic field in matter this velocity cannot be the same as the speed of light in vacuum c_0. The easiest way to get the phase velocity is to use the dispersion relation, like Eq. (2.11), by reinserting Eq. (2.24) into Eq. (2.23).

$$v_{\mathrm{ph}}(\omega) = c(\omega) = \frac{\omega}{k} = \frac{1}{\sqrt{\varepsilon\mu}} = \frac{1}{\sqrt{\varepsilon_r\mu_r\varepsilon_0\mu_0}} = \frac{c_0}{n(\omega)} \tag{2.26}$$

Here we have introduced the **index of refraction** $n = \sqrt{\varepsilon_r\mu_r}$, which is normally frequency dependent, since ε_r and μ_r dependent on the frequency. This effect is also called dispersion and is responsible for such nice effects like a rainbow. Because ε_r and μ_r are in general complex, the refection index can as well be complex. The imaginary part of the refraction index is representing a damping of the electromagnetic wave amplitude in the material. The imaginary part is important for opaque materials and metals, which we will not consider here any further.
The phase velocity can even get higher than the velocity of light in vacuum ($c > c_0$), which stands not in conflict with the theory of relativity. This is because the energy and the information is transported with the group velocity v_{gr}:

$$v_{\mathrm{gr}}(\omega) = \left(\frac{d\omega}{dk}\right)_{k=k_0} \tag{2.27}$$

2.1.7. Energy density, Pointing Vector and Intensity

One of the most important properties of the electromagnetic field or of light is the transport of energy. The derivation of the *energy density* E and the *Pointing Vector* $\boldsymbol{S}$ is as well given in many textbooks (Jackson, 1998). They are given by

$$\text{Engergy density:} \qquad \mathsf{E} = \frac{1}{2}(\boldsymbol{E}\cdot\boldsymbol{D} + \boldsymbol{B}\cdot\boldsymbol{H}) \tag{2.28}$$

$$\text{Pointing vector:} \qquad \boldsymbol{S} = (\boldsymbol{E}\times\boldsymbol{H}) \tag{2.29}$$

The pointing vector $\boldsymbol{S}$ can as well be regarded as the *energy flux density* of the *energy conservation equation*.

$$\frac{\partial \mathsf{E}}{\partial t} + \nabla\cdot\boldsymbol{S} = 0 \tag{2.30}$$

The pointing vector plays another important role for the measurement of electromagnetic waves, because it is only possible to measure the energy deposit. Therefore the definition of the intensity comes up.

$$I[\mathrm{W\,m^{-2}}] = \langle|\boldsymbol{S}|\rangle = \varepsilon_0 nc\langle|\boldsymbol{E}|^2\rangle \qquad \text{EM-wave: } I = \frac{1}{2}\varepsilon_0 nc|E_0|^2 \tag{2.31}$$

where $\langle\,\rangle$ denotes the temporal mean over one period T.

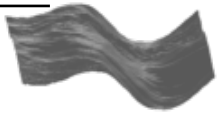

2.2. Polarization of Light

Due to the *orthogonality of* $\boldsymbol{E}$ *and* $\boldsymbol{H}$ of electromagnetic waves (Sec. 2.1.2 and Sec. 2.1.6, Eq. (2.14)) it is only necessary to consider one field, which will be the $\boldsymbol{E}$-field in our case. Without loss of generality we can choose $\boldsymbol{k}$ to go into z-direction and therefore the *transversality* of EM-waves ($\boldsymbol{k} \cdot \boldsymbol{E} = 0$) states that the $\boldsymbol{E}$ must lie in the x, y-plane. Without loss of generality we can write the solution to the wave equation Eq. (2.24) as such:

$$\boldsymbol{E} = \boldsymbol{E}_x + \boldsymbol{E}_y = \begin{bmatrix} E_{\mathrm{x0}} \cos(kz - \omega t) \\ E_{\mathrm{y0}} \cos(kz - \omega t + \varphi) \\ 0 \end{bmatrix} \tag{2.32}$$

where $E_{\mathrm{x0}}, E_{\mathrm{y0}}$ are the amplitudes of the $\boldsymbol{E}$-field in x, y-direction and φ is a phase factor between the x, y-component. The different configuration of these factors ($E_{\mathrm{x0}}, E_{\mathrm{y0}}, \varphi$) give the different types of polarization, which will be explained subsequently.

2.2.1. The polarization ellipse

The trace of the $\boldsymbol{E}$-vector over time at a certain x, y-plane (where $z = z_0$) describes an ellipse. This can easily be seen if we use some trigonometric function identities and combining the $E_x(t)$ and $E_y(t)$ component of the $\boldsymbol{E}$-field. After some mathematical manipulation the equation of the *polarization ellipse* arise (see Schott (2009), Brosseau (1998)).

$$\frac{E_x^2}{E_{\mathrm{x0}}^2} + \frac{E_y^2}{E_{\mathrm{y0}}^2} - 2\frac{E_x E_y}{E_{\mathrm{x0}} E_{\mathrm{y0}}} \cos\varphi = \sin^2\varphi \tag{2.33}$$

An illustration of the polarization ellipse is shown in Fig. 2.1.

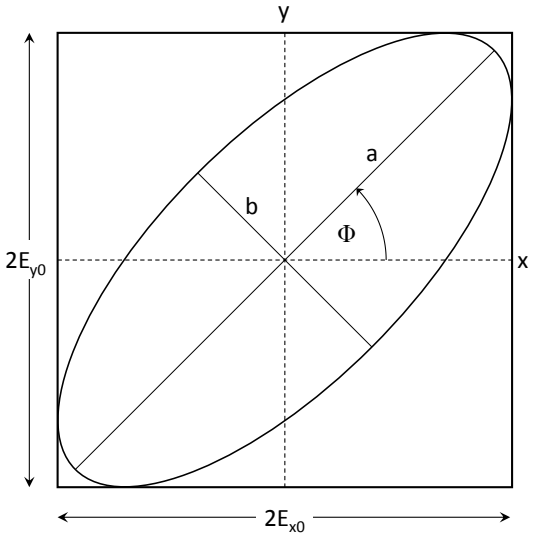

Figure 2.1.: Illustration of the polarization ellipse with the polarization angle Φ

Equation (2.33) is the general equation of an ellipse, which is rotated by an angle Φ, where

$$\tan 2\Phi = \frac{2E_{\mathrm{x0}} E_{\mathrm{y0}} \cos\varphi}{E_{\mathrm{x0}}^2 - E_{\mathrm{y0}}^2} \tag{2.34}$$

Even more generally, the amplitude of $\boldsymbol{E}$ as well as the phase difference (and hence also the angle Φ) can change over time. This means that the *polarization ellipse* starts to rotate over time.

Another aspect of the propagation of elliptical EM-waves is not covered with the above equations, which is the left- or right-handedness of the rotation. As neither elliptical nor circular polarization is relevant in this thesis, this topic will not be considered in detail further.
Some special cases of the *elliptical polarization* are the *linear polarization* and the *circular polarization*.

Linear Polarization

Linear polarization is a special case of the elliptical polarization, where the phase shift φ between the E_x and E_y components is an integer multiple of π. ($\varphi = n \cdot \pi; n \in \mathbb{N}$). This means that the $\boldsymbol{E}$-field oscillates only in one plane. Therefore it is called *plane* or *linear polarization*. If we look at the two cases of $\varphi = 0$ or π we can write E_y

$$E_y = \frac{E_{y0}}{E_{x0}} E_x \text{ for } \phi = 0, \qquad E_y = -\frac{E_{y0}}{E_{x0}} \text{ for } \phi = \pi \tag{2.35}$$

This is a line with zero intercept and a slope of E_{y0}/E_{x0} and we can derive Φ from the slope by

$$\tan\Phi = \frac{E_{y0}}{E_{x0}} \tag{2.36}$$

which corresponds to a simplification of equation (2.34).
Since linear polarization is the most common form of polarized light in nature, we will mainly concentrate on this in the next chapters.

Circular Polarization

Circular polarization is as well a special case of the elliptical polarization, where the phase shift between the two $\boldsymbol{E}$-vector components is $\varphi = \frac{2\cdot n+1}{2}\pi; n \in \mathbb{N}$ and the amplitudes are equal $E_{x0} = E_{y0} = E_0$. Hence the ellipse equation (2.33) reduces to:

$$\frac{E_x^2}{E_0^2} + \frac{E_y^2}{E_0^2} = 1 \tag{2.37}$$

which is a circle equation.

2.2.2. Stokes Vector

There are many ways to introduce the Stokes vector (see Jackson (1998), Brosseau (1998), Videen et al. (2005)). But the easiest way, in my opinion, is described by Schott (2009), which we will follow. The Stokes parameters are one of the most important concepts in this work because they are easy to measure as we will see later and they describe also partly polarized light. An unpolarized light ray has no distinct polarization state, which means that it consist of many EM-waves with all kinds of polarization. A partial polarized light is then a light ray which has one favored polarization state, but there are as well other ones included in the ray.
To derive the Stokes parameter we start out with the equation of the elliptical polarization Eq. (2.33), taking the time average over one period and taking the square as for the intensity Eq. (2.31). This gives after some mathematical reformulation:

$$(E_{x0}^2 + E_{y0}^2)^2 = (E_{x0}^2 - E_{y0}^2)^2 + (2E_{x0}E_{y0}\cos\varphi)^2 + (2E_{x0}E_{y0}\sin\varphi)^2 \tag{2.38}$$

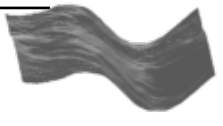

As we can see here, there are four important terms, which we will define as the Stokes parameters:

$$S_0 = E_{x0}^2 + E_{y0}^2 \tag{2.39}$$

$$S_1 = E_{x0}^2 - E_{y0}^2 \tag{2.40}$$

$$S_2 = 2E_{x0}E_{y0}\cos\varphi \tag{2.41}$$

$$S_3 = 2E_{x0}E_{y0}\sin\varphi \tag{2.42}$$

The first parameter S_0 is the easiest to interpret, since it is the squared norm of the $\boldsymbol{E}$-vector of Eq. (2.32), were the time average is already taken. Hence we can conclude from Eq. (2.31), that this parameter represents the total intensity of the light ray. The second parameter S_1 becomes clear, if we consider only horizontal or vertical polarized light, where only E_{x0} or E_{y0} exists, respectively. Thus the second parameter represents these polarization states. S_2 describes the polarization in ±45°-direction and last but not least S_3 stand for the amount of left- and right-handed polarization. (For further understanding of the parameters have a look at the definition of the different polarization states in Sec. 2.2.1 or in the book Schott (2009).)
If we use now the definition of the Stokes parameters Eq. (2.39) and Eq. (2.38) we can derive a very important property of the Stokes parameters:

$$S_0^2 = S_1^2 + S_2^2 + S_3^2 \tag{2.43}$$

This equation is only valid if the light ray is fully polarized, which is not true for most cases. Due to the fact that S_0 represents the total energy of the ray, the right hand part of Eq. (2.43) cannot become larger than S_0 because of energy conservation. Thus a partly polarized ray is characterized by

$$S_0^2 > S_1^2 + S_2^2 + S_3^2 \tag{2.44}$$

Another property of polarized light can be expressed by the Stokes parameters, namely the *polarization angle* Φ, which is defined in Eq. (2.34).

$$\tan 2\Phi = \frac{2E_{x0}E_{y0}\cos\varphi}{E_{x0}^2 - E_{y0}^2} = \frac{S_2}{S_1} \qquad \Rightarrow \qquad \Phi = \frac{1}{2}\tan^{-1}\left(\frac{S_2}{S_1}\right) \tag{2.45}$$

The Stokes parameters are often arranged in vector form. This vector has no directional meaning, but the convenience of this representation becomes clear in the next section (Sec. 2.2.3)).

$$\boldsymbol{S} = \begin{bmatrix} S_0 \\ S_1 \\ S_2 \\ S_3 \end{bmatrix} = \begin{bmatrix} E_{x0}^2 + E_{y0}^2 \\ E_{x0}^2 - E_{y0}^2 \\ 2E_{x0}E_{y0}\cos\varphi \\ 2E_{x0}E_{y0}\sin\varphi \end{bmatrix} = S_0 \begin{bmatrix} 1 \\ S_1/S_0 \\ S_2/S_0 \\ S_3/S_0 \end{bmatrix} \tag{2.46}$$

Since in polarimetry we are mostly interested in the state of polarization, the normalized Stokes vector, which is divided by the total intensity, is introduced.
A further fascinating attribute of the Stokes vector is that they obey the superposition principle.

$$\boldsymbol{S}_c = \begin{bmatrix} S_{0c} \\ S_{1c} \\ S_{2c} \\ S_{3c} \end{bmatrix} = \begin{bmatrix} S_{0a} \\ S_{1a} \\ S_{2a} \\ S_{3a} \end{bmatrix} + \begin{bmatrix} S_{0b} \\ S_{1b} \\ S_{2b} \\ S_{3b} \end{bmatrix} = \begin{bmatrix} S_{0a} + S_{0b} \\ S_{1a} + S_{1b} \\ S_{2a} + S_{2b} \\ S_{3a} + S_{3b} \end{bmatrix} = \boldsymbol{S}_a + \boldsymbol{S}_b \tag{2.47}$$

With this principle it is possible to split up the Stokes vector for a partially polarized light into a vector of the full polarization and a Stokes vector of the unpolarized light. Before we do that we have to define the *degree of polarization* (DOP), which defines how much the ray is polarized on total.

$$DOP = \frac{\sqrt{S_1^2 + S_2^2 + S_3^2}}{S_0} \tag{2.48}$$

In nature, there is mostly no circular polarized light and therefore we define another concept of degree of linear polarisation(DOLP), where only linear polarized light is considered.

$$DOLP = \frac{\sqrt{S_1^2 + S_2^2}}{S_0} \tag{2.49}$$

With these definitions we can write a partly polarized light ray as

$$\boldsymbol{S}_{\text{partly}} = \boldsymbol{S}_{\text{pol}} + \boldsymbol{S}_{\text{unpol}} = \begin{bmatrix} DoP \cdot S_0 \\ S_1 \\ S_2 \\ S_3 \end{bmatrix} + (1 - DOP) \cdot \begin{bmatrix} S_0 \\ 0 \\ 0 \\ 0 \end{bmatrix} \tag{2.50}$$

To obtain a deeper understanding of the Stokes vector we put six different ideal polarization filter, which represent the different parts of the Stokes vector in front of an incident beam and measure after every filter the intensity. Figure 2.2 pictures the composition.

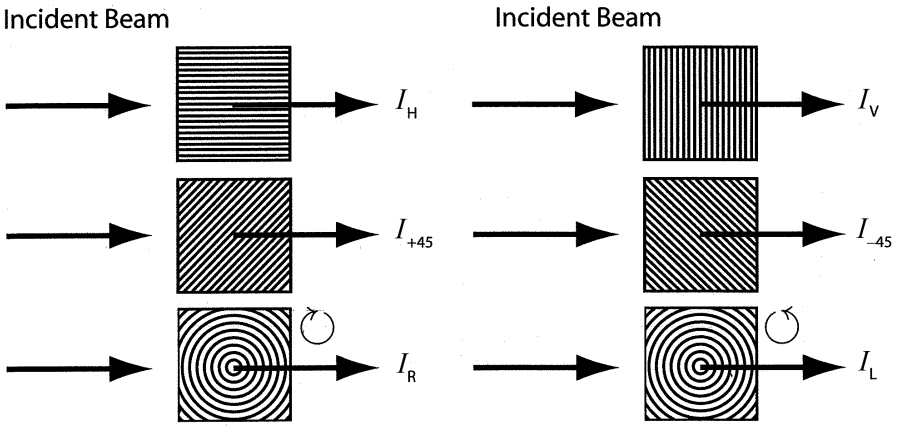

Figure 2.2.: Put different polarization filters in front of an incidence beam to distinguish it's Stokes vector. Source: Schott (2009, p. 39)

The Stokes vector for this setup is given as

$$\boldsymbol{S} = \begin{bmatrix} I_H + I_V \\ I_H - I_V \\ I_{+45} - I_{-45} \\ I_R - I_L \end{bmatrix} \tag{2.51}$$

where $I_H, I_V, I_{+45}, I_{-45}, I_R, I_L$ describe the intensities of the different polarization states.

Table 2.1 gives an overview over the different polarization states and normalized Stokes vector representations.

Table 2.1.: Representation of the different normalized Stokes vector. The S stands for german *senkrecht* (horizontal) and the P stands for parallel.

Polarization State	Symbol	Stokes Vector
Horizontal	$\leftrightarrow$ $\perp$ S	$\begin{bmatrix}1\\1\\0\\0\end{bmatrix}$
Linear +45°	$\nearrow$	$\begin{bmatrix}1\\0\\1\\0\end{bmatrix}$
Right-Hand Circular	$\circlearrowright$	$\begin{bmatrix}1\\0\\0\\1\end{bmatrix}$
Random	$*$	$\begin{bmatrix}1\\0\\0\\0\end{bmatrix}$

Polarization State	Symbol	Stokes Vector
Vertical	$\updownarrow$ $\parallel$ P	$\begin{bmatrix}1\\-1\\0\\0\end{bmatrix}$
Linear -45°	$\nwarrow$	$\begin{bmatrix}1\\0\\-1\\0\end{bmatrix}$
Left-Hand Circular	$\circlearrowleft$	$\begin{bmatrix}1\\0\\0\\-1\end{bmatrix}$

2.2.3. Müller-Matrices

The Stokes vector provides a description of the polarization states and the intensity of a beam. But we do not have a description of the interaction, when this beam is transmitted or reflected by a material. Here the *Müller matrix* comes up, which will represent the interaction of a beam by transforming the Stokes vector. The incoming beam $\boldsymbol{S}_{\text{in}}$ will then be converted to the outgoing beam $\boldsymbol{S}_{\text{out}}$ like

$$\boldsymbol{S}_{\text{out}} = \boldsymbol{M} \cdot \boldsymbol{S}_{\text{in}} \tag{2.52}$$

$$\begin{bmatrix} S_0 \\ S_1 \\ S_2 \\ S_3 \end{bmatrix}_{\text{out}} = \begin{bmatrix} m_{00} & m_{01} & m_{02} & m_{03} \\ m_{10} & m_{11} & m_{12} & m_{13} \\ m_{20} & m_{21} & m_{22} & m_{23} \\ m_{30} & m_{31} & m_{32} & m_{33} \end{bmatrix} \cdot \begin{bmatrix} S_0 \\ S_1 \\ S_2 \\ S_3 \end{bmatrix}_{\text{in}}$$

where $\boldsymbol{M}$ is the *Müller matrix* describing the property of the optical element.
The easiest way to understand Müller matrices is by looking at different examples of polarizers.

ideal horizontal polarizer:
$$M_s = \frac{1}{2}\begin{bmatrix} 1 & 1 & 0 & 0 \\ 1 & 1 & 0 & 0 \\ 0 & 0 & 0 & 0 \\ 0 & 0 & 0 & 0 \end{bmatrix} \tag{2.53}$$

ideal vertical polarizer:
$$M_p = \frac{1}{2}\begin{bmatrix} 1 & -1 & 0 & 0 \\ -1 & 1 & 0 & 0 \\ 0 & 0 & 0 & 0 \\ 0 & 0 & 0 & 0 \end{bmatrix} \tag{2.54}$$

ideal +45° polarizer:
$$M_{+45} = \frac{1}{2}\begin{bmatrix} 1 & 0 & 1 & 0 \\ 0 & 0 & 0 & 0 \\ 1 & 0 & 1 & 0 \\ 0 & 0 & 0 & 0 \end{bmatrix} \tag{2.55}$$

ideal -45° polarizer:
$$M_{-45} = \frac{1}{2}\begin{bmatrix} 1 & 0 & -1 & 0 \\ 0 & 0 & 0 & 0 \\ -1 & 0 & 1 & 0 \\ 0 & 0 & 0 & 0 \end{bmatrix} \tag{2.56}$$

ideal depolarizing filter:
$$M_{\text{depol}} = \begin{bmatrix} 1 & 0 & 0 & 0 \\ 0 & 0 & 0 & 0 \\ 0 & 0 & 0 & 0 \\ 0 & 0 & 0 & 0 \end{bmatrix} \tag{2.57}$$

The factor of $\frac{1}{2}$ in front of the polarizer is important for energy conservation.
Another property of the Müller matrices is that we can combine them by multiplying. If we send a beam $\boldsymbol{S}_{\text{in}}$ first through a horizontal polarizer and afterwards through a +45° polarizer, the result would be

$$\boldsymbol{S}_{\text{out}} = \boldsymbol{M}_{+45} \cdot \boldsymbol{M}_s \cdot \boldsymbol{S}_{\text{in}} \tag{2.58}$$

As we have seen in Sec. 2.2 we can choose our frame of reference, where we measure the components of the Stokes vector. The transformation to another reference frame can as well be represented by a Müller matrix. A change of the reference frame along the beam is equal to a rotation with the angel θ_R. Thus the rotation Müller matrix is given by

$$\begin{aligned} \boldsymbol{S}_\theta &= \boldsymbol{R}(\theta_R) \cdot \boldsymbol{S}_{\text{in}} \\ \begin{bmatrix} S_0 \\ S_1 \\ S_2 \\ S_3 \end{bmatrix}_\theta &= \begin{bmatrix} 1 & 0 & 0 & 0 \\ 0 & \cos 2\theta_R & \sin 2\theta_R & 0 \\ 0 & -\sin 2\theta_R & \cos 2\theta_R & 0 \\ 0 & 0 & 0 & 1 \end{bmatrix} \cdot \begin{bmatrix} S_0 \\ S_1 \\ S_2 \\ S_3 \end{bmatrix}_{\text{in}} \end{aligned} \tag{2.59}$$

As one can easily verify, the rotation has no effect on the circular polarization or on DOP or DOLP, but it has some effect at the polarization angle Φ, which is very intuitive.

2.3. Fresnel equations

In this section we want to look at an incoming light ray that is reflected and transmitted at a surface of a dielectric material. These considerations can also be done for non-dielectric materials and also the Fresnel equations are valid then. For simplicity, we want to look only at simple linear isotropic dielectric materials, where $\mu_r = 1$ and the refraction index is only governed by $n = \sqrt{\varepsilon_r}$ a non complex permittivity.
A ray with the wave vector $\boldsymbol{k}_i$ is coming in the material with the refraction index n_1 at a surface of the material with refraction index n_2. This incoming beam gives rise to a reflected beam $\boldsymbol{k}_r$ and a transmitted beam $\boldsymbol{k}_t$. The situation is depicted in Fig. 2.3. To obtain all relevant effects, we have to take the boundary conditions of Sec. 2.1.2 and Sec. 2.1.5 into account. The first

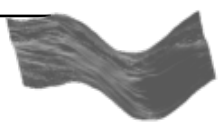

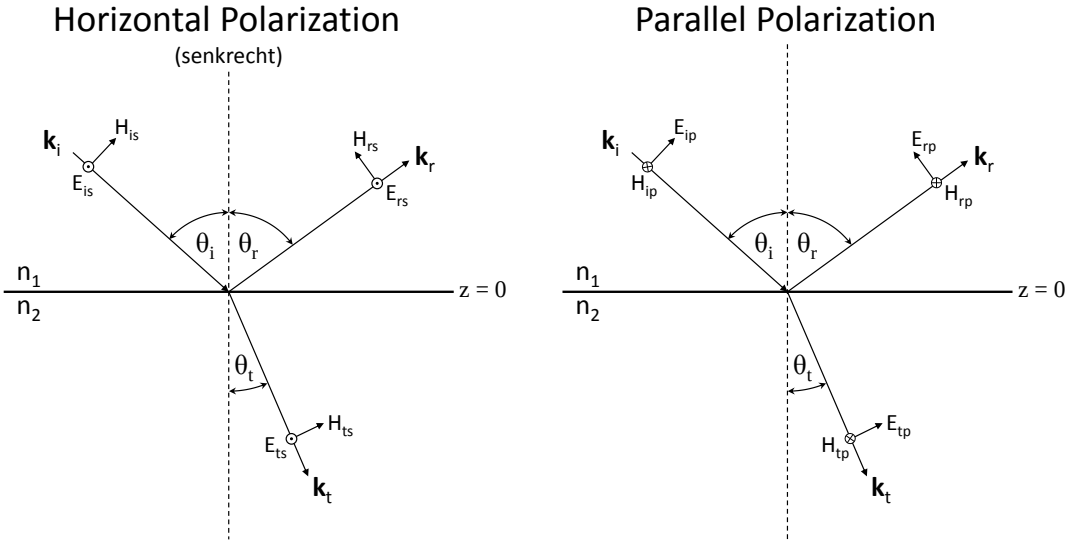

Figure 2.3.: An incidence beam with wave vector $\boldsymbol{k}_i$ gets reflected (wave vector $\boldsymbol{k}_r$) and transmitted (wave vector $\boldsymbol{k}_r$) at a boundary between the two materials with the index of refraction n_1, n_2 respectively. For the horizontal polarization the field vector $\boldsymbol{E}_s$ is looking out from the paper (indicated by the dot in the circle). For the parallel polarization the field vector $\boldsymbol{H}_p$ is looking in the paper (indicated by a cross in the circle).

boundary condition is that at the surface all spatial and also temporal changes of the wave must be the same. This means that at any moment t the phase factor has to be the same. This means the following condition must hold at the surface $z = 0$

$$(\boldsymbol{k}_i \boldsymbol{x})_{z=0} = (\boldsymbol{k}_r \boldsymbol{x})_{z=0} = (\boldsymbol{k}_t \boldsymbol{x})_{z=0} \tag{2.60}$$

This must hold for an arbitrary $\boldsymbol{x}$ at the surface and hence

$$\begin{aligned} &\boldsymbol{k}_{i\parallel} = \boldsymbol{k}_{r\parallel} = \boldsymbol{k}_{t\parallel} \Rightarrow \\ &k_i \cdot \sin\theta_i = k_r \cdot \sin\theta_r = k_t \cdot \sin\theta_t \end{aligned} \tag{2.61}$$

where $k = |\boldsymbol{k}|$ and θ is the angle to the surface normal. Since the magnitude of the incoming and reflected wave vector must be the same $k_i = k_r$, the commonly known reflection principle is derived, where incidence angle is reflection angle.

$$\theta_i = \theta_r \tag{2.62}$$

For the angle of refraction we have to consider the two different indexes of refraction with the dispersion relation $k_i c_i = \omega = k_t c_t$.

$$\frac{k_t}{k_i} = \frac{c_i}{c_t} = \frac{n_2}{n_1} = \frac{\sin\theta_i}{\sin\theta_t} \tag{2.63}$$

This is *Snell's law of refraction.*
From the continuity of the $\boldsymbol{E}$-field $\boldsymbol{n} \times \boldsymbol{E}$ at a dielectric boundary (see Eq. (2.22)) we can obtain the Fresnel's equation for horizontal polarization (horizontal to the plane of incidence), which will be denoted by s for *senkrecht.* Here, the field vector $\boldsymbol{E}$ is always tangential to the surface independent of the incident angle. The continuity condition can therefore be written as

$$E_{\mathrm{is}} + E_{\mathrm{rs}} = E_{\mathrm{ts}}, \tag{2.64}$$

whereas the field vectors $\boldsymbol{H}$ are always perpendicular to the $\boldsymbol{E}$ vector and thus, they must be projected with a $\cos\theta$ at the surface normal. With equation (2.15) and $\mu_r = 1$ the magnitude of $\boldsymbol{H}$ is given by $H = \frac{n}{\mu_0 c_0} E$. Hence the continuity of the tangential component of $\boldsymbol{n} \times \boldsymbol{H}$ leads to

$$n_1 E_{\text{is}} \cos\theta_i - n_1 E_{\text{rs}} \cos\theta_r = n_2 E_{\text{ts}} \cos\theta_t \tag{2.65}$$

After some mathematical manipulation of Eq. 2.64 and Eq. (2.65) with Eq. (2.62) we get the ratio of reflection for the horizontal (German: senkrecht) polarization

$$r_s = \frac{E_{\text{rs}}}{E_{\text{is}}} = \frac{n_1 \cos\theta_i - n_2 \cos\theta_t}{n_1 \cos\theta_i + n_2 \cos\theta_t} \tag{2.66}$$

The same can be done for the ratio of transmission, but since we are only interested in the reflection part, it will not be listed here.
The refraction index in Eq. (2.66) can be eliminated by Snell's law Eq. (2.63). To get the *reflection coefficient* we have to calculate the ratio of reflection for intensities, which are given by Eq. (2.31). Because all factors in front of the $\boldsymbol{E}$-field cancel out for reflection, we just have to square the factors. This yields the *horizontal reflection coefficient*

$$R_s = \frac{I_{\text{rs}}}{I_{\text{is}}} = \frac{E_{\text{rs}}^2}{E_{\text{is}}^2} = \frac{\sin^2(\theta_i - \theta_t)}{\sin^2(\theta_i + \theta_t)} \tag{2.67}$$

Now the same can be done if the field vector $\boldsymbol{E}$ is parallel to the plane of incidence. Here we can use the same boundary conditions as for the horizontal polarization, but we have to exchange the $\boldsymbol{E}$ with the $\boldsymbol{H}$ field. This gives the following conditions

$$H_{\text{ip}} + H_{\text{rp}} = H_{\text{tp}} \quad \Rightarrow \quad n_1 E_{\text{ip}} + n_1 E_{\text{rp}} = n_2 E_{\text{tp}} \tag{2.68}$$

$$E_{\text{ip}} \cos\theta_i - E_{\text{rp}} \cos\theta_i = E_{\text{tp}} \cos\theta_t \tag{2.69}$$

This yields the ratio of reflection for the parallel polarization

$$r_p = \frac{E_{\text{rp}}}{E_{\text{ip}}} = \frac{n_2 \cos\theta_i - n_1 \cos\theta_t}{n_2 \cos\theta_i + n_1 \cos\theta_t} \tag{2.70}$$

This result looks quite similar to the result of the horizontal polarization Eq. (2.66), but with the refraction indices swapped. This has a great impact if we use again Snell's law Eq. (2.63). The *parallel reflection coefficient* for the intensities is then given as

$$R_p = \frac{I_{\text{rp}}}{I_{\text{ip}}} = \frac{E_{\text{rp}}^2}{E_{\text{ip}}^2} = \frac{\tan^2(\theta_i - \theta_t)}{\tan^2(\theta_i + \theta_t)} \tag{2.71}$$

These two *reflection coefficients* (Eq. (2.67) and Eq. (2.71)) together with the transmission coefficients for horizontal and parallel to the plane of incidence polarized light are called the **Fresnel coefficients**.
Another interesting property can be calculated with the Fresnel coefficients, namely the *Brewster angle*. The *Brewster angle* θ_B is defined as the angle, where the parallel polarization of the reflected light vanishes and only horizontal polarization is present. Therefore at the *Brewster angle* the degree of linear polarisationis $DOLP = 1$. For the angle between the transmitted parallel polarized beam θ_t and the reflected horizontal polarized beam θ_r one has $\theta_r + \theta_t = 90°$ (Zinth and Zinth, 2013). From this and the law of reflection $\theta_r = \theta_B$ the following relation for the *Brewster angle* can be derived:

$$\text{Brewster Angle: } \tan\theta_B = \frac{n_2}{n_1} \tag{2.72}$$

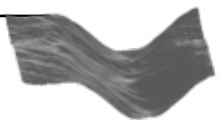

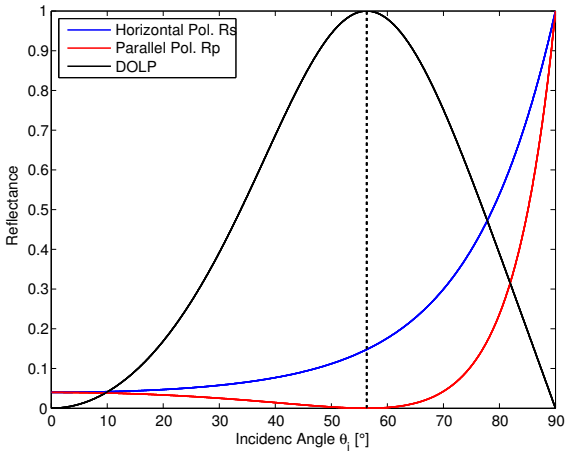

Figure 2.4.: Reflectance for the horizontal (R_s) and parallel (R_p) polarization and degree of linear polarisation(DOLP) plot against the incidence angle θ_i. The *Brewster angle* θ_B is indicated by the dashed line. Material properties: $n_1 = 1, n_2 = 1.5$

Fig. 2.4 shows the reflection coefficients and the degree of linear polarisation(DOLP) for different incidence angles θ_i.

The Fresnel reflection or transmission coefficients can also be included in a *Müller matrix* to describe the interaction of a incoming beam at a surface. The *Müller matrices* for reflection and transmission are given in Brosseau (1998), Schott (2009) and Kattawar and Adams (1989).

$$\text{Reflection Müller matrix} \qquad \boldsymbol{R}(\theta_i,\theta_t) = \begin{bmatrix} \alpha+\eta & \alpha-\eta & 0 & 0 \\ \alpha-\eta & \alpha+\eta & 0 & 0 \\ 0 & 0 & \gamma_{\mathrm{Re}} & 0 \\ 0 & 0 & 0 & \gamma_{\mathrm{Re}} \end{bmatrix} \tag{2.73}$$

$$\text{Transmission Müller matrix} \qquad \boldsymbol{T}(\theta_i,\theta_t) = \begin{bmatrix} \alpha'+\eta' & \alpha'-\eta' & 0 & 0 \\ \alpha'-\eta' & \alpha'+\eta' & 0 & 0 \\ 0 & 0 & \gamma'_{\mathrm{Re}} & 0 \\ 0 & 0 & 0 & \gamma'_{\mathrm{Re}} \end{bmatrix} \tag{2.74}$$

where

$$\alpha = \frac{1}{2}\left(\frac{\tan(\theta_i-\theta_t)}{\tan(\theta_i+\theta_t)}\right)^2 \qquad \eta = \frac{1}{2}\left(\frac{\sin(\theta_i-\theta_t)}{\sin(\theta_i+\theta_t)}\right)^2$$

$$\gamma_{\mathrm{Re}} = \frac{\tan(\theta_i-\theta_t)\sin(\theta_i-\theta_t)}{\tan(\theta_i+\theta_t)\sin(\theta_i+\theta_t)}$$

$$\alpha' = \frac{1}{2}\left(\frac{2\cos\theta_i\sin\theta_t}{\sin(\theta_i+\theta_t)\cos(\theta_i-\theta_t)}\right)^2 \qquad \eta' = \frac{1}{2}\left(\frac{2\cos\theta_i\sin\theta_t}{\sin(\theta_i+\theta_t)}\right)^2$$

$$\gamma'_{\mathrm{Re}} = \frac{4\cos^2\theta_i\sin^2\theta_t}{\sin^2(\theta_i+\theta_t)\cos(\theta_i-\theta_t)}$$

Here, $\alpha, \eta, \gamma_{\mathrm{Re}}$, and $\alpha', \eta', \gamma'_{\mathrm{Re}}$ represent the Fresnel reflection or transmission coefficients respectively for the different incident (θ_i) and transmission angle (θ_t).

3. Method

3.1. Imaging Polarimeter

A polarimeter is a measurement instrument that can measure the polarization state and hence the Stokes vector of the incoming light. An imaging polarimeter is a polarimeter, which measures the polarization state of an object for every image position. This can be achieved with a setup with several cameras. Since a CCD or CMOS camera measures only intensities, which corresponds to the incoming power (see Sec. 2.1.7), different polarization filters in front of the cameras are necessary to measure all components of the Stokes vector (like in Fig. 2.2). At least four linear independent measurements are needed to gain the full information about the four component Stokes vector. If one can assume, that no circular polarized light is present, the last component of the Stokes vector S_3 can be neglected. Therefore only three cameras with three linear polarization filters are required to gather the first three components of the Stokes vector (S_0, S_1, S_2).

First we want to examine an incoming light ray, which has the Stokes Vector $\boldsymbol{S}_{\text{in}} = [S_0, S_1, S_2]^t_{\text{in}}$, going through a polarization filter with the adjusted angle α. After the filter the intensity I_α is measured, which corresponds to the first component of the Stokes vector $\boldsymbol{S}_{\text{out}}$. As we have seen in Sec. 2.2.3 the effect of a linear polarization filter can be described in terms of Müller calculus by a Müller matrix. The Müller matrix for an ideal linear polarization filter with the polarization angle α is given as:

$$\boldsymbol{M}_{\text{lin.pol.}}(\alpha) = \frac{1}{2}\begin{bmatrix} 1 & \cos 2\alpha & \sin 2\alpha & 0 \\ \cos 2\alpha & \cos^2 2\alpha & \cos 2\alpha \sin 2\alpha & 0 \\ \sin 2\alpha & \cos 2\alpha \sin 2\alpha & \sin^2 2\alpha & 0 \\ 0 & 0 & 0 & 0 \end{bmatrix} \tag{3.1}$$

Since the cameras themselves are insensitive to polarization and can only measure the total intensity $S_{0_{\text{out}}}$, we just have to use the first column of the Müller matrix to link the incoming Stokes vector to the intensity.

$$I_\alpha = S_{0_{\text{out}}} = \frac{b}{2} \cdot \begin{bmatrix} 1 & \cos 2\alpha & \sin 2\alpha \end{bmatrix} \cdot \begin{bmatrix} S_0 \\ S_1 \\ S_2 \end{bmatrix}_{\text{in}} \tag{3.2}$$

where b is a factor to correct that the polarization filter is not perfect, α is the angle of the filter. The factor b_f depends on the polarization filter quality and on the efficiency of the intensity measurement system and is therefore normally constant over time. As we can see in Eq. (3.2) the relation between the measured intensity and the incoming Stokes vector is linear if α is not changing. As mentioned before, the minimum requirement to measure the first three components of the incoming Stokes vector is therefore to obtain at least three intensities for three different polarization filter orientations α. As explained in Sec. 4 we have used three cameras each with a different polarization filter angle. To use the full angular resolution of the polarization of 180°, we set the polarization filter at $\alpha = 0°, 60°, 120°$. Since the relation in Eq. (3.2) is linear for each of the three intensities, it is possible to reverse it to obtain the Stokes vector of

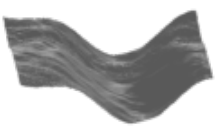

the incoming light:

$$\boldsymbol{S}_{\text{in}} = \begin{bmatrix} S_0 \\ S_1 \\ S_2 \end{bmatrix}_{\text{in}} = \boldsymbol{A} \cdot \mathbf{I} = \begin{bmatrix} a_{11} & a_{12} & a_{13} \\ a_{21} & a_{22} & a_{23} \\ a_{31} & a_{32} & a_{33} \end{bmatrix} \cdot \begin{bmatrix} I_1 \\ I_2 \\ I_3 \end{bmatrix} \tag{3.3}$$

Here the matrix $\boldsymbol{A}$ is the analyzer matrix and describes, how the measured intensities of the polarimeter are related to the Stokes vector. This matrix can be found by calibration of the system, see Sec. 5.6. The analyzer matrix is therefore the heart of the polarimeter, because it enables us to measure the first three components of the Stokes vector.

3.2. Water as dielectric matter

As we have seen in Sec. 2.1.5 dielectric materials have some special characteristics, which are of importance for optics. Water is such a dielectric matter and has an index of refection of $n_{\text{water}} = 1.33$ in our used bandwidth (490 nm to 740 nm) at a temperature of $T = 20°C$ (Daimon and Masumura, 2007). Because water is a dielectric matter the Müller matrix of the Fresnel equation for reflection Eq. (2.73) and transmission Eq. (2.74) between air and water surface are valid. (The refraction index of air is taken as that of vacuum $n_{\text{air}} = 1$.) The Müller calculus describe how an incoming Stokes vector $\boldsymbol{S}_{\text{in}}$ gets changed by the interaction at the air-sea surface. For the measurement of waves on the water surface, sky light is used for illumination. The reflected Stokes vector $\boldsymbol{S}_{\text{R}}$ is than given as:

$$\boldsymbol{S}_{\text{R}} = \boldsymbol{R}_{\text{AS}}(\theta) \cdot \boldsymbol{S}_{\text{sky}} \tag{3.4}$$

with the Stokes vector of the incoming sky light $\boldsymbol{S}_{\text{sky}}$. Here $\boldsymbol{R}_{\text{AS}}(\theta)$ is the Müller matrix of reflection (Eq. (2.73)) at the Air-Sea interface. Eq. 3.4 shows that the polarization state depends on the incidence angle of the reflected light, which is the basis for the polarimetric slope images technique (see Sec. 3.3). To get a functional relationship between the incidence angle θ and the polarization state, the degree of linear polarisation (DOLP) will be calculated. If we assume that the sky is unpolarized, which means that the normalized Stokes vector is $\boldsymbol{S}_{\text{sky}} = \boldsymbol{S}_{\text{up}} = [1,0,0,0]^t$ the DOLP of the reflected Stokes vector $\boldsymbol{S}_{\text{R}}$ can be calculated with Eq. 2.49 as:

$$DOLP(\theta, n) = \frac{\alpha(\theta, n) - \eta(\theta, n)}{\alpha(\theta, n) + \eta(\theta, n)} \tag{3.5}$$

This equation is the key point of the polarimeter wave measurement technique, because it links the polarization to the incidence angle of the incoming light. Figure 3.1 illustrates the dependency of the degree of linear polarisation with the angle of incidence θ. The Brewster angle for water $\theta_{\text{B}} = \tan(n_{\text{water}}) = 53°$ is indicated by a vertical dashed line.

Because DOLP(θ) is not a monotone function (see Fig. 3.1), it is not possible to invert the relation for the whole rang of the incidence angle θ. The inversion from DOLP to θ is possible between 0° and the Brewster angle $\theta_{\text{B}} = 53°$ or between the Brewster angle and 90°. We have chosen to look under an angle of $\theta_{\text{pol}} = 37°$ at the water surface because the DOLP is rising there almost linear, which can be seen in Fig. 3.1b. Figure 3.1b shows the absolute derivative of $|\partial DOLP/\partial\theta|$ over the incidence angle θ. The inflection point, where the gradient is at the maximum and the curve is almost linear, is close to $\theta = 37°$.

In the range between the Brewster angle θ_{B} and 90° the inversion from DOLP to θ is very sensitive. Also the reflection coefficients and therefore the amount of reflected light would be high. Still it is not practicable to measure in this region, because the angle of view of the polarimeter

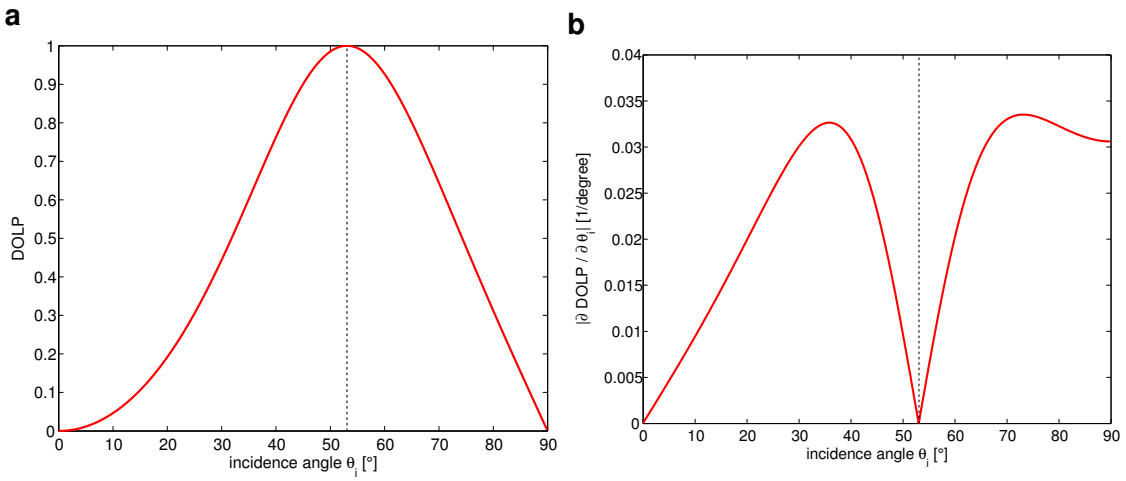

Figure 3.1.: a degree of linear polarisation for the reflection at a air-sea interface calculated from the Fresnel reflection coeffiecents Eq. (3.5) **b** Absolute derivative of $|\partial DOLP/\partial\theta|$ over the incidence angle θ. The Brewster angle of $\theta_B = 53°$ is indicated by a black dashed line.

would be so low, that large waves would hide some parts of the measurement area.

In the previous derivation of the degree of linear polarisation the factor of the upwelling light was neglected. To get the total Stokes vector $\boldsymbol{S}_{\text{tot}}$ that is seen by the Polarimeter, the effect of the upwelling light from beneath the water surface has to be taken into account. The upwelling light with the Stokes vector $\boldsymbol{S}_{\text{up}}$ gets transmitted through the sea surface. Thus the transmission Stokes vector $\boldsymbol{S}_{\text{T}}$ is given as

$$\boldsymbol{S}_{\text{T}} = \boldsymbol{T}_{\text{AS}}(\theta') \cdot \boldsymbol{S}_{\text{up}} \tag{3.6}$$

where $\boldsymbol{T}_{\text{AS}}(\theta')$ is the Müller matrix of transmission (Eq. (2.74)) between an Air-Sea interface. The total Stokes vector is therefore given as

$$\boldsymbol{S}_{\text{tot}} = \boldsymbol{S}_{\text{R}} + \boldsymbol{S}_{\text{T}} = \boldsymbol{R}_{\text{AS}} \cdot \boldsymbol{S}_{\text{sky}} + \boldsymbol{T}_{\text{AS}} \cdot \boldsymbol{S}_{\text{up}} \tag{3.7}$$

If we make the same assumption as before, that the sky and the upwelling light is unpolarized which means that the normalized Stokes vectors are $\boldsymbol{S}_{\text{sky}} = \boldsymbol{S}_{\text{up}} = [1,0,0,0]^t$ the DOLP of the total Stokes vector $\boldsymbol{S}_{\text{tot}}$ can be calculated with Eq. 2.49 as

$$DOLP(\theta,n) = \frac{\alpha(\theta,n) - \eta(\theta,n) + u(\theta,\theta') \cdot (\alpha'(\theta',n) - \eta(\theta',n))}{\alpha(\theta,n) + \eta'(\theta,n) + u(\theta,\theta') \cdot (\alpha'(\theta',n) + \eta'(\theta',n)} \tag{3.8}$$

where α,η,θ are the coefficients of the reflection and α',η',θ' transmission Fresnel formula. $u(\theta,\theta') = S_{0\text{T}}(\theta')/S_{0\text{R}}(\theta)$ is the ratio between the transmitted (or upwelling) and the reflected light intensity (Zappa et al., 2008). The upwelling light changes the degree of linear polarisation which is needed to calculate the surface slope. Hence it is important for an accurate measurement of the reflected DOLP that the upwelling light does not play a role which means that

$$u(\theta,\theta') = \frac{S_{0\text{T}}(\theta')}{S_{0\text{R}}(\theta)} \to 0 \tag{3.9}$$

This leads again to the much simpler form of DOLP(θ) Eq. 3.5 from before. Not only the upwelling light is disturbing Eq. (3.5) but also the incoming polarization from the sky, which will be discussed in the next section.

3.2.1. Polarization of the Sky

The sky consists of many different particles, like gases and aerosols, all with a different size distribution. Therefore the electromagnetic waves of light interact with the particles and get scattered. The scattering process depends on the size of the particle and is mainly divided into two different regimes. The first is the *Rayleigh scattering*, which applies if the particle size is much smaller than the wavelength ($2\pi r << \lambda$) and the other is *Mie scattering*, which is valid if the particle size is equal or greater than the wave length ($2\pi r \geq \lambda$). Here r is the radius of the particle and λ is the wave length. Because the scattering direction for Mie scattering is mainly in forward direction, it can be included in a first order correction to the *Rayleigh sky model*. The Rayleigh sky model describes the polarization of the incoming sun light at a clear sky due to Rayleigh scattering. A description of the sky model can be found in Schott (2009) and an application of the Rayleigh sky model together with a polarimetric slope sensing can be found in Barsic and Chinn (2012). Lee (1998) showed with polarimetric images of the clear sky, that the degree of linear polarisation can even reach $DOLP = 1$ at an angle of 90° to the sun.
With cloud cover the situation changes significantly because in clouds the prevailing scattering type is Mie scattering. Pust and Shaw (2006) showed that the sky gets nearly unpolarized if clouds are on the sky. Horváth et al. (2002) used this phenomenon to detect clouds.

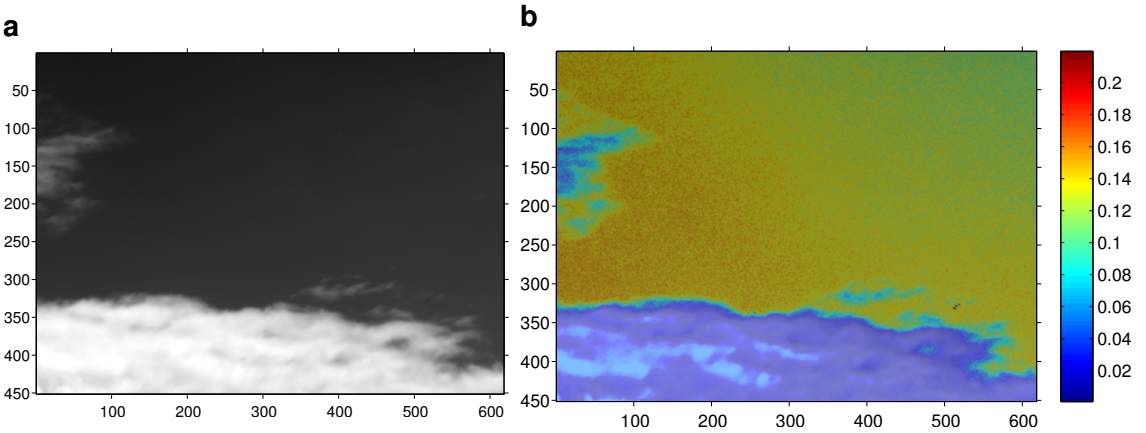

Figure 3.2.: Images of the polarization of the sky taken at 14:50 on the 04.07.2013. Looking direction: South. **a** First component of the Stokes vector S_0, where the clear sky is dark and the clouds are white. **b** Overlay of DOLP onto the S_0 image. The depolarizing effect of the clouds can be seen.

Figure 3.2 shows an image taken with the polarimeter on the 04.07.2013 at 14:50 (local time) of the south part of the sky with some clouds. The sun position was $Elevation = 51.77°$, $Azimuth = 238.79°$ at the geographical position $Latitude = 49.41729°N$, $Longitude = 8.67402°E$[1]. This means, that the sun was above the top right corner of the image. Since the maximal degree of linear polarisation is reached at 90° to the sun, the DOLP looking almost in the direction to the sun gets not more than $DOLP \leq 0.25$. Fig. 3.2a shows the S_0 component of the Stokes vector, to understand the scene. (Sky is mostly dark and the clouds are white.) Fig. 3.2b is an overlay of DOLP onto the S_0 image in color to show the depolarizing effect of clouds.

[1] Sun position calculated with http://www.sunearthtools.com/dp/tools/pos_sun.php

3.3. Polarimetric Slope Imaging

Equation (3.5) is the main equation for the polarimetric slope imaging technique. With the inversion of the equation, from DOLP to θ, it is possible to measure the incidence angle of light onto the water surface. From this and the known angle of view of the polarimeter the slope of the surface can be computed. Since the inversion is not unique it is only possible to invert the equation in the range from $\theta = 0° - 53°$. Together with the polarization angel Φ (Eq. (2.34)) it is possible to recover a two dimensional slope field from the reflected light at the air-sea surface.

If $\eta(\boldsymbol{x}, t)$ is the water surface elevation, the polarimetric slope imaging measures the gradient of the elevation $[s_x, s_y]^t = \nabla\eta(\boldsymbol{x}, t)$. This relation will be later used to recover the surface elevation except for an integration constant (see Sec. 3.4).

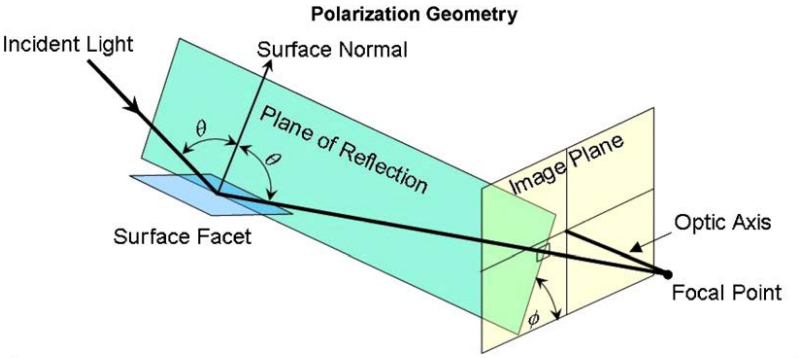

Symbol	Description	Measurement	Range
ϕ	Projected Surface Orientation	Polarization Orientation	[-90°,90°]
θ	Incidence Angle	Degree of Linear Polarization	[0,1]

Figure 3.3.: Geometrical representation of the light path for polarimetric measurements. The reflection surface is defined by the surface normal vector. The angle θ is defined by the vector of the incidence light and the surface normal vector and can be measured with DOLP. The slope of the surface to the horizontal is defined by the angle ϕ. (Attention: $\phi = \Phi + 90°$.) Source: Zappa et al. (2008)

Figure 3.3 shows the geometric relationship between the surface slope and the incidence angle θ (measured with DOLP) and the surface orientation ϕ to the polarization angle Φ, where $\phi = \Phi + 90°$. As derived in Sec. 2.3, the incidence angle and the reflection angel are equal (Eq. (2.62)) and the reflected beam and the surface normal lie in the same plane. The surface orientation ϕ can than be seen as the angle between the X-axis of the imaging plane and the plane of reflection. Therefore the orientation of the surface normal is determined by the angles θ, ϕ relative to the camera reference system.

Because the camera is looking tilted onto the water surface, a projective transformation from the image plane onto the water surface is needed to obtain the water surface slope in Cartesian coordinates, see Sec. 5.2.

Because the system is measuring angles, the angle of view of the camera must be taken into account. This can be done by imposing that the water surface must be flat for a long term average slope. Thus, we can subtract an long term slope average from all images to correct for the angle of view.
To calculate the slope of the surface, we have to do an transformation from θ, ϕ to s_x, s_y. The angular slope of the surface facet can be calculated like that:

$$\begin{aligned} X_{\text{comp}} &= -\cos\phi \cdot \theta = \sin\Phi \cdot \theta \\ Y_{\text{comp}} &= \sin\phi \cdot \theta = \cos\Phi \cdot \theta \end{aligned} \tag{3.10}$$

where $\phi = \Phi + 90°$ was used. To get the actual slope the tangents have to be taken from the $X_{\text{comp}}, Y_{\text{comp}}$.

$$\begin{aligned} s_x &= \tan(X_{\text{comp}}) = \tan(\sin\Phi \cdot \theta) \\ s_y &= \tan(Y_{\text{comp}}) = \tan(\cos\Phi \cdot \theta) \end{aligned} \tag{3.11}$$

From these two slope maps an elevation map can be calculated, which will be done in the next section.

3.4. Height Reconstruction

Since the slope in X- and Y-direction (s_x, s_y) corresponds to the gradient of the surface elevation $h(\boldsymbol{x})$ of the water, it is possible to reconstruct the water height except for an additive constant, which corresponds to the constant of integration. The first attempt to get the height from an gradient field would be integration of the two slope components. The height is then depending on the integration path. Hence for one pixel the height must be calculated from many integration paths, which means, that this method is computational exhausting. Thus a nowadays very commonly used method was proposed by Frankot and Chellappa (1988), which was already successfully applied on water surface slops, see Zhang (1996), Balschbach (2000), Fuß (2004) and Rocholz (2008). This method uses some useful properties of the Fourier domain. A quantity in Fourier domain will be indicated by a ^. The definition and the properties of the spatial Fourier transformation (FT) can be found in Jähne (2005). The starting point is the transformation of the height gradient into Fourier space.

$$\begin{array}{lcll} \text{Spatial domain} & \circ\!\!-\!\!\bullet & \text{Fourier domain} & \\ s_x(\boldsymbol{x}) = \dfrac{\partial h(\boldsymbol{x})}{\partial x} & \circ\!\!-\!\!\bullet & \hat{s}_x(\boldsymbol{k}) = ik_x\hat{h}(\boldsymbol{k}) \quad \Rightarrow & ik_x\hat{s}_x(\boldsymbol{k}) = -k_x^2\hat{h}(\boldsymbol{k}) \\ s_y(\boldsymbol{x}) = \dfrac{\partial h(\boldsymbol{x})}{\partial y} & \circ\!\!-\!\!\bullet & \hat{s}_y(\boldsymbol{k}) = ik_y\hat{h}(\boldsymbol{k}) \quad \Rightarrow & ik_y\hat{s}_y(\boldsymbol{k}) = -k_y^2\hat{h}(\boldsymbol{k}) \end{array} \tag{3.12}$$

Here it was used that a partial derivative ∂_x in Fourier domain is a multiplication with ik_x. Another step was to multiply the equations with ik_x and ik_y respectively. Now the Fourier transformed of the height can be written as:

$$\hat{h}(\boldsymbol{k}) = \frac{-i(k_x\hat{s}_x(\boldsymbol{k}) + k_y\hat{s}_y(\boldsymbol{k})}{(k_x^2 + k_y^2)} \tag{3.13}$$

The denominator $(k_x^2 + k_y^2) = |\boldsymbol{k}^2|$ is the quadratic norm of $\boldsymbol{k}$. The equation can't be evaluated at $(k_x^2 + k_y^2) = |\boldsymbol{k}^2| = 0$, which means that the mean height and the mean slope cannot be recovered with this method. To recover the real height, equation (3.13) must be transformed into real space with the inverse Fourier transformation FT^{-1}. The formula for the height reconstruction is therefore:

$$h(\boldsymbol{x}) = FT^{-1}\left(\frac{-i(k_x\hat{s}_x(\boldsymbol{k}) + k_y\hat{s}_y(\boldsymbol{k})}{(k_x^2 + k_y^2)}\right) \tag{3.14}$$

3.5. Constraints for the Polarimeter technique

As we have seen in the previous sections, there are some constraints on the polarimeter slope imaging technique, so that it is working properly. To summarize and characterize all constraints a list of them will be given here.

No Upwelling Light As we have seen in Eq. (3.8) for DOLP, the upwelling light from underneath the water surface makes the inversion of the relation of DOLP and the angle of incidence θ nearly impossible. In clear and deep water (e.g. in the open ocean) this is not a problem, because the light is absorbed within about 200 m. In turbid water, e.g. coastal areas with a lot of biological activity or turbid rivers, light scattered from suspended particles close beneath the surface can be a problem. In the laboratory, the absorption of water can be increased by adding a dye that absorbs in the bandwidth of the polarimeter.

Unpolarized Incoming Light Eq. (3.5) was derived for an unpolarized incoming light. Hence, if the incoming light is polarized the relation between DOLP and the incidence angle θ gets changed. If the incoming polarization is known, like from a *Rayleigh sky model* or from polarization measurements of the incoming light, it is possible to conclude again from DOLP onto the incidence angle θ. If the polarization of the incoming light cannot be measured, it has to be verified that the incoming light is unpolarized. The incoming sky light can be seen as unpolarized, if the sky is completely overcast. (see Sec. 3.2.1).

Sufficient illumination The reflectivity of water can be calculated from the Fresnel coefficients (Eq. (2.67) and Eq. (2.71)) and reaches from 2.0% at $\theta = 0°$ to 3.8% at $\theta = 53°$. This means that not very much light is reflected at the water surface. Thus, it is necessary to have enough light that can be reflected so that the exposure time can be set low enough to capture the high frequency waves. Especially for inside experiments it has to be paid attention to a proper illumination.

Pixel size small enough Due to the nonlinearity of the dependence of DOLP on surface slope (Eq. (3.5) and Fig. 3.1), the slope should not change significantly over the area that is projected onto one pixel. This means that even in studies where long waves are of interest, the scale of the smallest occuring waves determines the requirement for spatial resolution. In studies of wind generated waves, where capillary waves are abundant, this means that if large areas are to be observed, large image resolution is required.

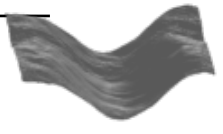

4. Experiments and Setup

There were two major experiments with the polarimeter. One was conducted on board of the research vessel *Meteor* for during one month and the other one was operated at the Hamburgische Schiffsbau-Versuchsanstalt (HSVA) in Hamburg.

4.1. Experiments at the *Meteor*

It was possible to deploy the Stereo Polarimeter on the *Meteor* M91 cruise[1] in front of the Peruvian coastline. The cruise started at the 1st of December 2012 in Callao (Peru) and ended at the 26th of December 2012 in Callao as well. The cruise was part of the *SOPRAN*[2] project, where two PhD students of our group, Daniel Kiefhaber and Leila Nagel, were taking part. On board of the ship the Stereo Polarimeter was operated by Daniel Kiefhaber. Due to the short building time and the early date of the shipment from Heidelberg to Callao at the 12th of October 2012, the setup was barely tested. The setup of the Stereo Polarimeter at the METEOR is described in Sec. 4.3. Table 4.1 lists all measurement stations where the Stereo Polarimeter was running, with the station names and positions taken from the cruise logbook.

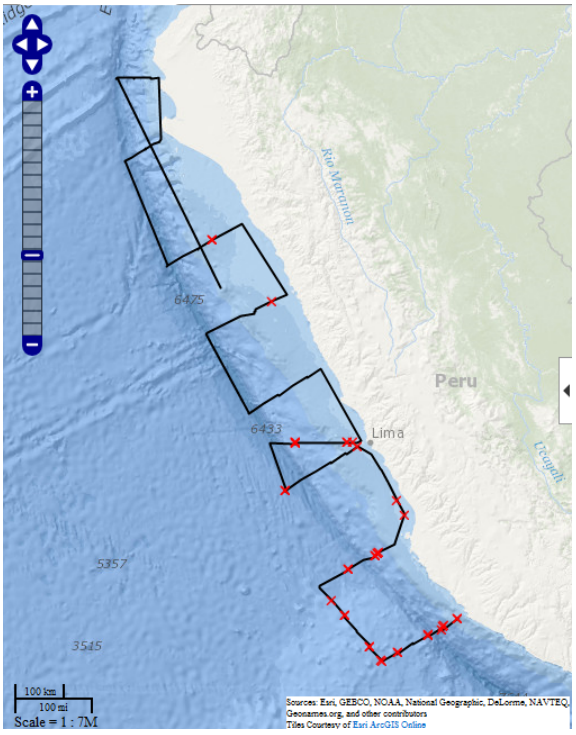

Figure 4.1.: Route of the Meteor (black) in front of Peru with the measurement stations of the Stereo-Polarimeter marked by a red cross. Map generated with Matlab® WebMap.

[1] METEOR M91 Cruise Report: http://www.ifm.zmaw.de/fileadmin/files/leitstelle/meteor/M90_M93/M91-SCR.pdf

[2] SOPRAN - Surface Ocean Processes in the Anthropocene: http://sopran.pangaea.de/

Table 4.1.: Overview of all measurement stations at the *Meteor*where the Stereo Polarimeter was acquiring data. The Station name, Date, Time and Position were taken from the logbook of the *Meteor*.

Num	Station	Date	Time	Position Lat	Position Lon	Recording time
1	1728-1	06.12.2012	21:33:00	8°8.46′ S	80°7.20′ W	70.0 s
2	1728-2	06.12.2012	22:14:00	8°8.40′ S	80°7.19′ W	60.0 s
3	1732-2	07.12.2012	19:31:00	9°19.79′ S	78°58.19′ W	128.0 s
4	1745-2	11.12.2012	19:46:00	12°2.39′ S	77°22.21′ W	90.0 s
5	1746-1	11.12.2012	21:29:00	12°2.39′ S	77°29.41′ W	120.0 s
6	1746-2	11.12.2012	21:54:00	12°2.42′ S	77°29.42′ W	400.0 s
7	1750-1	12.12.2012	14:44:00	12°2.38′ S	78°30.02′ W	120.0 s
8	1750-2	12.12.2012	16:07:00	12°2.44′ S	78°30.01′ W	420.0 s
9	1750-3	12.12.2012	17:37:00	12°3.79′ S	78°29.65′ W	145.0 s
10	1752-5	13.12.2012	14:05:00	12°56.96′ S	78°41.43′ W	200.0 s
11	1752-6	13.12.2012	18:38:00	12°57.03′ S	78°41.43′ W	415.4 s
12	1757-1	15.12.2012	10:02:00	12°6.93′ S	77°17.50′ W	60.0 s
13	1761-3	16.12.2012	18:30:00	13°8.40′ S	76°31.80′ W	2080.0 s
14	1762-1	16.12.2012	22:44:00	13°25.78′ S	76°22.19′ W	120.0 s
15	1764-1	17.12.2012	08:34:00	14°7.23′ S	76°52.23′ W	420.0 s
16	1764-4	17.12.2012	12:11:00	14°8.77′ S	76°53.89′ W	60.0 s
17	1764-5	17.12.2012	16:02:00	14°8.79′ S	76°53.93′ W	1020.0 s
18	1764-9	17.12.2012	22:00:00	14°11.10′ S	76°55.99′ W	60.0 s
19	1764-10	17.12.2012	22:30:00	14°11.11′ S	76°56.01′ W	540.0 s
20	1766-1	18.12.2012	17:27:00	14°26.99′ S	77°28.23′ W	120.0 s
21	1766-2	18.12.2012	18:58:00	14°27.07′ S	77°28.33′ W	480.0 s
22	1769-2	19.12.2012	14:46:00	15°2.93′ S	77°47.39′ W	960.0 s
23	1770-2	19.12.2012	21:07:00	15°19.68′ S	77°32.02′ W	120.0 s
24	1770-3	19.12.2012	22:11:00	15°19.70′ S	77°32.03′ W	1020.0 s
25	1772-3	20.12.2012	10:58:00	15°54.15′ S	77°3.56′ W	60.0 s
26	1772-4	20.12.2012	11:32:00	15°54.21′ S	77°3.62′ W	720.0 s
27	1773-1	20.12.2012	16:19:00	16°10.71′ S	76°48.25′ W	480.0 s
28	1773-3	20.12.2012	20:32:00	16°9.38′ S	76°49.28′ W	360.0 s
29	1774-1	21.12.2012	19:40:00	16°1.15′ S	76°30.14′ W	120.0 s
30	1774-2	21.12.2012	21:15:00	16°1.14′ S	76°30.73′ W	840.0 s
31	1776-1	22.12.2012	09:30:00	15°41.40′ S	75°54.02′ W	60.0 s
32	1776-2	22.12.2012	10:58:00	15°41.46′ S	75°54.01′ W	840.0 s
33	1777-3	22.12.2012	18:34:00	15°31.19′ S	75°36.03′ W	540.0 s
34	1777-5	22.12.2012	20:31:00	15°32.44′ S	75°36.84′ W	1223.0 s
35	1777-9	23.12.2012	12:34:00	15°35.19′ S	75°38.24′ W	1320.0 s
36	1778-1	23.12.2012	20:01:00	15°22.76′ S	75°19.91′ W	60.0 s
37	1778-2	23.12.2012	20:39:00	15°22.83′ S	75°20.04′ W	600.0 s

4.2. Stereo Polarimeter

The idea of the Stereo Polarimeter was to combine stereo height measurements (Benetazzo, 2006; Schumacher, 1939) with slope measurements of the polarimeter (Zappa et al., 2008), to gain information about large and small scale waves. My task was the development of the polarimetric slope imaging technique, but for documentation reasons the stereo measurements will be illustrated here as well.

The Stereo Polarimeter consists of two equal polarimeter boxes, each with three cameras equipped. For cooling reasons, the cameras are installed on an aluminium block parallel to each other with a displacement of 3.5 cm. Some space is left for an optional fourth camera. A power supply for the cameras and a fan for cooling inside the box was installed as well. On each camera of the type *Basler acA2500-14gm* (for the specifications see Tab. 4.2) a *TAMRON* lens[3] with 16 mm focal length is installed. At the lens a polarisation filter from *Schneider-Kreuznach*[4] is mounted. Because the polarisation filter is only working in the bandwidth from 420 nm to 780 nm a yellow filter[5] and an IR-blocking filter[6] (as front window) are placed in front of the polarisation filter. The bandwidth is therefore limited from 490 nm to 740 nm. If necessary, the cameras can be triggered externally with a function generator. A picture of the inside of a polarimeter box and the setup of the optical components is given in Fig. 4.2.

Table 4.2.: Specifications of the camera used. Source: http://www.baslerweb.com/products/ace.html?model=170&language=en

Vendor	Basler
Model	acA2500-14gm
Sensor type	Progressive Scan CMOS, rolling shutter
Sensor diagonal	Diagonal 7.13 mm, Optical Size 1/2.5 inch
Lens Mount	C-Mount
Resolution horizontal/vertical	2592 pixel × 1944 pixel
Pixel Size horizontal/vertical	2.20 μm × 2.20 μm
Pixel Bit Depth	12 bits
Maximum Frame Rate	14 fps (@ 2592 × 1944 pixel)
Synchronization	external trigger, free-run, Ethernet connection
Interface type	Gigabit Ethernet

4.3. Setup *Meteor*

The Stereo Polarimeter was installed at the bow of the research vessel *METEOR*[7]. The rack of the 3 m long stereo basis was mounted on top of the *ACFT*[8] box. The height from the polarimeter boxes to the water surface was 8.9 m. Hence the length of the line of sight was 11.14 m, because the polarimeter was tilted by 37° to the water surface normal. The line of sight is an imaginary

[3] TAMRON M118FM16, http://www.tamron.eu/en/cctv/cctv-single/cctvproduct/m118fm16-wlock-118-16mm-f14-c-mount-3.html

[4] Schneider Fil Pol/CIR 25,5-MRC, http://www.schneiderkreuznach.com/fileadmin/user_upload/bu_industrial_solutions/industriefilter/Polarizer/IF_Polarizer.pdf

[5] Schneider Fil 022/25,5-MRC, http://www.schneiderkreuznach.com/fileadmin/user_upload/bu_industrial_solutions/industriefilter/Color/IF_Color_Filter.pdf

[6] CalflexX, http://www.opticsbalzers.com/data/tmp/1383303693_OBA%20010%20PE.pdf

[7] http://www.ifm.zmaw.de/fileadmin/files/leitstelle/meteor/METEORvirtuell/index.html, http://www.ifm.zmaw.de/fileadmin/files/leitstelle/meteor/M90_M93/M91-SCR.pdf

[8] Active Controlled Flux Technique, see Schimpf et al. (2011)

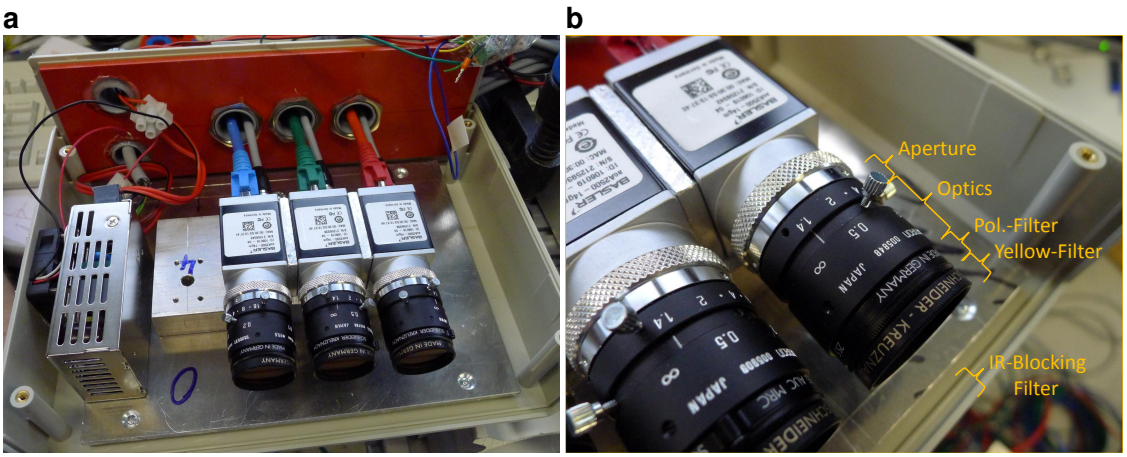

Figure 4.2.: Setup of the Polarimeter: **a** three cameras with different polarisation filters (0°,60°,120°) aligned parallel next to each other. **b** optical components of each camera: optics with aperture, polarisation filter, yellow filter and an IR-blocking filter, which is used as front window of the box.

straight line from the center of the camera to the mean water surface. A sketch of the setup on the *Meteor* and a photo are given in Fig. 4.3. Detailed information about the proportions and configurations is subsumed in Tab. 4.3. A summary of all measurements with the corresponding conditions during the *Meteor* 91 cruise is given in Tab. 4.1.

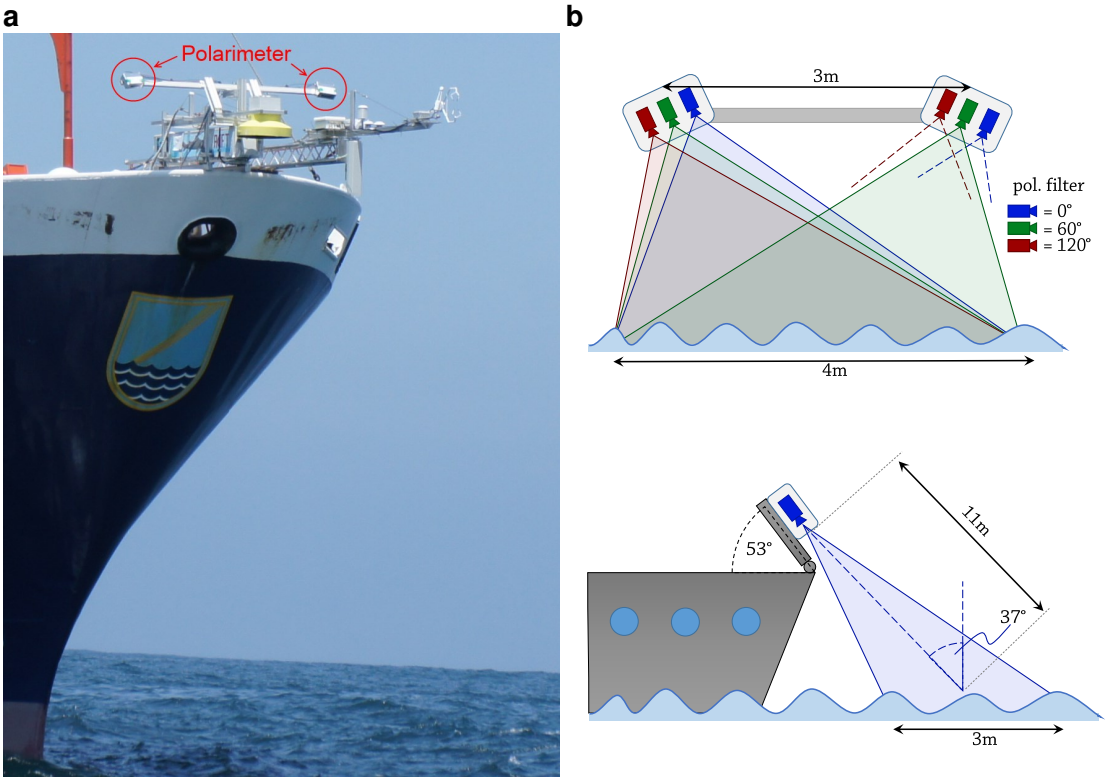

Figure 4.3.: **a** Photo (taken by Daniel Kiefhaber) and **b** Sketch of the Setup of the Stereo Polarimeter at the *Meteor*. The polarimeter was fixed with a *X95*-rack to face the water surface under an angle of 37° to the water surface normal

For calibrating the stereo system a set of chessboard pictures was taken. This was done by turning the Stereo Polarimeter such that it was facing towards the ship.

Table 4.3.: Specifications of the Setup at the *Meteor* with the camera configuration used. (The real image size is calculated as a plane parallel to the image sensor at the distance of the line of sight.)

Focal length	16 mm
Aperture	1.4
Binning	1 x 1
Resulting pixel pitch	2.20 μm x 2.20 μm
Resulting resolution	2592 pixel x 1944 pixel
Maximum frame rate	14 fps
Distance Ship - Water surface	8.9 m
Length of the line of sight	11.14 m
Real image size	3.97 m x 2.97 m
Real resolution	1.53 mm/pixel

4.4. Experiments in Hamburg

The experiments in Hamburg were conducted at the Hamburgische Schiffsbau-Versuchsanstalt[9] on the 12th and 13th of August 2013. At the small towing tank at the HSVA only one polarimeter box was installed, since it was necessary to measure the slope of the waves. In this experiment the waves where not driven by wind, but generated by a wave generator. Different wave spectra were generated. A wave wire was installed at the tank, which is useful for comparison. Table 4.4 shows all measurements and conditions of the experiment.

Table 4.4.: Overview of all measurements and conditions at the Hamburgische Schiffsbau-Versuchsanstalt.

Date	Measurement Name	Generated Waves	Acquisition Frequency	Recording Time
12.08.2013	HSVA1	Test measurements	-	-
12.08.2013	HSVA2	Test measurements	-	-
12.08.2013	HSVA3	Monochromatic	free running	-
12.08.2013	HSVA4	Monochromatic	free running	-
12.08.2013	HSVA5	Monochromatic	10 Hz	1 × 100 s
12.08.2013	HSVA6	Monochromatic	10 Hz	1 × 100 s
12.08.2013	HSVA7	Monochromatic	10 Hz	2 × 100 s
12.08.2013	HSVA8	Monochromatic	10 Hz	2 × 100 s
13.08.2013	HSVA9	Monochromatic	25 Hz	6 × 40 s
13.08.2013	HSVA10	Monochromatic	25 Hz	10 × 40 s
13.08.2013	HSVA11	Monochromatic	25 Hz	1 × 120 s
13.08.2013	HSVA12	Monochromatic	25 Hz	4 × 120 s
13.08.2013	HSVA13	Monochromatic	25 Hz	1 × 120 s
13.08.2013	HSVA14	Monochromatic	25 Hz	2 × 120 s
13.08.2013	HSVA15	Monochromatic	25 Hz	2 × 120 s
13.08.2013	HSVA16	Continuous spectrum	25 Hz	2 × 120 s
13.08.2013	HSVA17	Continuous spectrum	25 Hz	3 × 120 s
13.08.2013	HSVA18	Continuous spectrum	25 Hz	3 × 120 s
13.08.2013	HSVA19	Continuous spectrum	25 Hz	2 × 120 s

[9] HSVA: http://www.hsva.de/

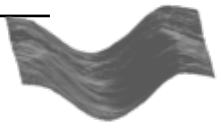

4.5. Setup Hamburg

For measurements at the Hamburgische Schiffsbau-Versuchsanstalt (HSVA) only the polarimeter function of the Stereo Polarimeter was necessary. To fit the needs at the HSVA, the components of one box were changed slightly. To achieve a larger measurement area a *TAMRON* lens[10] with 8 mm focal length was installed on each camera. The yellow filter was replaced by a red filter[11] and as a result the bandwidth of the incoming light was limited to 600 nm–740 nm. To increase the sensitivity of the cameras they were operated in *binning* mode. This means that 4×4 pixel were collected together. Accordingly, the resulting image has a smaller resolution, which was sufficient at the HSVA because the pixel area on the water surface was still smaller than the smallest wave length (see Sec. 3.5). Apart from that, the cameras could be operated with a higher acquisition rate (up to max. 30 fps). Detailed information about the setup is given in Tab. 4.5. The cameras were triggered externally with a function generator, except for the free running mode, where cameras use their internal trigger.

Table 4.5.: Specifications of the Setup at the Hamburgische Schiffsbau-Versuchsanstalt with the camera configuration used. (The real image size is calculated as a plane parallel to the image sensor at the distance of the line of sight.)

Focal length	8 mm
Aperture	1.4
Binning	4 x 4
Resulting pixel pitch	8.80 μm x 8.80 μm
Resulting resolution	648 pixel x 486 pixel
Maximum Frame Rate	30 fps
Length of the line of sight	4.00 m
Real image size	2.85 m x 2.13 m
Real resolution	4.4 mm/pixel

4.5.1. Setup at the HSVA

The polarimeter was operated at the small towing tank of the Hamburgische Schiffsbau-Versuchsanstalt (HSVA). The size of the tank can be seen in Fig. 4.4, where the positions of the wave generator, the wave wire and the polarimeter are marked. The polarimeter was mounted on a ladder such that it faces the water surface normal under an angle of 37°. Fig. 4.5a visualizes the geometry of the setup schematically. The polarimeter box is visible in the upper left corner at the top of the ladder in Fig. 4.5b.

At the Hamburgische Schiffsbau-Versuchsanstalt two problems arose in contrast to the open field measurements (see Sec. 3.5). The first problem was how to achieve a proper **unpolarized illumination**, because there was not enough light for the cameras. The second one are the reflections from the ground of the tank. It is important that **only reflections from the water surface** were seen by the cameras.

Unpolarized Illumination The light that is reflected by the water surface to the polarimeter must be unpolarized before it is reflected. Hence two spotlights, each made out of 140

[10] TAMRON M118FM08, http://www.tamron.eu/en/cctv/cctv-single/cctvproduct/m118fm08-wlock-118-8mm-f14-c-mount-2.html

[11] Hoya R-60 Red M25.5x0.5 Threaded, http://www.edmundoptics.com/optics/optical-filters/color-dichroic-filters/mounted-color-filters/46-542

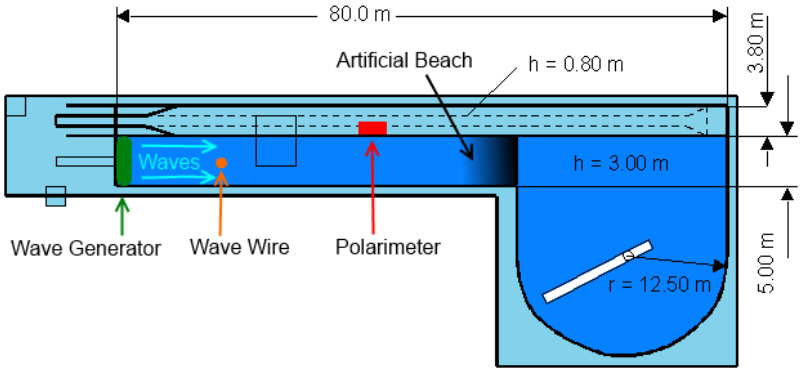

Figure 4.4.: Sketch of the Polarimeter position at the *Small Towing Tank* at the HSVA. Source: http://www.hsva.de/

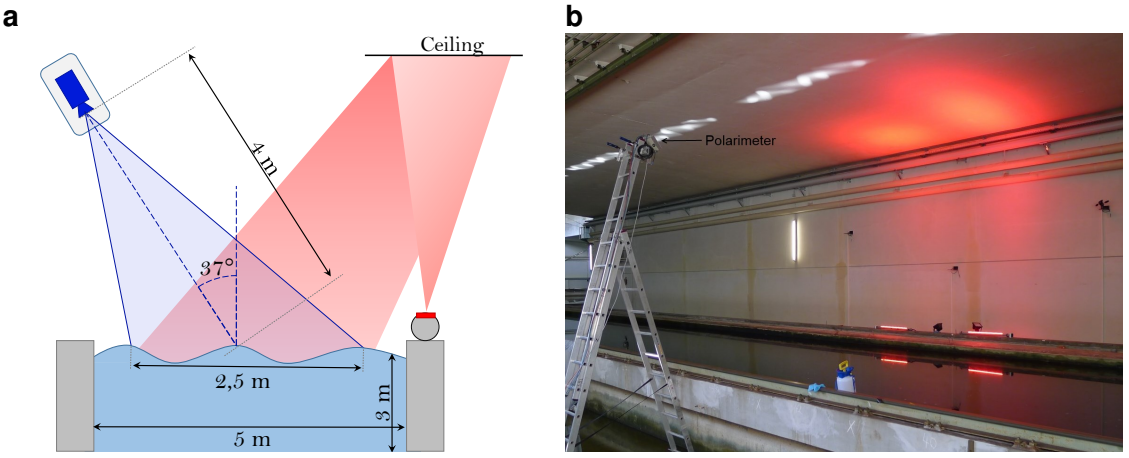

Figure 4.5.: **a** Sketch of the polarimeter setup at the small towing tank at the HSVA. On the right hand side the light source is illuminating the ceiling. The polarimeter sees the reflection of the ceiling at the water surface. **b** Photo of the polarimeter setup.

high-performance LEDs[12] ($\lambda_{\text{peak}} = 630\,\text{nm}$), were built for illumination. The degree of linear polarisation of the light reflected by the ceiling (see Fig. 4.5) was checked on-site and it was just a few percent.

Only reflections from the water surface All light that is gathered by the cameras must come from the water surface. Otherwise the assumption that no upwelling light is present (see Sec. 3.5) is not justified any more. When light hits the water surface nearly perpendicularly only a fraction of about 2% is reflected. Thus, almost all light is transmitted into the water. Therefore it must be guaranteed that no light is reflected by the bottom of the tank. At the beginning of the experiment the ground was visible, because the self absorption of the water was not high enough. To enhance the absorption of the water the dye *Patent Blue V*[13] was added. As it can be seen in Fig. 4.6 the absorption bandwidth overlaps with the bandwidth of the LEDs from the spotlight. Hence, only a small amount of dye was necessary to prevent all reflections of the ground. In total, an amount of 40 g was added to the towing tank with a capacity of about 2.7×10^6 l of water.

[12] Cree XP-E red, http://www.cree.com/~/media/Files/Cree/LED%20Components%20and%20Modules/XLamp/Data%20and%20Binning/XLampXPE.pdf

[13] Patent blue V sodium salt (E131)

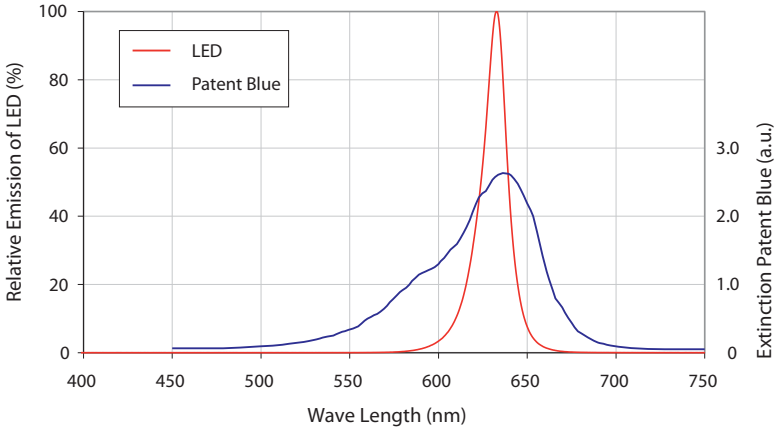

Figure 4.6.: Emission spectrum of the red LEDs used and absorption spectrum of *Patent Blue V*. The absorption is almost the highest at the wavelengths where the LEDs emit. Source of the Data: LEDs http://www.cree.com/~/media/Files/Cree/LED%20Components%20and%20Modules/XLamp/Data%20and%20Binning/XLampXPE.pdf, Patent Blue V http://www.zum.de/Faecher/Ch/BW/smarties.shtml

5. Calibration

The calibration is one of the most important parts of my work, because it is crucial for the success of the measurements.

5.1. Coordinate Systems

In photogrammetry the correct definition of coordinate systems is important, because it mainly deals with transformations from one coordinate system (e.g. the camera) to another one (e.g. the real world). All coordinate systems used are listed and explained below.

5.1.1. Pixel Coordinate Frame

The pixel coordinate frame is the coordinate system of a digital image and consists of columns and rows (u, v). The origin $(u = 0, v = 0)$ is in the upper-left corner and is defined with the positive y-axis pointing downwards. A digital image can also be interpreted as a matrix, which becomes multidimensional if there is more information, like color or image sequences.

5.1.2. Image Coordinate Frame

The image coordinate frame (often also: camera coordinate/reference frame) determines the camera reference system. First of all we will define it as a flat Cartesian coordinate system (x', y') (see Fig. 5.1). This coordinate frame is fixed to reference points of the camera like the pixel coordinate frame. The difference to the pixel coordinate frame is that it's origin is in the center of the image and the coordinates are continuous. The origin of this coordinate system is also called principal point (see. Sec. 5.3).

This coordinate system can be extended by a z'-axis to become a right-handed three dimensional coordinate system. The origin of this three dimensional coordinate system is the projection center of the camera O'.

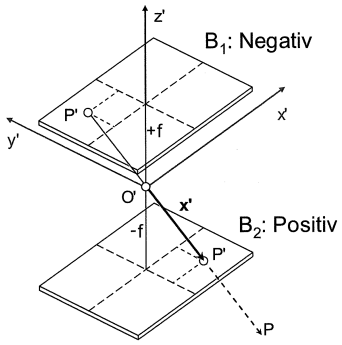

Figure 5.1.: Sketch of the image coordinate system. The physical imaging process is taking place at the negative B_1. In photogrammetry it is easier to think of the positive definition B_2, since the vector $\boldsymbol{x}'$ is pointing to the point P in world coordinates. Source: Luhmann (2010, p. 25, Fig. 2.2)

With the extension of the z'-axis it is possible to define a vector $\boldsymbol{x}'$:

$$\boldsymbol{x}' = \begin{bmatrix} x' \\ y' \\ z' \end{bmatrix} = \begin{bmatrix} x' \\ y' \\ -f \end{bmatrix} \tag{5.1}$$

where f is the focal length of the camera. z' component is negative because the image coordinate system is right-handed. This vector $\boldsymbol{x}'$ points to the point P, which is defined in world coordinates (see Sec. 5.1.3). x', y' and z' are continuous coordinates, but are related to the pixel coordinate frame via the pixel size, pixel position and focal length (Sec. 5.1.1).

Normalized Coordinates

Normalized coordinates can be seen as a projection of a pinhole camera. A pinhole camera is a simple camera model without aberrations, like the one we have used in the previous section. If P' is a point defined in the camera reference frame, with the vector $P' = [x', y', z']^t$, the normalized coordinates are defined as:

$$\boldsymbol{x}_n = \begin{bmatrix} x_n \\ y_n \\ 1 \end{bmatrix} = \begin{bmatrix} x'/z' \\ y'/z' \\ 1 \end{bmatrix} \tag{5.2}$$

The normalized coordinates are therefore independent of any properties of the camera.

5.1.3. World Coordinate Frame

The world coordinate frame (often also: object coordinate frame) is a Cartesian coordinate system (X, Y, Z), which is defined by reference points at an object in the real world. The aim of photogrammetry is to connect the world coordinate frame to the camera frame and therefore to the pixel coordinates. The definition of the origin, the coordinate orientation and the scaling is often called *datum*. The transformation from world coordinates to image coordinates is visualized in Fig. 5.3.

5.2. Coordinate Transformations

Transformations are needed to change between two reference systems. Thus finding the right transformation is one of the key points of photogrammetry. *Similarity*, *affine*, *polynomial* and *bilinear* transformations are well discussed and presented in many books about this topic, e.g. Luhmann (2010), Forsyth and Ponce (2002), Szeliski (2011), Hartley and Zisserman (2003). The most important transformation, the 2D projective transformation, is described in the next section.

5.2.1. 2D Projective Transformation

A plane (2D) projective transformation or also plane homography transforms one plane (2D) coordinate system to another one, where each ray of the projection crosses the projection center.

The transformation rule is given as:

$$\begin{aligned} X &= \frac{a_0 + a_1 x + a_2 y}{1 + c_1 x + c_2 y} \\ Y &= \frac{b_0 + b_1 x + b_2 y}{1 + c_1 x + c_2 y} \end{aligned} \tag{5.3}$$

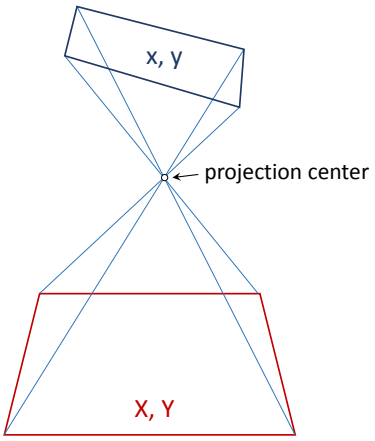

Figure 5.2.: Plane projective transformation from one plane (x, y) to another one (X, Y) or vice versa

or in matrix notation with normalized vectors:

$$\boldsymbol{X} = \begin{bmatrix} X \\ Y \\ 1 \end{bmatrix} = \begin{bmatrix} a_1 & a_2 & a_0 \\ b_1 & b_2 & b_0 \\ c_1 & c_2 & 1 \end{bmatrix} \cdot \begin{bmatrix} x \\ y \\ 1 \end{bmatrix} = \boldsymbol{H} \cdot \boldsymbol{x} \tag{5.4}$$

Here the coordinates (X, Y) and (x, y) can be of any plane euclidean coordinate system. For example the projective transformation can be used to transform from one camera system to another one or from one camera system to the water surface.

As it can be seen in eq. (5.3) and eq. (5.4) the projective transformation has 8 *degrees of freedom* (DOF). The equation can be solved by linearizing Eq. (5.3) by multiplying with the denominator.

$$\begin{aligned} a_0 + a_1 x + a_2 y - X - c_1 xX - c_2 yX &= 0 \\ b_0 + b_1 x + b_2 y - Y - c_1 xY - c_2 yY &= 0 \end{aligned} \tag{5.5}$$

The parameters of the homography can be solved either with a least-squares fit or with SVD (*single value decomposition*). For a detailed description of the SVD see Trucco and Verri (1998). A special property of the plane projective transformation is that double ratios are conserved, which is also known as the intercept theorem.

5.2.2. 3D Transformations

A 3D transformation from one 3D coordinate system to another one is in general given by a displacement vector $\boldsymbol{X}_0$, a scaling factor m and a rotation matrix $\boldsymbol{R}(\omega, \varphi, \kappa)$. (More information about rotation matrices can be found in Sec. A.1)

$$\begin{aligned} \boldsymbol{X} &= \boldsymbol{X}_0 + m \cdot \boldsymbol{R} \cdot \boldsymbol{x}' \\ \begin{bmatrix} X \\ Y \\ Z \end{bmatrix} &= \begin{bmatrix} X_0 \\ Y_0 \\ Z_0 \end{bmatrix} + m \cdot \begin{bmatrix} r_{11} & r_{12} & r_{13} \\ r_{21} & r_{22} & r_{23} \\ r_{31} & r_{32} & r_{33} \end{bmatrix} \cdot \begin{bmatrix} x' \\ y' \\ z' \end{bmatrix} \end{aligned} \tag{5.6}$$

Figure 5.3 shows a sketch of a transformation from world coordinates to image coordinates.

Equation (5.6) can be seen as starting point to derive the main equation of photogrammetry, the so called *collinearity equation*. As we have seen in Sec. 5.1.2 the camera coordinate system

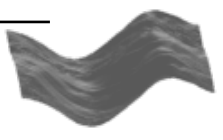

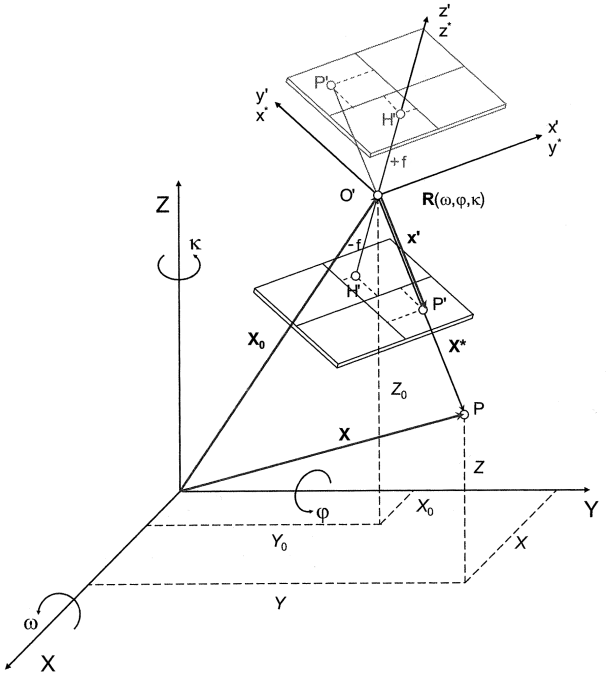

Figure 5.3.: Sketch of the coordinate transformation from world coordinates to the image coordinates. Source: Luhmann (2010, p. 237, Fig. 4.4)

is primarily two dimensional (x', y'). The imaging process therefore describes the transformation from a world coordinate point (X, Y, Z) to the image coordinates (x', y'). This can be done by rewriting Eq. (5.6):

$$
\begin{aligned}
x' &= \frac{a'_0 + a'_1 X + a'_2 Y + a'_3 Z}{1 + c'_1 X + c'_2 Y + c'_3 Z} \\
y' &= \frac{b'_0 + b'_1 X + b'_2 Y + b'_3 Z}{1 + c'_1 X + c'_2 Y + c'_3 Z}
\end{aligned}
\tag{5.7}
$$

This equation is the three dimensional projection equation or collinearity equation. The parameters a', b', c' can be calculated from the translation vector $\boldsymbol{X}_0$ and the rotation matrix $\boldsymbol{R}$. Since we transform from a 3D coordinate system to a 2D coordinate system, the distance information in z-direction is lost completely.

5.3. Camera Matrix

With the camera matrix it is possible to transform normalized coordinates (see Sec.5.1.2) to the pixel coordinate frame (see Sec.5.1.1). The camera matrix contains the intrinsic parameters of the camera without the distortion. There are five independent intrinsic camera parameters, which are the focal length (f_x, f_y), the principal point (cc_x, cc_y) and the shear parameter α_c. The focal length is split into two parameters, because the ratio $f_y / f_x = (1 + m)$ gives the scaling difference, if the pixels are not squared. (For squared pixels $m = 0$). The shear parameter α_c is important if the pixels are not rectangular. The principal point (cc_x, cc_y) gives the penetration

point of the optical axis at the sensor in pixel coordinates. The camera matrix $\boldsymbol{K}$ is then:

$$\boldsymbol{K} = \begin{bmatrix} 1 & \alpha_c & cc_x \\ 0 & (1+m) & cc_y \\ 0 & 0 & 1 \end{bmatrix} \cdot \begin{bmatrix} f_x & 0 & 0 \\ 0 & f_x & 0 \\ 0 & 0 & 1 \end{bmatrix} = \begin{bmatrix} f_x & \alpha_c \cdot f_x & cc_x \\ 0 & f_y & cc_y \\ 0 & 0 & 1 \end{bmatrix} \tag{5.8}$$

The combination of the camera matrix and the 3D-Transformation equation 5.6 then gives the total projection matrix $\boldsymbol{P}$, which describes the transformation from the world reference frame to the pixel coordinate frame. The projection matrix $\boldsymbol{P}$ has 11 DOF in total, 5 DOF from the intrinsic parameters ($\boldsymbol{K}$-Matrix) and 6 DOF from the extrinsic parameters (3 rotation angles and 3 components of the translation vector $\boldsymbol{X}_0$).

$$\boldsymbol{P} = \boldsymbol{K} \cdot \boldsymbol{R} \cdot [\boldsymbol{I}| - \boldsymbol{X}_0] = \begin{bmatrix} f_x & \alpha_c \cdot f_x & cc_x \\ 0 & f_y & cc_y \\ 0 & 0 & 1 \end{bmatrix} \cdot \begin{bmatrix} r_{11} & r_{12} & r_{13} \\ r_{21} & r_{22} & r_{23} \\ r_{31} & r_{32} & r_{33} \end{bmatrix} \cdot \begin{bmatrix} 1 & 0 & 0 & -X_0 \\ 0 & 1 & 0 & -Y_0 \\ 0 & 0 & 1 & -Z_0 \end{bmatrix} \tag{5.9}$$

Here a new notation is introduced (in geometry often called *homogeneous coordinates*) to simplify the subtraction of the translation vector $\boldsymbol{X}_0$. Thus the projection matrix $\boldsymbol{P}$ is a 3×4 dimensional matrix and therefore the 3 dimensional vector $\boldsymbol{X}$ must be changed into to a 4 dimensional vector by adding 1 as fourth component. The transformation from object coordinates $\boldsymbol{X}$ to normalized camera coordinates $\boldsymbol{x}'$ is then given as:

$$\boldsymbol{x}' = \boldsymbol{P} \cdot \begin{bmatrix} \boldsymbol{X} \\ 1 \end{bmatrix} = \boldsymbol{K} \cdot \boldsymbol{R} \cdot (\boldsymbol{X} - \boldsymbol{X}_0) \tag{5.10}$$

5.4. Imaging Optics and Optical Aberration

There are many different optical aberrations, but most of them are corrected by a good lens. Detailed information about the different aberrations can be found in Jähne et al. (1999), Jähne (2005), Luhmann (2010). In our setup **spherical aberrations**, **astigmatism** and **coma aberrations** were corrected by the lens very well and therefore they where not taken into account for the calibration procedure. The **chromatic aberrations** also do not play a major role because the visible spectrum was limited to a small bandwidth with optical filters. Hence the most important aberration for calibration is the **distortion** of the lens. Additionally, there exist some radiometric properties as well that cannot be corrected by a good lens, like the field darkening or the dark noise. Therefore a correction these parameters is important for high quality images.

5.4.1. Field darkening

The intensity of an incoming bundle of light rays is reduced by a factor of $\cos^4\theta$, θ is the angle between the incoming light ray and the optical axis of the lens.

$$I_{\text{Sensor}} = I_{\text{Incoming}} \cdot \cos^4\theta \tag{5.11}$$

There is also an effect of the aperture, which is discussed in Jähne et al. (1999) and Jähne (2005). The factor of $\cos^4\theta$ is composed of a factor of $\cos^2\theta$ from the *inverse square law* (the reduction of the incoming cross-section for the incoming ray bundle), a factor of $\cos\theta$ from passing the lenses in a sloped way and a factor of $\cos\theta$ by light rays hitting the sensor not perpendicular.
This effect can easily be corrected by taking a mean picture of the *integrating sphere*, which produces an evenly distributed light field and normalizing it to one for the highest intensity in a picture. A calibration picture and the setup in front of the integrating sphere can be seen in Fig. 5.4.

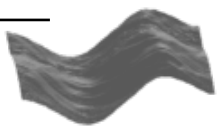

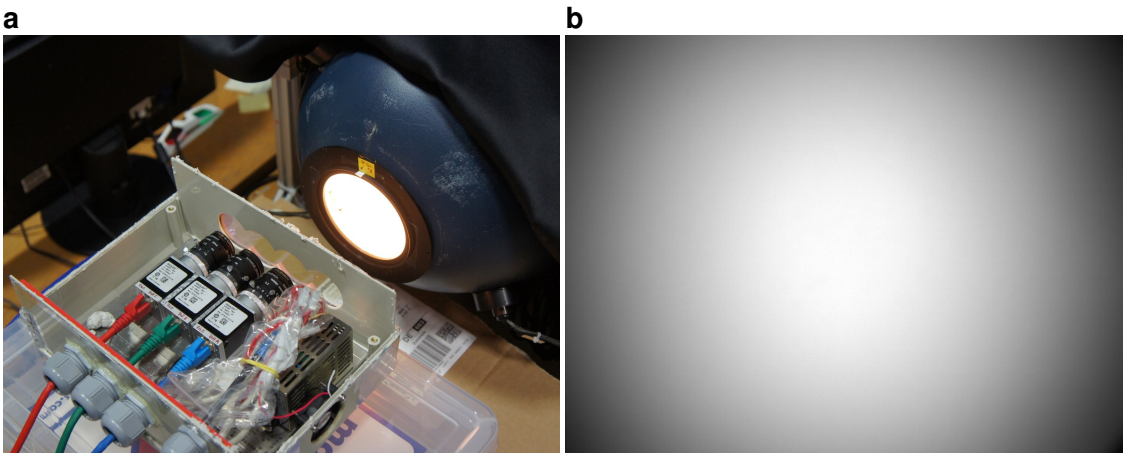

Figure 5.4.: **a** Setup for the radiometric calibration of the cameras. The cameras are placed parallel in front of the *integrating sphere*. **b** The result of a mean image with an $8\,\mathrm{mm}$ optics.

5.4.2. Dark Noise

Due to thermal effects the sensor becomes exposed even when the camera is put into complete darkness. This noise is called dark noise or amplifier noise because it is provoked by the thermal stimulation of the "reading"-electronics of the sensor. Each pixel of a CMOS-sensor has its own amplifier. All these amplifiers have a slightly different offset. The CMOS sensor therefore has a fixed pattern noise, which comes from the offset differences. The fixed pattern noise occurs especially in the dark parts of an image, since the amplifiers also becomes thermal stimulated. This fixed pattern noise can easily be corrected by subtracting a dark image after the acquisition of an image. The dark image is generated by taking the mean of a long time series of images which are acquired when the camera is completely covered, so that no light can enter the lens. A typical dark image can be seen in Fig. 5.5. A normalized image with correction of the field

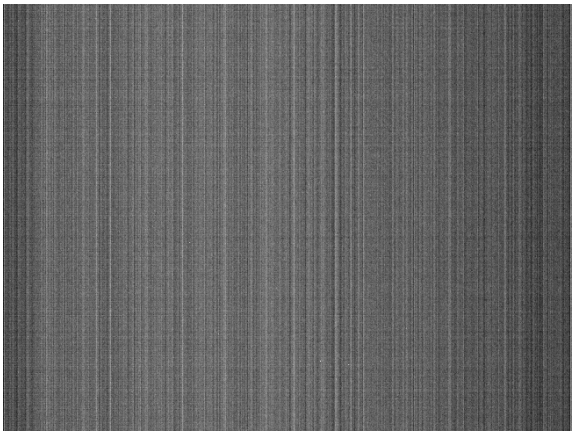

Figure 5.5.: Example of the dark image of a *Basler acA2500-14gm*

darkening and of the dark noise is computed like this:

$$I_{\mathrm{norm}} = \frac{I_{\mathrm{in}} - I_D}{I_M - I_D} \tag{5.12}$$

here I_{in} is the image input, I_D is the dark image, I_M is an image of the field darkening and I_{norm} is the normalized image.

5.4.3. Depth-of-field

To get a sharp image of an object it is not only necessary to adjust the focus at the correct length, but as well to adjust the aperture so that the whole measurement range is in the depth-of-field. In our case the aperture was fixed to $n_f = 1.4$ and the focus was set at 11 m at the Meteor and at 5 m in Hamburg. The calculation of the measurement range (depth-of-field), where the image is not blurred, is done in many textbooks like in Haferkorn (1994). The depth-of-field $\Delta d = d_f - d_n$ is defined as the difference between the near point d_n and far point d_f, where the image is still focused. The relationship between these points is depicted in Fig. 5.6.

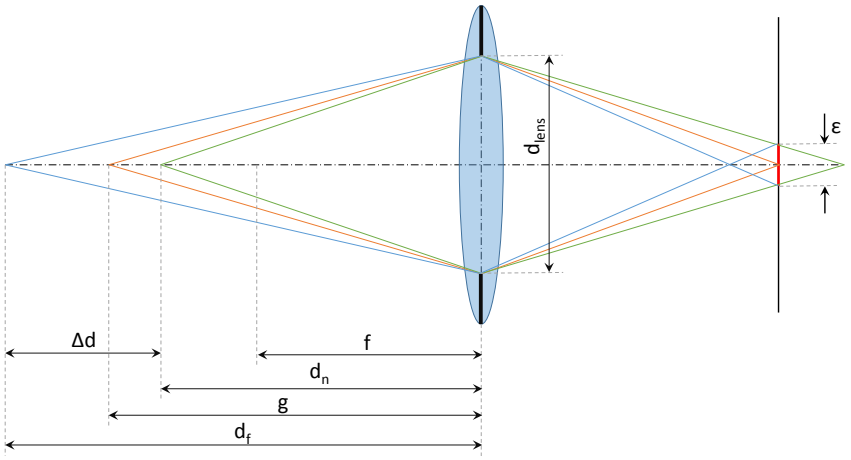

Figure 5.6.: Sketch of a lens with an aperture (opening diameter d_{lens}), where all important distances for the depth-of-focus Δd calculation are depicted.

Near and far point are computed like this:

$$d_n = \frac{1}{\frac{1}{g} + \frac{1}{d_h}} \qquad d_f = \frac{1}{\frac{1}{g} - \frac{1}{d_h}} \tag{5.13}$$

where g is the distance to the focused object and d_h is the hyperfocal distance. These equations are valid only with the assumption of $g >> f$, which is given for all of our setups. The hyperfocal distance is defined as:

$$d_h = \frac{f^2}{n_f \cdot \varepsilon} + f \tag{5.14}$$

where f is the focal length, $n_f = \frac{f}{d_{\text{lens}}}$ is the f-number, with the opening diameter of the aperture d_{lens} and ε is the diameter of the blur disk (in general the pixel size). In our case the hyperfocal length for $f = 16\,\text{mm}$, $n_f = 1.4$ and $\varepsilon = 2.2\,\mu\text{m}$ (size of one pixel) is $d_h = 83.13\,\text{m}$ and for $f = 8\,\text{mm}$, $n_f = 1.4$ and $\varepsilon = 8.8\,\mu\text{m}$ (size of one pixel with binning 4x4) is $d_h = 5.203\,\text{m}$. Table 5.1 gives an overview of the different distances and depth-of-field for the different experimental setups.

Table 5.1.: Calculated depth-of-field Δd and important distances for the two different setups

	Setup Meteor	Setup Hamburg
Focus f	16.0 mm	8.0 mm
F-Stop n_f	1.4	1.4
Pixel size ε	2.2 µm	8.8 µm
Object distance g	11.14 m	5.00 m
Hyperfocal length d_h	83.13 m	5.20 m
Near Point d_n	9.82 m	2.55 m
Far Point d_f	12.86 m	128.27 m
Depth of Field Δd	3.04 m	125.72 m

5.4.4. Distortion

For most lenses, distortion is the most significant optical aberration. For the functionality of the polarimeter three images have to be mapped. In order to avoid errors the distortion correction is crucial for a correct mapping. Hence a major part of this thesis was to quantify the distortion of the cameras.

The primary part of distortion is the radial symmetric distortion, which can be classified into two different regimes, depending on the sign of the distortion parameter: *barrel distortion* (negative sign) and *pincushion distortion* (positive sign).

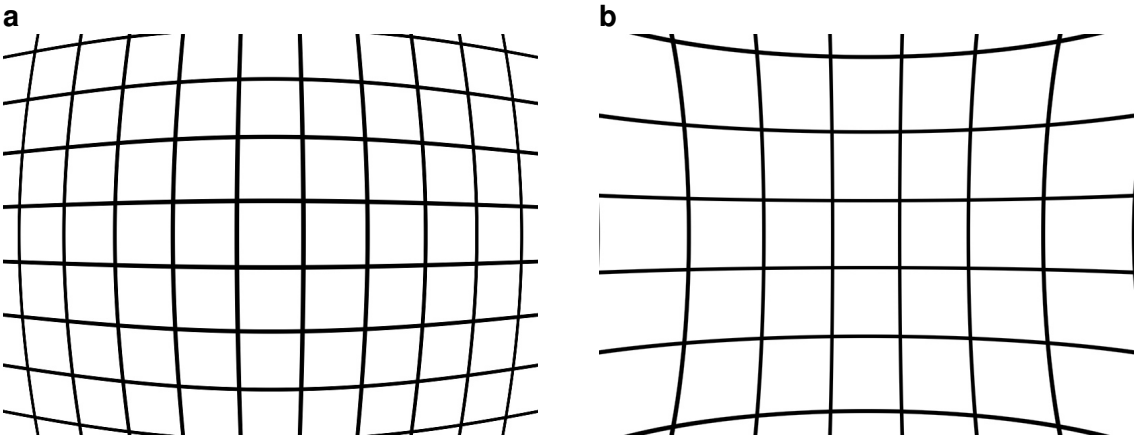

Figure 5.7.: Illustration of **a** *barrel distortion* and **b** *pincushion distortion*

There is a lot of literature about this topic like Zhang (2000), Heikkilä and Silven (1997), Tsai (1987) each one with its own calibration parameters and procedure. For the optimization of the parameters we used the *Camera Calibration Toolbox for Matlab* (Bouguet, 2008) and for consistence we use the same notation.

Radial-symmetric distortion

The radial symmetric distortion has the most significant effect on the images. The origin of the radial distortion normally is the principal point. Therefore it is important to use the image coordinates (see Sec. 5.1.2) or the normalized coordinates (see Sec. 5.1.2) for further calculations. Normalized coordinates can as well be achieved with pixel coordinates by multiplying them with the inverse of the camera matrix. We will use the definition of the normalized coordinates

$\boldsymbol{x}_n$ Eq. (5.2), which were defined as:

$$\boldsymbol{x}_n = \begin{bmatrix} x_n \\ y_n \end{bmatrix} = \begin{bmatrix} x'/z' \\ y'/z' \end{bmatrix} \tag{5.15}$$

With the normalized coordinates we can define a radius from the origin as:

$$r^2 = x_n^2 + y_n^2 \tag{5.16}$$

For our purpose it was sufficient to take just two radial distortion coefficients (k_1, k_2). With these definitions we get for the radial distortion vector $\boldsymbol{x}_{\text{rad}}$:

$$\boldsymbol{x}_{\text{rad}} = (1 + k_1 r^2 + k_2 r^4)\boldsymbol{x}_n \tag{5.17}$$

The effect of the radial distortion and the distortion curve can be seen in Fig. 5.8. Fig. 5.8a visualizes the distortion coefficient of Eq. (5.17) in front of $\boldsymbol{x}_n$ over the normalized radius r. The barrel distortion of this lens is clearly visible, since the first coefficient k_1 is negative and the radial distortion factor reaches below one. Fig. 5.8b shows the radial distortion map. The cross indicates the middle of the image and circle indicates the principal point. The arrows point from the ideal position to the distorted position of the image points. The contours show the shift in pixels.

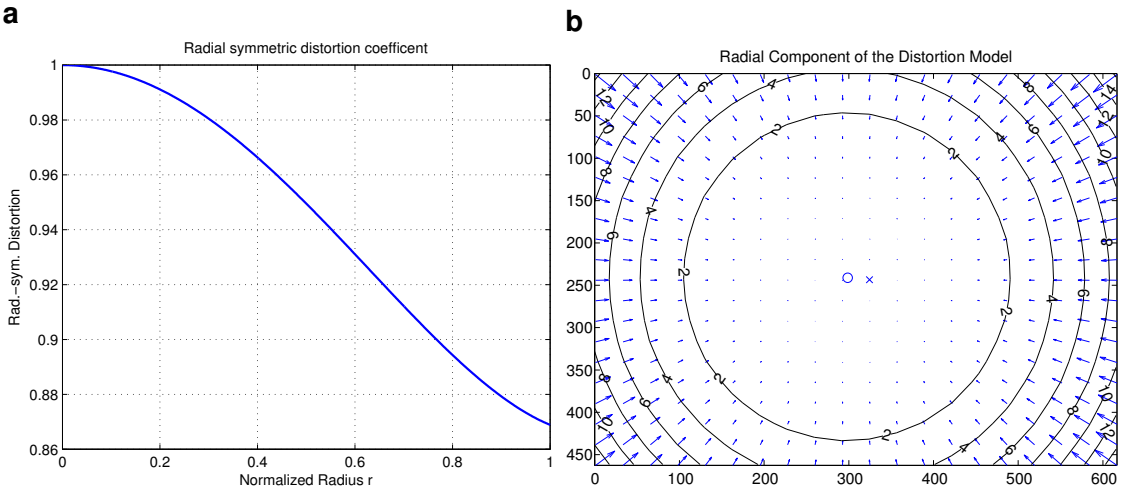

Figure 5.8.: **a** Radial symmetric distortion of a 8.00 mm optics as function of the normalized radius r. **b** Influence of the radial symmetric distortion on an image

Radial-asymmetric or tangential Distortion

The tangential distortion comes mainly from the misalignment of the lenses in the optics. Thus, for well-adjusted optics the tangential distortion parameters (k_3, k_4) is secondary. For our purpose the tangential distortion was taken into account although it was rather small. The tangential distortion vector $\boldsymbol{x}_{\text{tan}}$ is given as:

$$\boldsymbol{x}_{\text{tan}} = \begin{bmatrix} 2k_3 \cdot x_n \cdot y_n + k_4 \cdot (r^2 + 2x_n^2) \\ k_3 \cdot (r^2 + 2y_n^2) + 2k_4 \cdot x_n \cdot y_n \end{bmatrix} \tag{5.18}$$

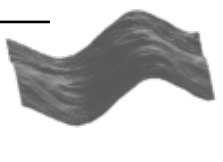

Total distortion model

The total distortion is then described by the sum of the radial distortion $\boldsymbol{x}_{\text{rad}}$ and the tangential one $\boldsymbol{x}_{\text{tan}}$. Another term could be added, which corrects for the affinity and shearing, but this is already included in the camera matrix $\boldsymbol{K}$, see Eq. (5.8). The total distortion is therefore:

$$\begin{aligned} \boldsymbol{x}_{\text{tot}} &= \boldsymbol{x}_{\text{rad}} + \boldsymbol{x}_{\text{tan}} \\ \begin{bmatrix} \boldsymbol{x}_{\text{px}} \\ 1 \end{bmatrix} &= \boldsymbol{K} \cdot \begin{bmatrix} \boldsymbol{x}_{\text{tot}} \\ 1 \end{bmatrix} = \boldsymbol{K} \cdot \begin{bmatrix} \boldsymbol{x}_{\text{rad}} + \boldsymbol{x}_{\text{tan}} \\ 1 \end{bmatrix} \end{aligned} \tag{5.19}$$

where $\boldsymbol{x}_{\text{px}}$ is the total distortion vector $\boldsymbol{x}_{\text{tot}}$ converted using the pixel coordinates of the image to the camera matrix $\boldsymbol{K}$. The effect of the total distortion model and of the tangential distortion can be seen in Fig. 5.9. As seen in the previous distortion map, the cross indicates the middle of the image and circle indicates the principal point. The arrows point from the ideal position to the distorted position of the image points. The contours show the shift in pixel. Hence a correction of the total distortion model would displace the image points from the tip to the shaft of the arrow.

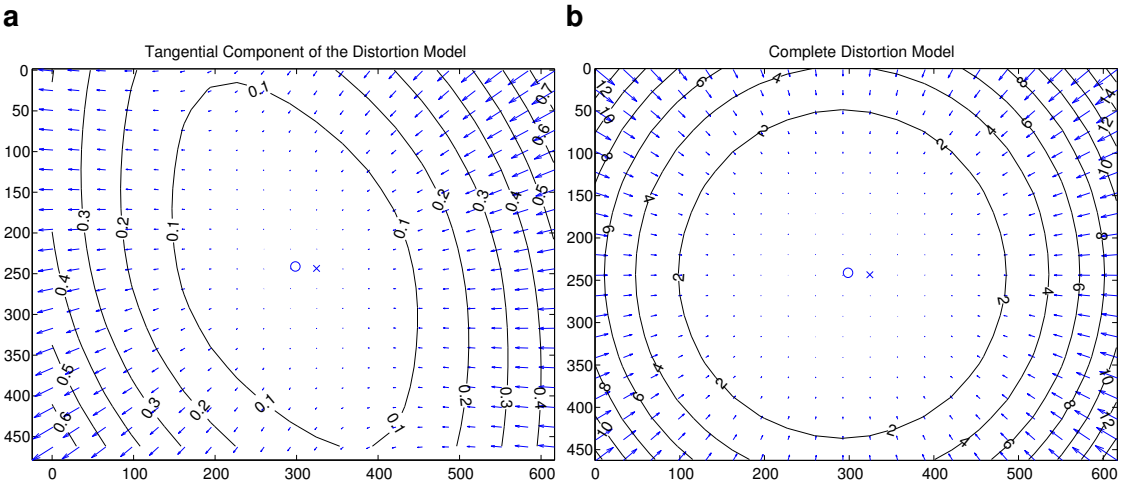

Figure 5.9.: Influence of **a** the tangential distortion and **b** the complete distortion, with radial and tangential distortion, on an image

To apply the total distortion model onto images, the shift of each pixel is calculated. Because the shift might not be on the same regular pattern as the pixel coordinates, some interpolation is necessary. The standard way is to use a linear interpolation, with four pixels as basis.

With the inclusion of the total distortion model in the transformation from world coordinates to pixel coordinates, the system becomes non-linear. Thus, it is not possible any longer to use a linear technique (like the Direct Linear Transformation DLT) to receive the parameters. The minimization process must be done by iteration, for example with a *Levenberg–Marquardt algorithm*. For our purpose we used the iterative optimization of the *Camera Calibration Toolbox for Matlab* (Bouguet, 2008) to obtain all 9 intrinsic parameters (5 from the camera matrix $\boldsymbol{K}$ and 4 from the distortion model). A table with all the parameters for all cameras can be seen in Tab. A.1 and Tab. A.2.

5.5. Calibration in Hanau

The normal calibration procedure with the *Camera Calibration Toolbox for Matlab* (Bouguet, 2008) requires taking about 10 to 15 pictures of a chessboard target in different orientations.

To obtain a good calibration result the chessboard should cover almost the full image size in the range of the depth-of-field. As shown in Tab. 4.3 the cameras were focused at a length of 11.14 m and the image size in the real world was $X = 3.97\,\text{m}$ and $Y = 2.97\,\text{m}$. Since we printed the chessboard on a plotter, the maximum size was DinA0 and hence it was not possible to cover the whole field with images of a chessboard at the focused distance. Prof. Jähne came up with the idea to build our own target with the correct dimensions, which was done at the Studiozentrum of *AEON*[1] in Hanau.

5.5.1. Target

The target is made out of three aluminum composite sandwich structure panels with a size of 3.1 m × 1.5 m. Black circles (made out of Metal Velvet[2]) were glued in a regular pattern ($\Delta x = \Delta y = 50.1\,\text{cm}$) at the top of the panels. At the middle panel a minor pattern ($\Delta x = \Delta y = 16.7\,\text{cm}$) with smaller circles is attached at the center. In each circle a white paper, which has a known emission characteristic, is applied, so that this target can also be used for radiometric calibration. The three panels were standing upright on the floor and were held by an aluminum rack. Fig. A.1 shows a 2D-graph of the target and Fig. 5.10 is a photo of it.

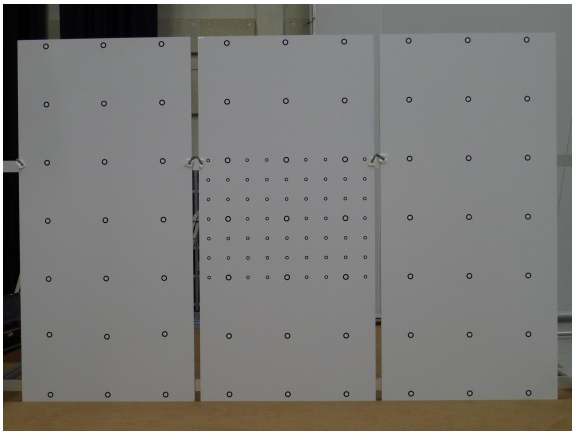

Figure 5.10.: Photo of the target in Hanau for the geometric calibration. (Large Pattern: $\Delta x = \Delta y = 50.1\,\text{cm}$, Small Pattern: $\Delta x = \Delta y = 16.7\,\text{cm}$)

5.5.2. Linear Translation Axis

One of the most difficult parts in camera calibration is to find the principal point of the camera. Therefore Prof. Jähne had the idea, whenever a camera is moving onto a target in a straight line the projection of the points must move on a straight line away from the principal point. Therefore the cameras were installed on a 3 m long linear translation axis, to move them on a straight line towards the target. The linear translation axis system consists of a Parker Compax3[3] control box, a brushless servo motor and a 3 m long linear axis[4]. A photo of the linear axis with the cameras and a sketch of the whole setup in Hanau is depicted in Fig. 5.11.

[1] AEON Verlag & Studio GmbH & Co. KG, http://www.aeon.de
[2] Ultra-Diffusive Light-Absorbing Foil UV, VIS and IR, http://www.acktar.com/category/products/lights-absorbing-foils/ultra-diffusive
[3] Parker C3S025V2F11I12T11M00, http://www.parker.com
[4] Motor: Parker SMH8260038142ID65A7, Linear-axis: Parker LCB060SG03000SRN, Gearbox: PTN080-004S7

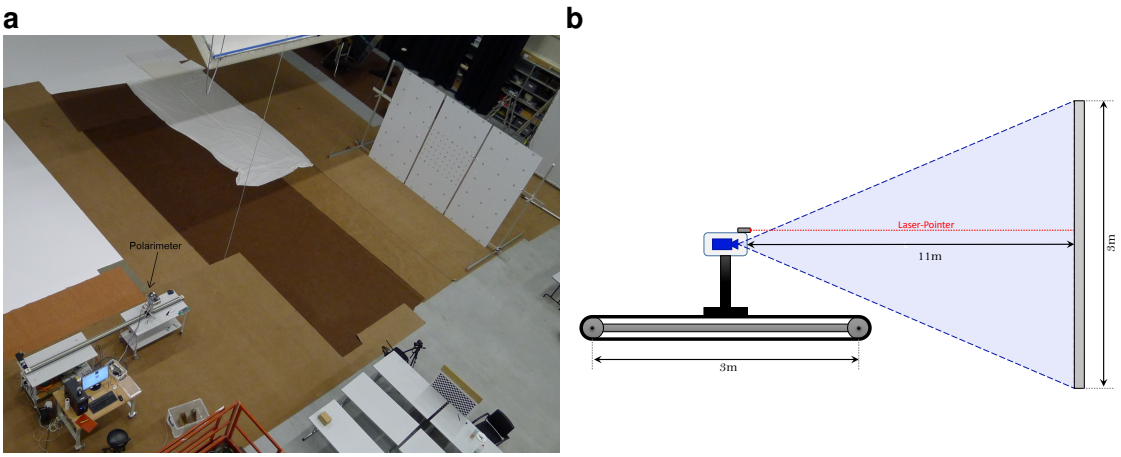

Figure 5.11.: **a** Photo and **b** sketch of the measurement setup in Hanau with the camera box on the linear axis facing at the target

Wobble Correction

Due to the large distance from camera to target, even tiny changes in the camera's viewing angle had notable effects on the position of the target in the image. Since the camera was supposed to move in a straight line towards the target, this wobbling had to be corrected. The laser pointer shown in Fig. 5.11 provided a stable reference point that had a fixed position in the camera image, but was subject to the same wobbling. Thus, by tracking the position of the laser pointer on the target, it is possible to determine the changes in the viewing angle. In practice, it was not trivial to determine the position of the laser spot, the cheap laser diode that was used was badly focused and had an irregular shape. Therefore, virtual points were used. A typical calibration image sequence consists of 59 images from different positions of the linear translation stage. The parameters for the wobble correction then were determined like this:

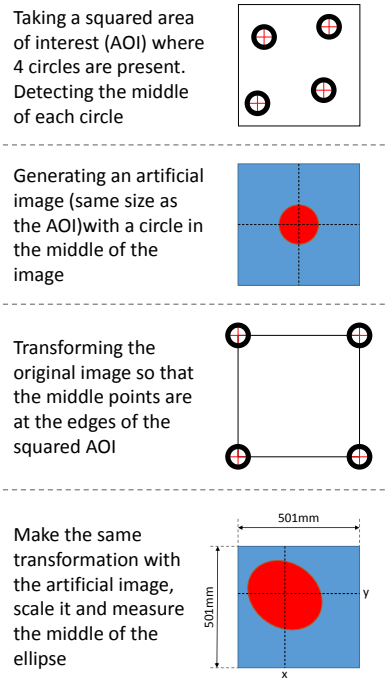

Figure 5.12.: Wobble Correction

1. An area of interest (AOI) was selected such that the same 4 circles are visible in all images of the sequence.
2. The centers of the circles were detected.
3. An artificial image with the same size as the AOI was generated with a circle in the middle (fixed point in the camera).
4. Using a perspective transformation, the image can be warped in a way that the 4 circle centers are the corners of the warped image.
5. The same transformation is applied to the artificial image (circle → ellipse).
6. The transformed artificial image is scaled to the same dimensions as the square pattern of the target ($\Delta x = \Delta y = 501\,\mathrm{mm}$).
7. The center of the ellipse is determined, which represents the fix point at the target.

After this was done for every position of the linear axis a line was fitted to the $X-$ and $Y-$data as a function of the position. Due to the *intercept theorem* (projective transformation, Sec. 5.2.1) the projection of a point must move on a line when the camera is moving on a straight line towards this point. The correction factors $(X_{\text{corr}}, Y_{\text{corr}})$ were calculated by subtracting the $X-, Y-$values of the straight line from the $X-, Y-$data. The wobbling and the line fit is shown in Fig. 5.13.

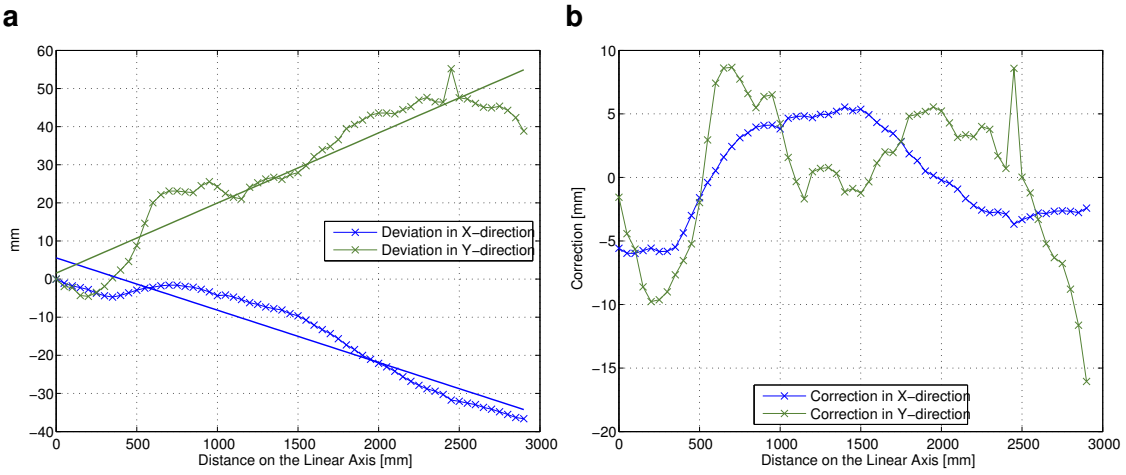

Figure 5.13.: **a** Wobbling of the linear axis in X- and Y-direction for every step of the linear axis. For the correction a linear fit is made. **b** Correction of the wobbling by subtracting the linear fit.

5.5.3. Detection of the Target

The implementation of the target detection was done in Heurisko® and in Matlab®. As it is shown in Fig. 5.11, the cameras are always facing head-on the target. This has one big advantage and one big disadvantage. The advantage is that circles always remain circles and do not transform to an ellipse. Thus, it was possible to use the Matlab®-Function *imfindcircles*.

Since the wobbling of the linear axis was very prominent in the images, it was not possible any more to use the first idea with the principal point. Therefore, we tried to use the *Camera Calibration Toolbox for Matlab* on this data. Because the target was always aligned parallel to the image sensor, it was not possible to use it as a planar target. Zhang (1998) showed that the standard calibration procedure with planar targets is not working any more if the planar target is always facing the camera with the same orientation.

The solution of this problem was to generate a 3D point cloud out of the real world coordinates of the planar target and the known translation of the linear axis. For every position of the linear axis the real world coordinates of the target were corrected as well by shifting the $X-, Y-$coordinates with the wobbling parameters $(X_{\text{corr}}, Y_{\text{corr}})$. With this approach it was possible to calibrate all cameras with the 16 mm-lens configuration. The intrinsic parameters of the calibration can be seen in Tab. A.2.

5.6. Polarization Filter Calibration

As mentioned in Sec. 3.1, the polarization filters of one polarimeter have to be aligned at $\theta = 0°$, 60° and 120° to cover the full range of 180°. The calibration of the orientation of the polarization filter was done with the integrating sphere with a polarization filter attached. Since the polarization filter of the integrating sphere had no degree scale, it was necessary to calibrate the orientation of this polarization filter as well. The knowledge of Sec. 3.2, that reflected light

is fully horizontally polarized at the Brewster angle, was used to do the gauging of the polarization filter. The reflection at the Brewster angle of the integrating sphere was acquired with a camera. A degree scale, determined by the radius of the polarization filter, was mounted on the polarization filter and the zero point of the scale was set where the reflection was the brightest. The zero point of the scale at the polarization filter of the integrating sphere is therefore set to horizontal polarization.

For the rough adjustment of the polarization filter of the three cameras to 0°, 60° and 120° the corresponding angle was set at the integrating sphere filter. Afterwards the filter in front of the camera was turned to the darkest position. This means e.g. the 0°-filter is vertically polarizing, since the zero position of the integrating sphere is horizontally aligned.

For the accurate measurement of the polarization filter adjustment the filter at the integrating sphere was turned from $0° - 195°$ in 5° steps and pictures were taken at every position of the polarization filter. The analyzer matrix $\boldsymbol{A}$ (see Sec. 3.1 and Eq. 3.3) for each box was determined using a least squares fit of Eq. 5.20, where I_k are the intensity from camera k and S_i $(i = 0,1,2)$ are the calculated components of the Stokes vector (see. 2.2.2).

$$\begin{bmatrix} I_1 \\ I_2 \\ I_3 \end{bmatrix} = \boldsymbol{A}^{-1} \cdot \begin{bmatrix} S_0 \\ S_1 \\ S_2 \end{bmatrix} \tag{5.20}$$

The Stokes-vector $\boldsymbol{S}$ is computed from the angle of the polarization filter θ_{pol} at the integrating sphere like this:

$$\begin{bmatrix} S_0 \\ S_1 \\ S_2 \end{bmatrix} = \begin{bmatrix} 1 \\ \cos(2\theta_{\text{pol}}) \\ \sin(2\theta_{\text{pol}}) \end{bmatrix} \tag{5.21}$$

An example of the measured intensities and with the calibrated $\boldsymbol{A}$-matrix and Stokes vector calculated intensities can be seen in Fig. 5.14. The crosses are the measured values and the continuous lines are the calculated values with Eq. (5.20). The polarization angle Φ is defined by the polarization filter of the integrating sphere.

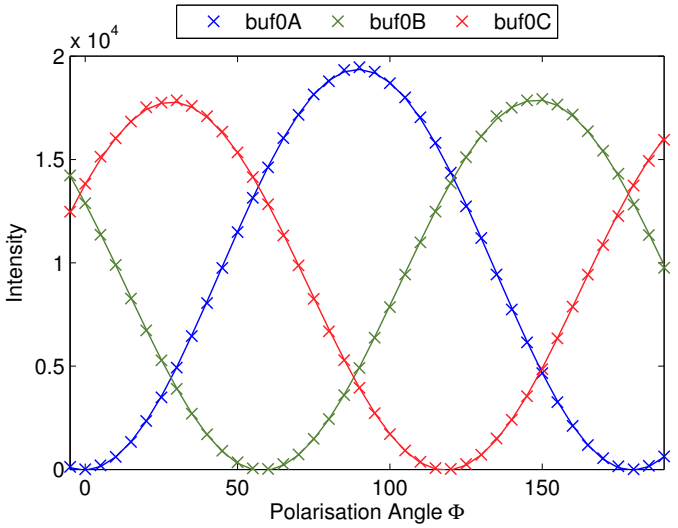

Figure 5.14.: Intensities of the different cameras with different polarization filters facing the polarization filter of the *integrating sphere*. The crosses indicate the measured values and the continuous lines are the calculated values with Eq. (5.20).

5.6.1. Test of the Polarization Filter Calibration

To verify the polarization filter calibration of the polarimeter, a special test was designed. A sketch and a photo of the experimental setup is shown in Fig. 5.15.

The reflection of an integrating sphere (without polarization filter) at the water surface was recorded for different incidence angles. The polarimeter was put on a rack with an angular adjustment stand. For a precise measurement of the angle a spirit level was fixed on the top of the box. The cameras were directly facing a water tank, where the ground was covered by black fabric, so no upwelling light (see Sec. 3.5) could come from the bottom of the tank. The integrating sphere was placed such that the reflection could be seen by the cameras.

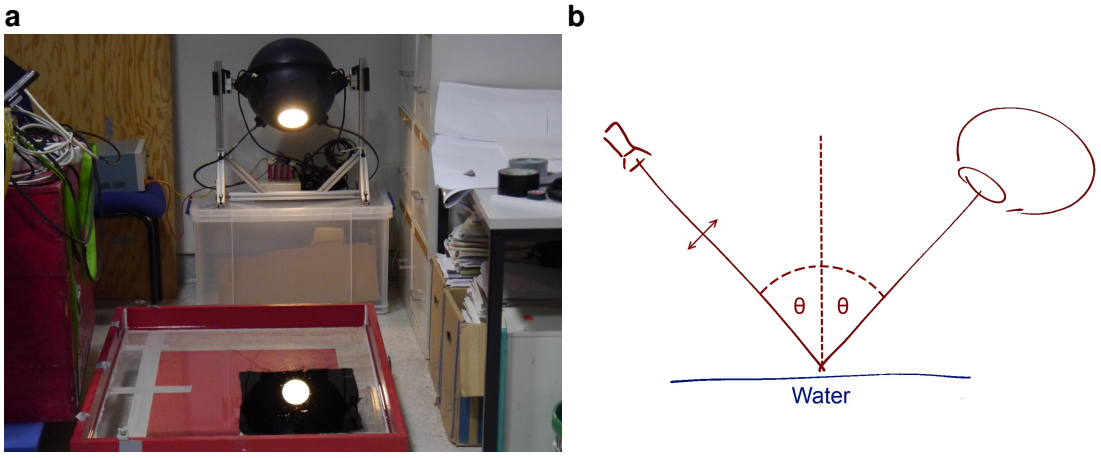

Figure 5.15.: a Photo and **b** sketch of the polarimeter test. The *integrating sphere* is shining onto the water surface without any filter attached to it. The camera is installed under a certain angle to the water surface and is capturing the reflection of the *integrating sphere*.

The incidence angle was adjusted from 30° to 75° in steps of 5° and the degree of linear polarisation was computed for the reflection of the integrating sphere. For matching the images of the cameras, a chessboard was put on the water surface for every condition. Since the Brewster angle of 53° is passed, when the incidence angle is varied from 30° to 75°, the two parts (left and right of the Brewster angle) of the DOLP curve Fig. 3.1 have to be taken into account. Below the Brewster angle the left part and above the right part is important.

Since the reflection was not always at the same position in the image the angle of view α of the camera has to be considered. The angle of view is depending on the optics and on the pixel position and can be calculated like this:

$$\alpha_{\text{ypos}} = \arctan\left(\frac{y_{\text{pos}} - cc_y}{f}\right) \tag{5.22}$$

Here α_{ypos} is the angle of view in Y at a certain position, y_{pos} is the y-position of the reflection, cc_y is the principal point or middle of the image in y-direction and f is the focal length. The same can be done in x-direction. The angle of view was computed for every position, by using the *center of gravity* of the reflection as pixel position.

Figure 5.16 shows the result of the polarization filter test, where Fig. 5.16a depicts the relation DOLP - incidence angle with and without the angle of view correction. Fig. 5.16 plots the quality of the polarization filter test, where the measured angle is compared to the adjusted angle.

This test demonstrates as well that it is possible to use both parts of the DOLP curve Fig. 3.1 (above and below the Brewster angle) for the reconstruction of the incidence angle. In practice it is not really useful to use both parts, since it is not possible to distinguish whether the Brewster angle is passed, like here in this experiment.

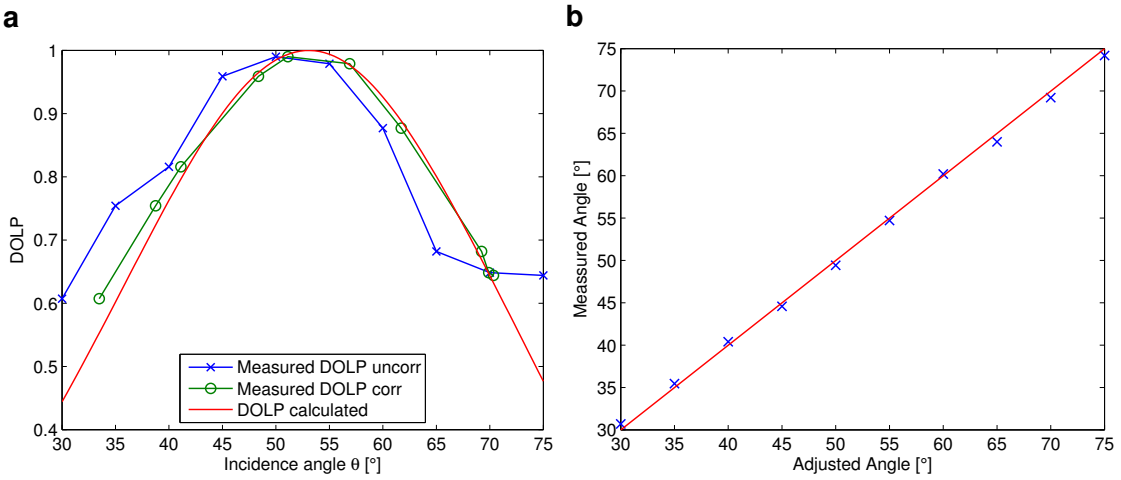

Figure 5.16.: a Plot of degree of linear polarisation (DOLP) for different adjusted angles of the camera. The blue line shows the result of the measurements when the angle of view and the position of the reflection is not taken into consideration whereas in the green one, this effect is corrected. The red curve is a theoretically calculated curve. **b** Relation between the measured angles and the adjusted angles.

6. Data Processing

The principle of the polarimeter data processing chain, from taking the picture of the 3 cameras to the X-, Y-slope images, is shown in Fig. 6.1. To illustrate the data processing steps, an example set of images will be shown in some sections. The conversion from the slope distributions to the height images is described in Sec. 6.6.

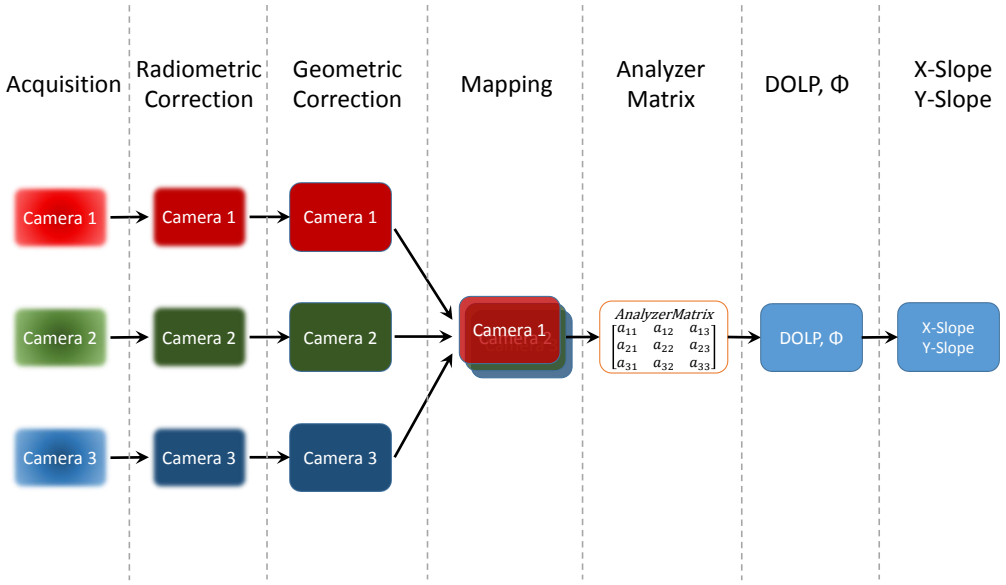

Figure 6.1.: Figure Data Processing Block diagram

6.1. Data Acquisition

The three cameras of the polarimeter were acquired at the same time. The acquisition frequency and the resolution of the different measurements can be seen in Tab. 4.3 and Tab. 4.5. An example set of 3 images from the measurements in Hamburg can be seen in Fig. 6.2.

The contrast of the images in Fig. 6.2 were adjusted to the same range.

6.2. Radiometric Correction

A two point correction was done for every acquired images by subtracting a dark image Fig. 5.5 (Sec. 5.4.2) and dividing by the field darkening images Fig. 5.4 (Sec. 5.4.1). With this correction different offsets and sensibilities of every pixel were adjusted. Especially the correction of the field darkening is very important for the polarimeter, because we want to compare different intensities for every pixel.

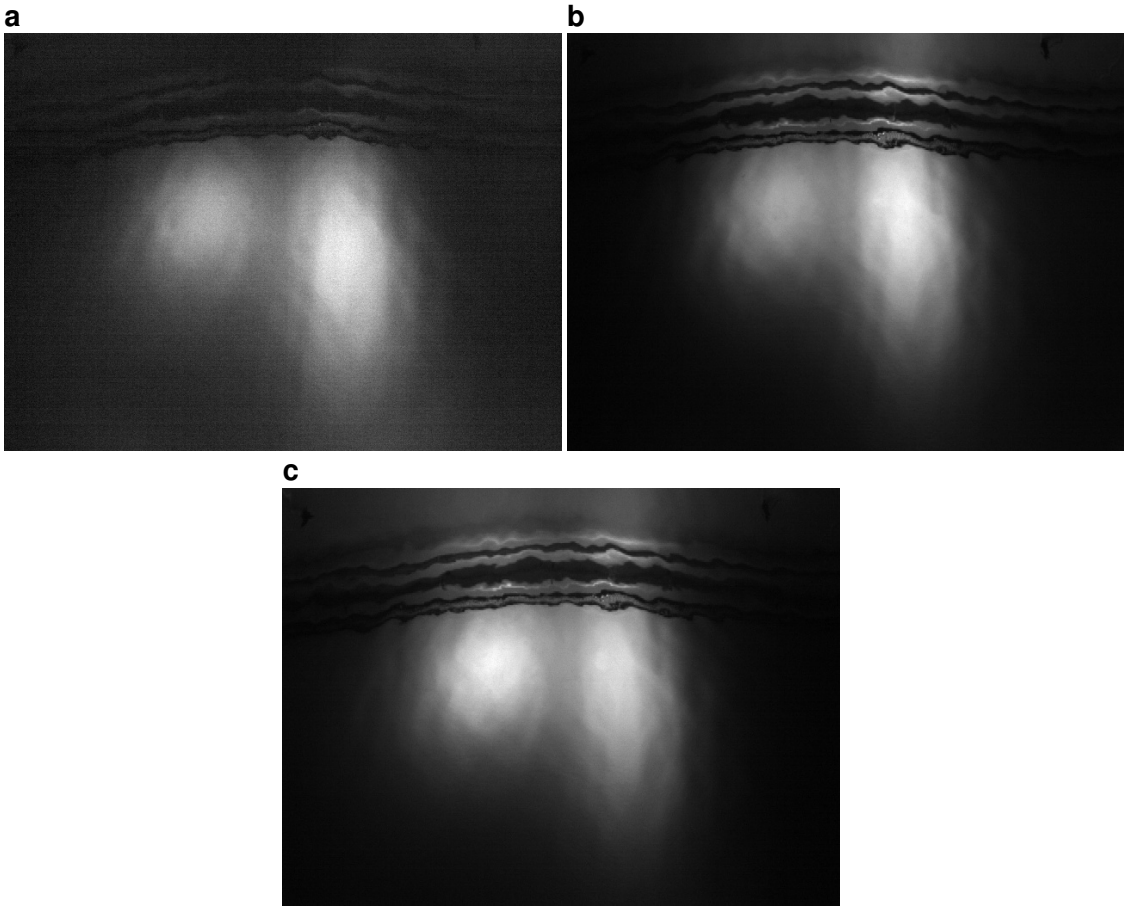

Figure 6.2.: Example raw images acquired from the 3 different cameras of a polarimeter with the polarization angle of **a** = 0° **b** = 60° **c** = 120°

6.3. Distortion Correction

Like the radiometric correction the distortion correction has to be done for every camera individually, since every lens and camera sensor is different adjusted. Especially the 8 mm optics in the experiments at the HSVA have not negligible distortion, which can be seen in particular at the edges of the images. The determination of the distortion parameters (two radial and two tangential) is done like in Sec. 5.4.4 described. The parameters for every setup can be looked up in Tab. A.1 and Tab. A.2. The distortion correction was done with the modified *rect*-routine of the *Camera Calibration Toolbox for Matlab* (Bouguet, 2008). Because the distortion correction is computationally extensive, the resulting images after the radiometric and distortion correction were saved for every data set. Therefore all further steps in the data processing chain could start with corrected images.

6.4. Mapping of the Images

The three cameras look from a slightly different position and a different perspective on the water surface. Hence, it is not possible to map the different images by a simple translation. To align the three images exactly pixel by pixel, two homographies (or projective transformations, see Sec. 5.2.1) where calculated, to map the outer cameras to the middle camera. In the same step the images were transformed to an orthogonal coordinate system. This is significant, because the cameras were looking under 37° at the water surface and hence the image section is

not rectangular. The rectification is as well a projective transformation (Sec. 5.2.1). At the HSVA experiment, the parameters of the transformation are determined by an chessboard floating on the water. The chessboard was as well important to calculate the dimensions of one pixel on the water surface. Figure 6.3 shows an example result of the mapping of all cameras of one box in RGB-colour coding.

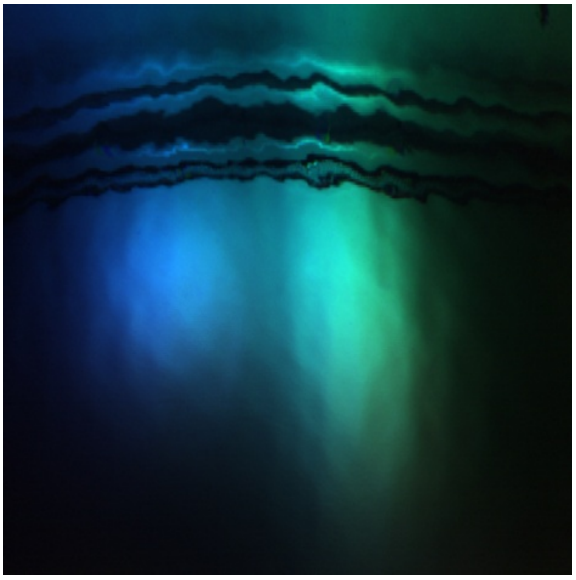

Figure 6.3.: Example image of the mapping process. The three cameras are shown in RGB-coding.

6.5. Calculation of the Slope Distribution

After the mapping we get at every pixel position the three intensities, which were taken with different polarization filter directions. These intensities can be converted with the calibrated analyzer matrix to the three components of the Stokes vector, see Sec. 3.1 and Eq. (3.3). With the components of the Stokes vector the orientation angle Φ and the degree of linear polarisation(DOLP) were calculated, see Sec. 2.2.2, Eq. (2.49) and Eq. (2.45). The non-linear transformation from DOLP to incidence angle θ_i (see Sec. 3.2) was done with a look-up table. With the angle of incidence θ_i and the orientation angle Φ the slope in X- and Y- direction (s_x, s_y) were calculated Eq. (3.11). Figure 7.3 and Fig. 7.6 display example images of DOLP and the orientation angle Φ. In Fig. 7.4 and Fig. 7.7 the slope in X- and Y-direction of the before shown images can be seen.

6.6. Calculation of the Height Distribution

With the two slope images (s_x, s_y) the surface elevation can be reconstructed with the algorithm developed by Frankot and Chellappa (1988). The principle of this algorithm is shown in Sec. 3.4. Because the algorithm is based on a Fourier transformations the slope images have to be cleared of *NaNs*, since the Fourier transformation is not working with *NaNs*. The *NaN* reconstruction algorithm will be depicted in the next section.

The reconstructed height is then given in pixel and must be scaled with the pixel scale that is evaluated in Sec. 6.4. An example of a reconstructed height can be seen in Fig. 7.5 and Fig. 7.8.

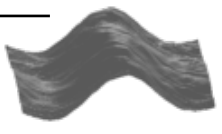

6.6.1. NaN-Reconstruction

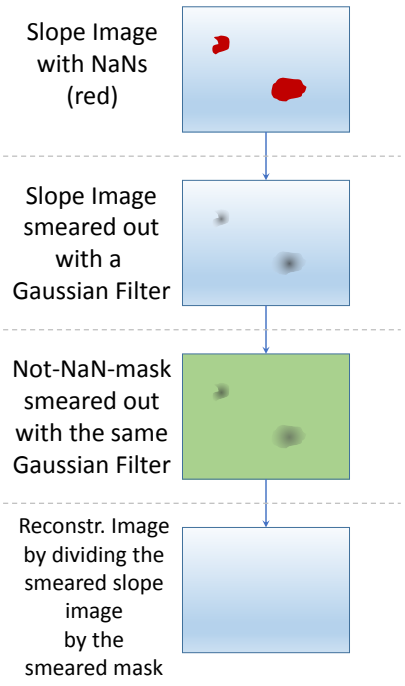

Figure 6.4.: Block diagram of the NaN-Correction

In many slope images there are *NaNs* in the data, because of too high DOLP values (see Sec. 7.2.2) at the transformation from DOLP to incidence angle. Since the *FFT (Fast Fourier Transformation)* cannot deal with *NaNs*, we have to get rid of them. The simple solution is to set all *NaNs* to zero. This means for the reconstructed height, that it stays at the same level, were the slop is zero. Another approach is to fill the *NaNs* by smearing the slope images so that the *NaNs* get filled up. The process of the reconstruction is described below.

NaN-Correction

1. Detection of the *NaNs* in a slope image and generating masks (NaN-mask and Not-NaN-mask)
2. Smearing the slope image with a Gaussian filter.
3. Smearing the Not-NaN-mask with the same Gaussian filter.
4. Correct the effect of darkening in the middle of a big hole by dividing with the smeared Not-NaN-mask.
5. Use the original image and fill the *NaNs* with the corrected image

6.7. Timing of the Data Processing

The analysis of the polarimeter can in principle be done online (in real time) if the system is calibrated in advance. Therefore the timing of all processes is very critical. Thus a timing of the different steps of the data processing was made and listed in Tab. 6.1. The calculations were done with Matlab® on a PC with *Intel® Core™ i7-3820 Processor* with 3.60 GHz and 64 GB of RAM. The time estimation is done with a data set of the Hamburg experiments with 3000 images. The initial size was 648 × 486 pixel and the final size was 486 × 470 pixel.

Table 6.1.: Timing of the different data processing steps. The times are given to process an image triples from 3 cameras (Resolution: 648×486 pixel) to the output parameters (s_x, s_y, h) (Resolution: 486×470 pixel).

Data Processing Step	3000 Triples	1 Triple
Calibration (radiometric and geometric, Sec.6.2 and Sec.6.3)	160.14 s	53.38 ms
Mapping, Analse Matrix, DOLP and X-,Y-slope (Sec.6.4 and Sec.6.5)	81.69 s	27.23 ms
NaN- and Height-Reconstruction (Sec.6.6)	90.77 s	30.26 ms
Total	332.60 s	110.87 ms

7. Results

7.1. Results of the Meteor

As described in Sec. 4.1 the Stereo Polarimeter was barely tested before it was used on board of the ship. Therefore most of the calibration had to be done afterwards. In Sec.4.3 it is mentioned that chessboard pictures were taken to calibrate the stereo system. Since the polarimeter was my only area of responsibility of the Stereo Polarimeter, the stereo calibration and the stereo data analysis aren't processed until now. As all reflections are specular at the water surface (see Sec. 3.2), it is not possible to use standard stereo algorithms (Jähne et al., 1994). The main difficulties of the stereo analysis will be that the illumination from the sky was very inhomogeneous and the sea surface roughness was too low most of the time, so that there is not enough structure for stereo matching.

It turned out that the analysis of the polarimeter data is challenging as well. First and foremost we do not have the possibility to place a chessboard at the water surface, like in the experiments in Hamburg (see Sec. 6.4). Therefore we had to map the three images of one polarimeter box with the calibration data from Hanau (Sec. 5.5). Since the cameras were tilted at the ship, we cannot obtain the exact mapping and the exact scale from this calibration. This problem can in principle be fixed with some height data from the RSSG[1] or from the stereo system. Another difficulty of the *Meteor* data is the stereo effect between the three cameras of the polarimeter. Although if the polarimeter was located 11.14 m from the mean sea surface, the stereo basis of 3.5 cm (Sec. 4.2) from one camera to the next one was sufficient to see a parallax effect in the images.

To estimate the stereo effect in the images, the change of the disparity is calculated. The starting point is the Equation of disparity or parallax, see Jähne (2005, p. 221, Eq. (8.3))

$$p = \frac{b \cdot f}{X_3} \tag{7.1}$$

where p is the disparity in pixel, b is the length of the stereo basis, f is the focal length in pixel and X_3 is the distance from the cameras to the object. To calculate the change of disparity when the length of the line of sight changes, we have to differentiate the disparity.

$$\frac{dp}{dX_3} = -\frac{b \cdot f}{X_3^2} \tag{7.2}$$

With the data from Tab. 4.3 and Tab. A.2 ($b = 3.5\,\text{cm}$, $f = 7273\,\text{px}$ taken from the camera calibration, $X_3 = 11.14\,\text{m}$) we obtain for the change of disparity:

$$\left|\frac{dp}{dX_3}\right| = 2.1\,\text{px/m} \tag{7.3}$$

This means, that for a wave magnitude of only 0.5 m, a stereo displacement of 1 px appears between two nearby cameras. The waves on the ocean were definitely higher and therefore this effect cannot be ignored.

[1] Reflective Stereo Slope Gauge: Kiefhaber et al. (2011)

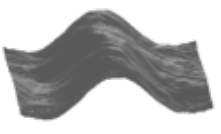

To illustrate the stereo effect Fig. 7.1 shows a mapped image of all three cameras in RGB color coding. In the upper part of the image a shift occurs, whereas in the lower part the shift is barely visible. This is hard to see with naked eye, hence two profiles from bubbles were taken in the upper and lower part in the image. The stereo effect appears as a shift of the peak in Fig.7.2.

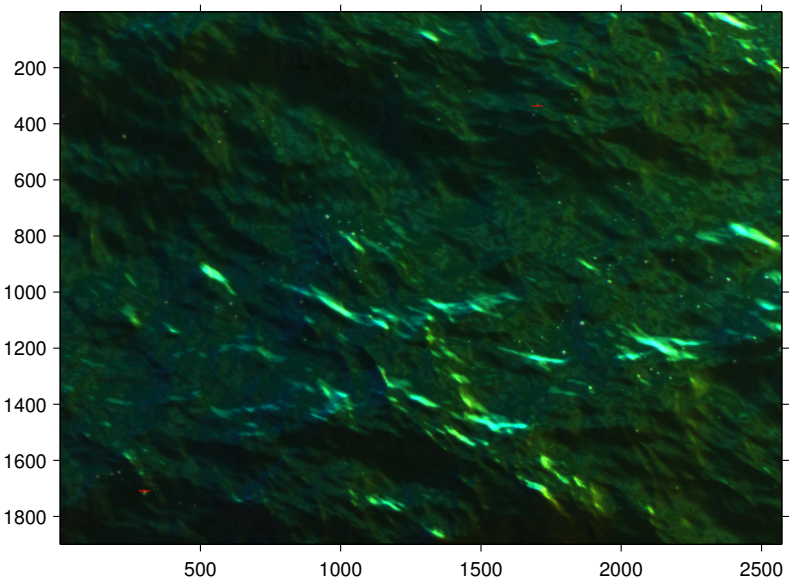

Figure 7.1.: Matched example image from the Meteor data illustrated in RGB-colors for the three different cameras. The red lines in the upper and lower part of the image indicate the position where a profile was taken. The profiles are shown in Fig. 7.2.

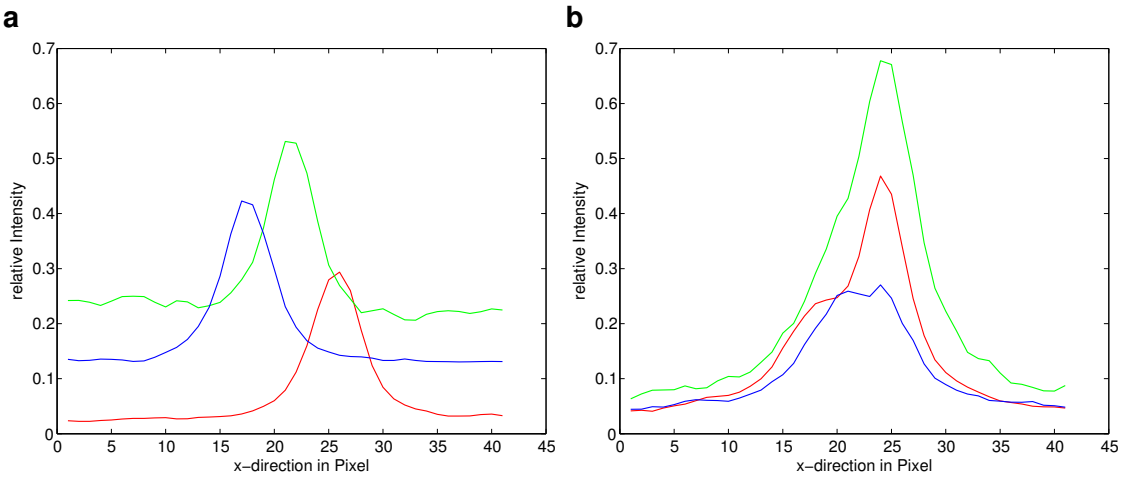

Figure 7.2.: Profiles in x-direction taken from bubbles in image Fig. 7.1. **a** Profile from a bubble from the upper right-hand side **b** Profile from a bubble from the lower left-hand side. The green line represents the middle camera. Between these two profiles due to the shift from the stereo effect can be seen here.

The stereo effect can in principle be corrected, if we know the declination of the ship and the exact surface elevation, like from the stereo measurements or from the RSSG measurements.

As mentioned in Sec. 3.5, the polarization and luminosity of the incoming light has to be considered. Since it is not possible to install an artificial light source which is large enough in front of the ship, all measurements have to be done during day time. During day time the measurements can be distorted due to the polarization of the clear sky (see Sec. 3.2.1). The polarization of the incoming light can be diminished by a cloud cover, which was unfortunately very rare at the *Meteor* 91 cruise. Another approach is to take the incoming polarization into

account with a Rayleigh sky model or to measure the polarization with a polarimeter facing the sky. The latter one is not possible any more for this data set. Solving all these problems was beyond the scope of this thesis.

7.2. Results from Hamburg

The conditions at the towing tank in Hamburg, where a mechanical wave generators was used, were completely different than on the *Meteor*. The waves were mainly moving into one direction (see Sec. 4.5.1), because they were not wind driven. Since the waves were very smooth and had a relatively long wavelength, it was possible to reduce the resolution of the cameras (according to the constraints Sec. 3.5) with a *4x4 binning modus* (see Sec. 4.5). With a reduced resolution and a maximum wave amplitude of 0.15 m it was possible to ignore the stereo effect, which was visible in the *Meteor* data. A sufficient illumination in the laboratory was important (see Sec. 3.5 and Sec. 4.5.1), but the *binning mode* was beneficial for the gathering of light. Before all experimental conditions will be discussed in Sec. 7.2.2 a set of example images will be shown. The images are the result of the data processing chain in Sec. 6.

7.2.1. Example Images

A set of example images of the polarimeter are displayed in the following paragraph. All example images are taken from the same series *HSVA15_001*. The monochromatic water waves of this series are always moving from the right to the left in the images. The degree of linear polarisation images and polarization angle Φ images are shown in one set and the slopes in X- and Y-direction (s_x, s_y) are displayed as pair. Attention has to be paid to the scale of the images, since the scale for the X-slope s_x is from -0.3 to 0.3 (in degrees: $\tan^{-1} 0.3 = 16.7°$) and for the Y-slope s_y from -0.2 to 0.2 (in degrees: $\tan^{-1} 0.2 = 11.3°$). The elevation map of the surface given in centimeters is reconstructed from the two slope images (s_x, s_y) (see Sec. 6.6).

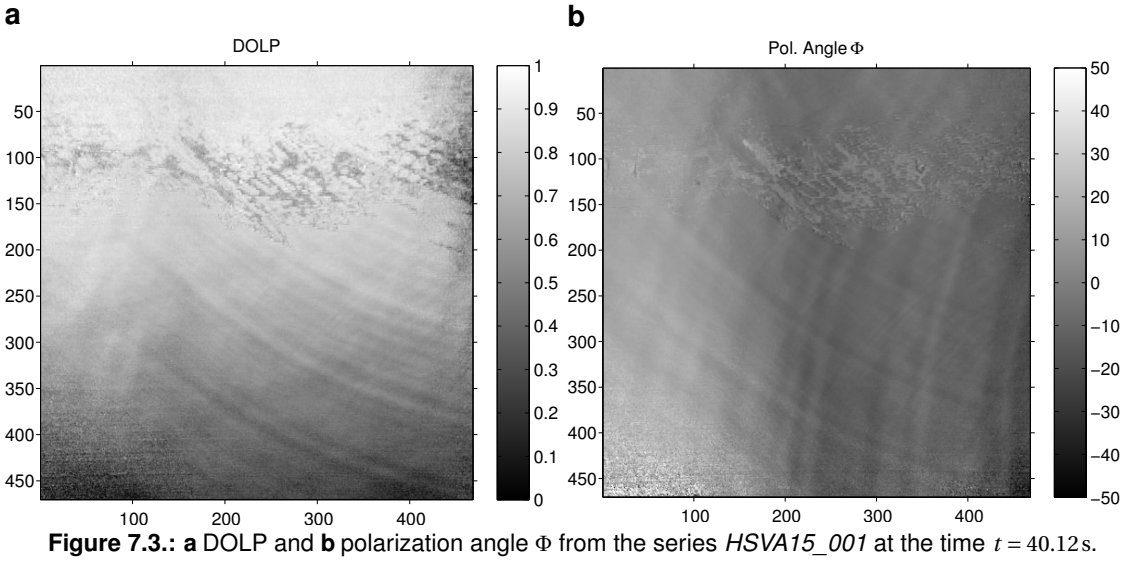

Figure 7.3.: a DOLP and **b** polarization angle Φ from the series *HSVA15_001* at the time $t = 40.12\,\mathrm{s}$.

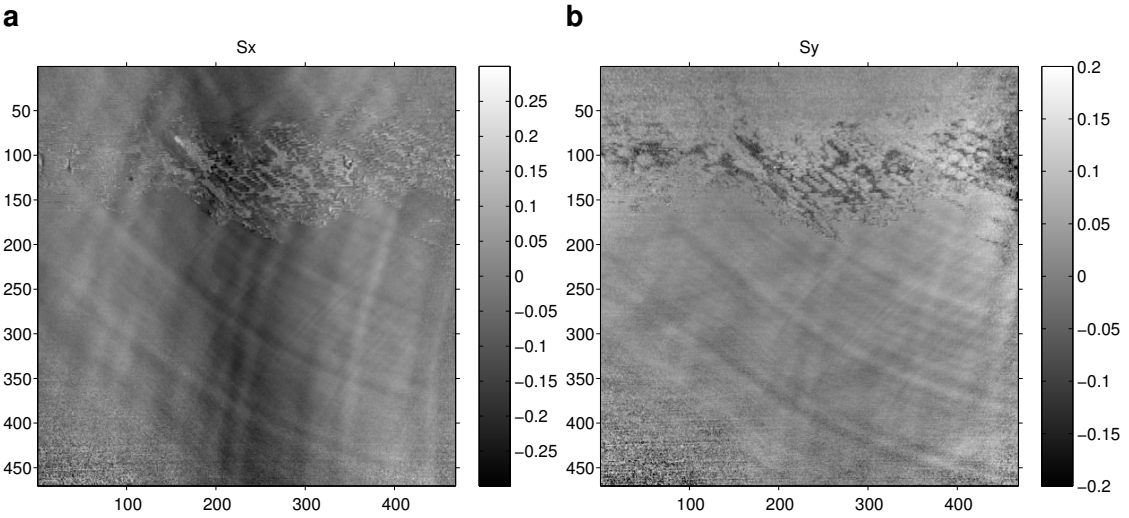

Figure 7.4.: Slope in **a** X-direction s_x and **b** Y-direction s_y from the series *HSVA15_001* at the time $t = 40.12\,\mathrm{s}$.

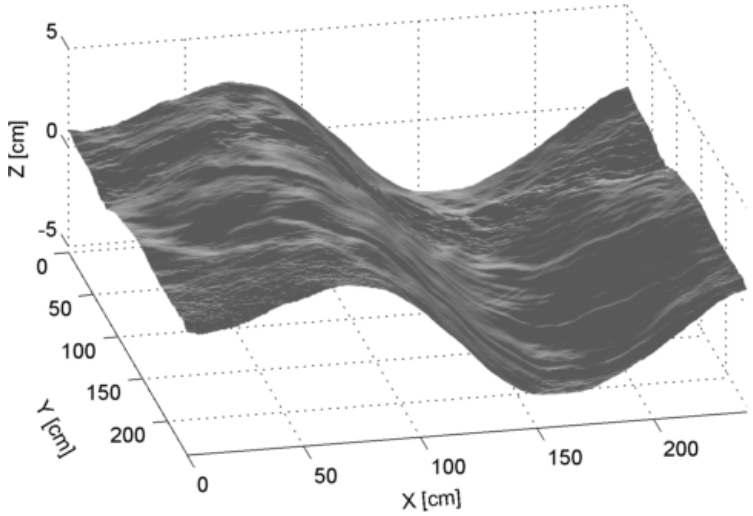

Figure 7.5.: Example image of the reconstructed height from the series *HSVA15_001* at the time $t = 40.12\,\mathrm{s}$.

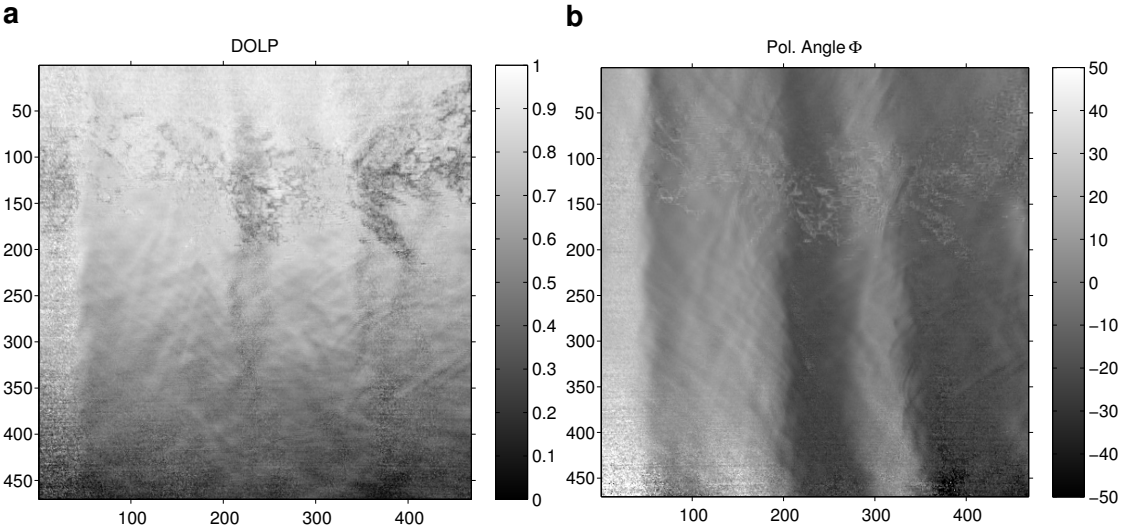

Figure 7.6.: **a** DOLP and **b** polarization angle Φ from the series *HSVA15_001* at the time $t = 52.0\,\mathrm{s}$.

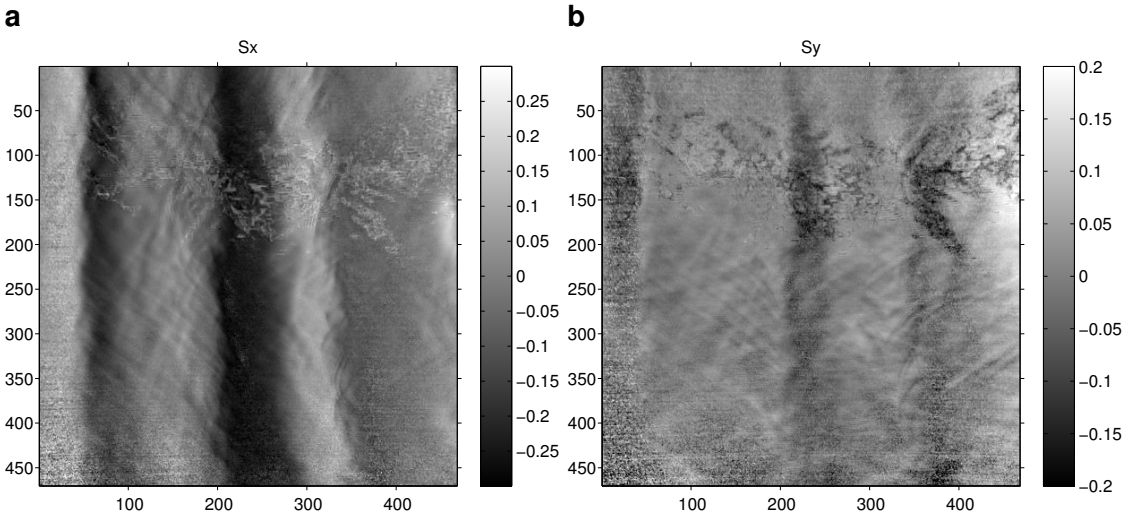

Figure 7.7.: Slope in **a** X-direction s_x and **b** Y-direction s_y from the series *HSVA15_001* at the time $t = 52.0\,\mathrm{s}$.

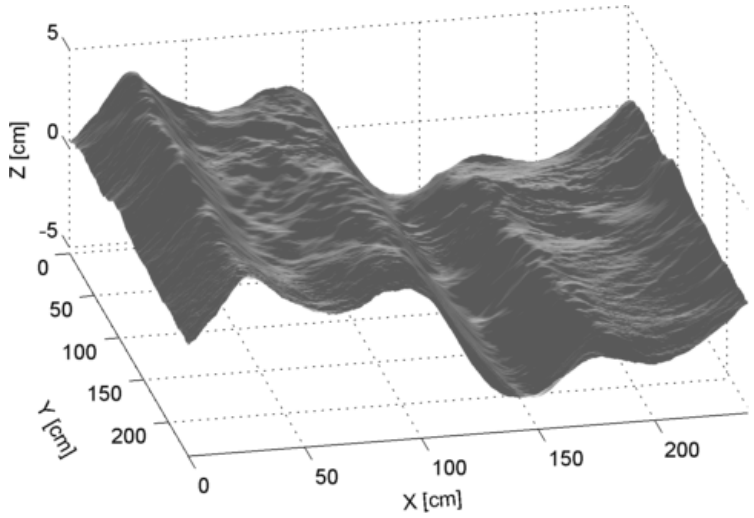

Figure 7.8.: Example image of the reconstructed height from the series *HSVA15_001* at the time $t = 52.0\,\mathrm{s}$.

7.2.2. Experimental conditions

Illumination

To obtain correct results from polarimetric slope imaging measurements the incoming light plays an important role, like it is shown in Sec. 7.2.6. For illumination, we installed two LED-Spotlights (see Sec. 4.5.1), facing the ceiling in order to widen the illuminated area. The illuminated area was still too small, which can be seen as dark spots in the image corners. With this lack of illumination it is not possible to obtain qualitatively good results. Figure 7.9 shows an example image of the degree of linear polarisation, where the noise becomes very large especially in the lower image corners.

The illumination area plays as well an important role for steep waves with a high curvature. A steep surface reflects the light from a spot, where the illumination source does not extend to. This causes high noise levels in these areas.

To quantify the lack of illumination, we can compute the effect of the noise in the raw images on the noise in the processed DOLP images. In the area marked by the red square in Fig. 7.9,

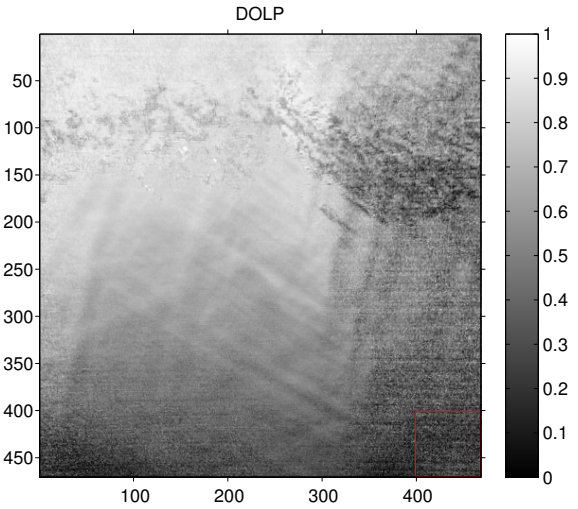

Figure 7.9.: Example image of the degree of linear polarisationof the series *HSVA15_001*. Attention should be paid to the noise at the lower image corners, which comes from a lack of illumination.

the absolute error (in gray values) in the mapped raw images is:

$$\begin{bmatrix} \sigma_{I1} \\ \sigma_{I2} \\ \sigma_{I3} \end{bmatrix} = \begin{bmatrix} 151.98 \\ 131.67 \\ 135.51 \end{bmatrix} \tag{7.4}$$

With the propagation of uncertainty (Eq. (3.3)) we obtain for the error of the stokes vector.

$$\begin{bmatrix} \sigma_{S0} \\ \sigma_{S1} \\ \sigma_{S2} \end{bmatrix} = \sqrt{\left(\boldsymbol{A} \cdot \begin{bmatrix} \sigma_{I1} \\ \sigma_{I2} \\ \sigma_{I3} \end{bmatrix} \right)^2} = \begin{bmatrix} 0.0179 \\ 0.0275 \\ 0.0235 \end{bmatrix} \tag{7.5}$$

The propagation of uncertainty can also be evaluated for DOLP (Eq. (2.49)):

$$\sigma_{DOLP} = \sqrt{\left(\frac{\partial DOLP}{\partial S_0} \cdot \sigma_{S0} \right)^2 + \left(\frac{\partial DOLP}{\partial S_1} \cdot \sigma_{S1} \right)^2 + \left(\frac{\partial DOLP}{\partial S_2} \cdot \sigma_{S2} \right)^2} \tag{7.6}$$

where

$$\frac{\partial DOLP}{\partial S_0} = -\frac{\sqrt{S_0^2 + S_1^2}}{S_0^2} \qquad \frac{\partial DOLP}{\partial S_1} = \frac{S_1}{S_0 \sqrt{S_0^2 + S_1^2}} \qquad \frac{\partial DOLP}{\partial S_2} = \frac{S_2}{S_0 \sqrt{S_0^2 + S_1^2}}$$

Following the rules of propagation of uncertainty for normally distributed errors, we get for the error of the DOLP $\sigma_{DOLP} = 0.0982$. The actual noise in the DOLP amounts to $\sigma_{dolp} = 0.0852$. This shows that the noise does come from the lack of proper illumination. Therefore it is clear that the data quality can be increased significantly by increasing the power of illumination in future experiments.

Ring waves

A perturbing effect that appeared at the towing tank at the HSVA was the generation of ring waves. Figure 7.10 shows an example image of the phenomenon.

At the side of the tank a water drain channel was installed. To empty the water drain channel holes connect the channel with the tank. These holes were located just above the water surface

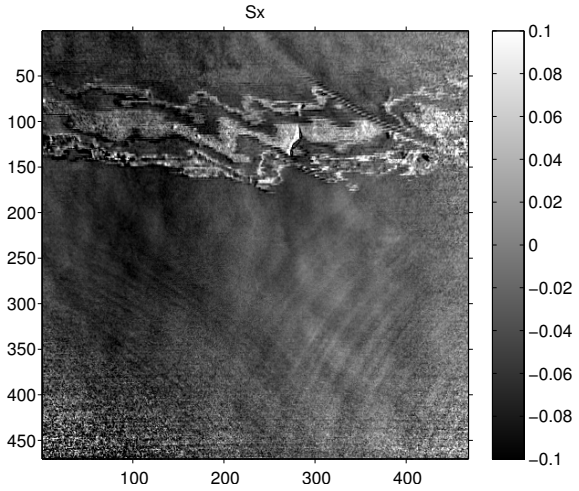

Figure 7.10.: Example image of ring waves shown in the X-component of the slope s_x of the series *HSVA15_001*.It can be recognized that the ring waves are coming from the side of the towing tank. (Main wave direction is in X-direction.)

when the water was calm. So, when a wave crest moved close some water flooded the holes. When the wave trough passed then the hole, the water was streaming out and generating some small scale ring waves. These ring waves will have an effect on the wave spectra, as one can see later. This is of importance since we want to compare the wave spectrum of the wave wire with that of the polarimeter and the wave wire was installed closer to the wave generator than the polarimeter (see Fig. 4.4).

Stereo Effect

Figure 7.11a shows an example image of degree of linear polarisation where all values that are larger than $DOLP > 1$ are marked in blue color. Because $DOLP > 1$ is unphysical, the error must come from the data analysis. A notable fact is that this defect is occurring especially where the reflected structure is very inhomogeneous. For investigation of this error a profile was taken in x-direction at the same position in the DOLP-image and in the image which was mapped already (Fig. 7.11b). The position of the profile is indicated by a red line in the images.

Figure 7.12 shows the result of both profiles of DOLP and the mapped images. By comparison of the two profiles it it is noticeable that DOLP decreases when the blue profile decrease and it increases when the green line is decreasing. Hence if the two dips of the blue and the green image profiles would coincide, DOLP were not too high.

As mentioned in the discussion of the *Meteor* data (see Sec. 7.1) a stereo effect arise due to the design of the polarimeter, with a stereo basis of 3.5 cm from one camera to the next one. Since we have mapped the images with a perspective transformation onto the water surface, the parallax was artificially set to zero at the water surface. The reflected background is therefore far away from the cameras. A parallax shift can be recognized in the images, if the reflection background is inhomogeneous. This effect is inherent in the simple polarimeter design, but its consequences can be eliminated by making the illuminated area as homogeneous as possible.

7.2.3. Slope Images

The primary result of the polarimeter is the degree of linear polarisation (DOLP) and the polarization angle Φ (see Sec. 6.5). An example image of each is shown in Fig.7.3 and 7.6. These results were then converted to the slope in X- and Y-direction (s_x, s_y) (see Sec. 3.1) with Eq.(3.11).

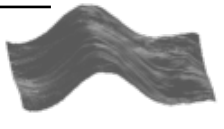

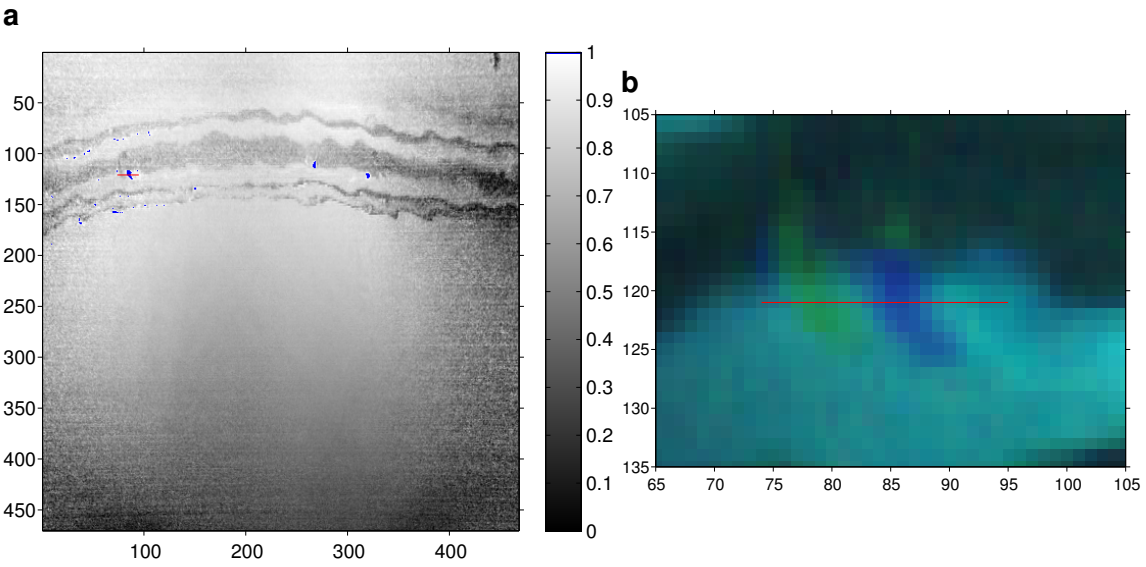

Figure 7.11.: **a** Example image of DOLP where all areas with $DOLP > 1$ are marked with blue color. **b** A detail of the same image of the 3 cameras in RGB color coding, mapped at the water surface. The red lines in both images indicate the position of the profile taken there. (see Fig. 7.12)

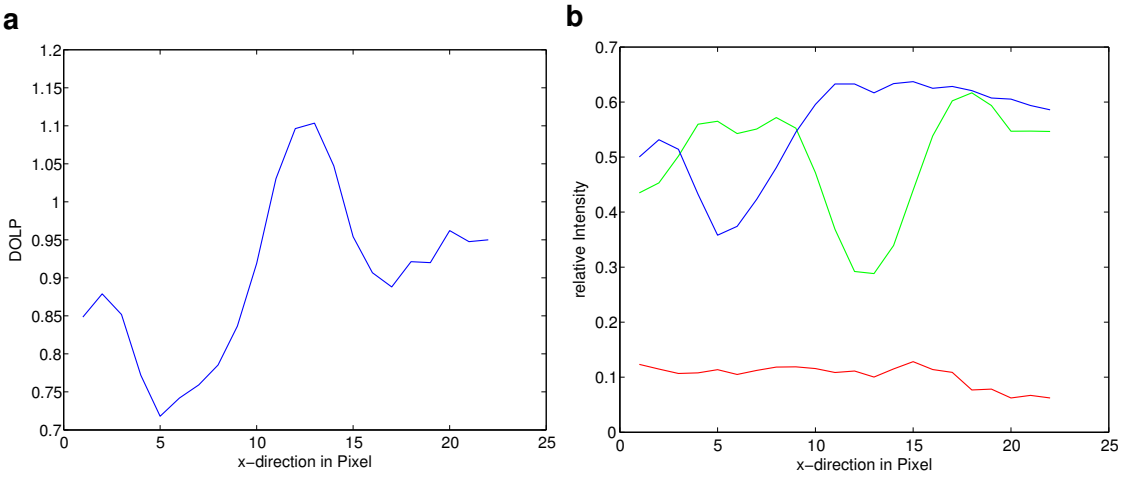

Figure 7.12.: Profiles of **a** DOLP and **b** mapped image in RGB color coding, which is taken from Fig. 7.11

Figure 7.4 and Fig.7.7 show the result of the conversion respectively.

As one can see with the naked eye the the slope in X-direction s_x is determined by the polarization angle Φ much more than by degree of linear polarisation and vise versa for slope in Y-direction s_y. This result shows obvious that the incidence angle θ, specified from DOLP, is the main factor for the Y-Component of the slope s_y. Thus the resolution in Y-direction is limited to a range from $\theta = 0° - 53°$, which corresponds to a slope from 0.0 to 1.3, due to conversion from DOLP to θ.

7.2.4. Height Reconstruction

Figure 7.5 and Fig. 7.8 show an example of the reconstructed height in a 3D representation. Noticeable is the smoothness of the reconstructed height although there has been a lot of noise in the corner of the images (see Sec. 7.2.2). This noise is diminished by the integration of the slope (see Sec. 3.4). The correct mean value can be achieved by integration, if the noise scatters Gaussian around this mean value. The smooth result of the height reconstruction demonstrates the

quality of the polarimetric slope imaging results.

As mentioned in Sec. 7.2.2 the degree of linear polarisation is sometimes larger than one (DOLP > 1). At the conversion from DOLP to the incidence angle θ all DOLP values above one will be set to *NaN*. Because the Fourier transformation in the height reconstruction routine cannot deal with *NaNs*, the areas with *NaNs* in the slope images (s_x, s_y) have to be corrected first. This can be done in two ways. The simple way is to set all *NaNs* to zero. This means that the height will remain on the same level where the slope is set to zero. Another approach is depicted in Sec. 6.6.1, where the *NaN* areas are filled up by an reconstruction algorithm. A comparison of the two *NaN* correction methods will be discussed in this section. The first method will be referred to as "*NaN* = 0" and the other one as "*NaN* reconstruction". Figure 7.13a depicts a reconstructed elevation map of the water surface with *NaN* reconstruction and Fig. 7.13b shows a detail image of the height difference with and without *NaN* reconstruction. The red line indicates the position where a profile was taken from the images.

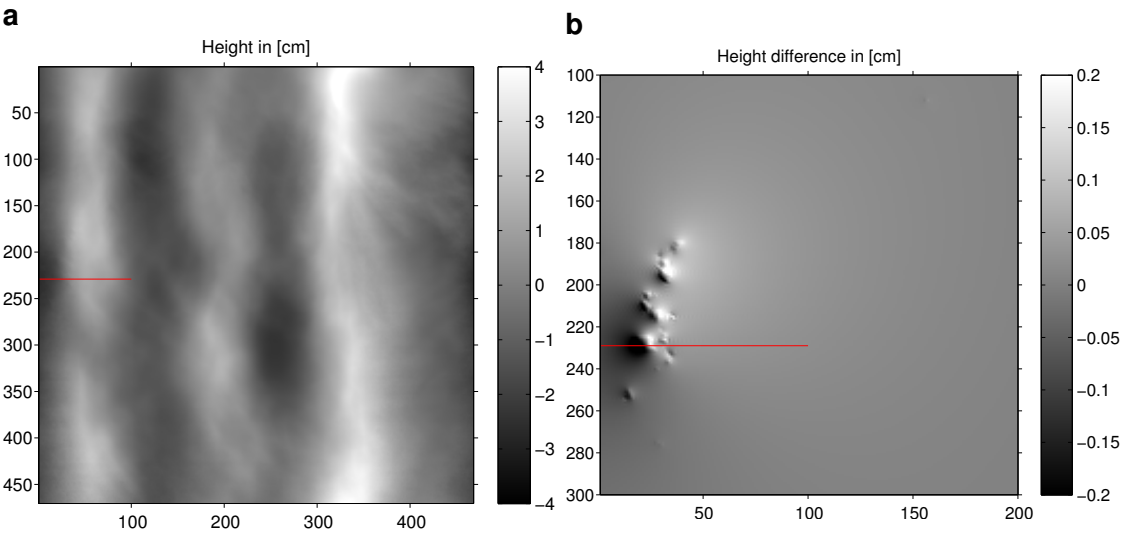

Figure 7.13.: **a** Example image of the series *HSVA15_001* of the Height with *NaN* reconstruction. **b** Detail of the height difference between the two height reconstructions, with different *NaN* corrected slopes. The red line indicates where a profile was taken (see Fig.7.15a)

To understand what is happening, one has to consider the slope images with the two different *NaN* correction methods. This is depicted in Figure 7.14. The difference in the two methods is quite prominent, since in the slope image with *NaN* = 0 the defects are easily visible, whereas in the images with *NaN* reconstruction they are not.

Figure 7.15a shows a profile of the two different height distribution, calculated with different *NaN* corrected slope images. It can be seen that the blue curve with the *NaN* reconstruction is much smoother and hence more physical than the curve where the *NaNs* in the slope image were set to zero. Figure 7.15 shows the corresponding profile of the X-slope image, where the two methods become obvious. The blue and the red curve are the same except for the *NaN* part, where the red curve is set to zero and the blue curve is continuing quite smoothly. The effect of the zero part in the red slope curve can also be seen in the red height curve as a bend to the horizontal. This is evident since a slope of zero is equal to no change in height.

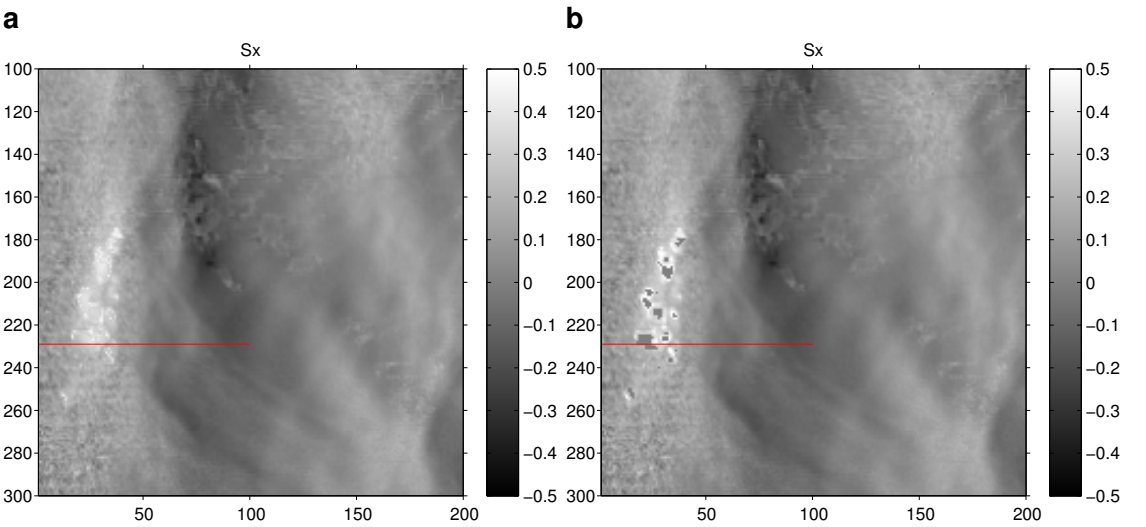

Figure 7.14.: Detail image of the slope in X-direction s_x **a** with *NaN* reconstruction and **b** with *NaN* = 0. The red line indicates the position of the profile that is shown in Fig. 7.15b.

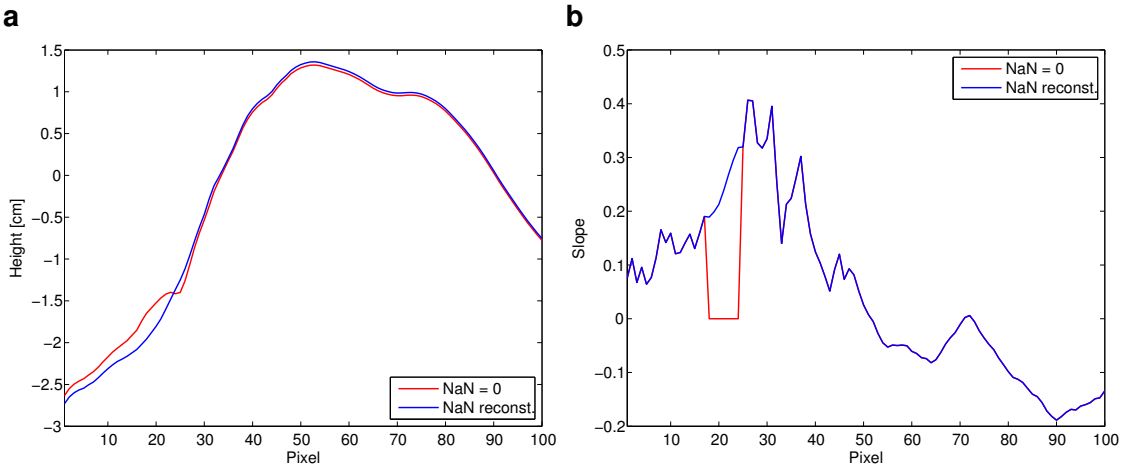

Figure 7.15.: **a** Profile of the two different height distributions, calculated from different *NaN* corrected slope images. **b** Profile of two slope images with the two different *NaN* correction methods.

7.2.5. Monochromatic Height Spectra

At the towing tank a wave wire was installed (see Sec. 4.5.1) for comparison reasons. To compare the data from the polarimeter with the wave wire, height power spectra were computed. The height power spectra of the polarimeter are computed as the mean of time series for every pixel of an area of interest. This area of interest, reaching from $x = 120\,\text{px} - 370\,\text{px}$ and $y = 220\,\text{px} - 340\,\text{px}$, was set to avoid errors from the missing illuminations in the corners (see Sec. 7.2.2) or from the stereo effect where the background was inhomogeneous (see Sec. 7.2.2). For a better comparability the data from the wave wire was resampled from 1000 Hz to the same frequency as the polarimeter (25 Hz). The same time range as for the polarimeter was chosen before the height power spectra of the wave wire were computed. Figure 7.16 and Fig. 7.17 show a height power spectrum of the wave wire compared to the polarimeter for the series *HSVA15_001* and the series *HSVA15_002*, respectively.

The measurements fit quite well above 0.9 Hz. Below this range the polarimeter underestimates the energy, especially at the peak frequency of 0.5 Hz. This is because the wavelength below 0.9 Hz (the corresponding wavelength is > 1.9 m) becomes longer than the length of the imaged water surface area of the polarimeter (see Tab. 4.5). This effect can be seen even for

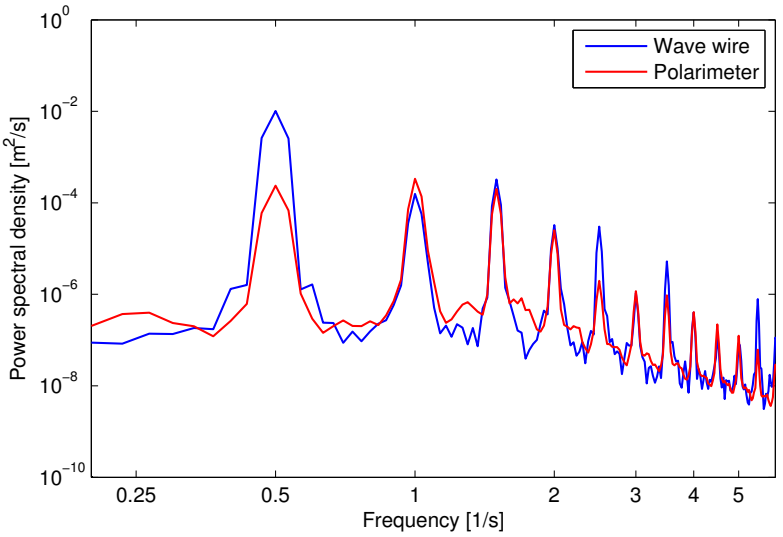

Figure 7.16.: Measurement *HSVA15_001* (monochromatic waves): Comparison of the spectrum from the polarimeter and the wave wire.

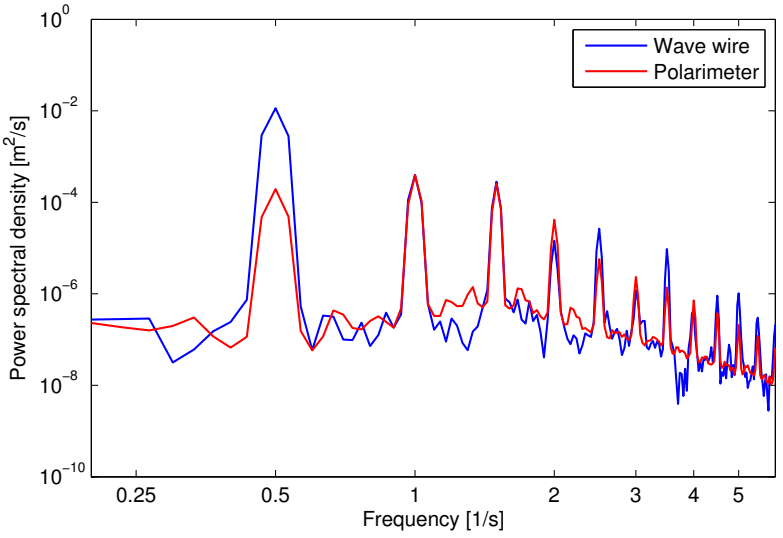

Figure 7.17.: Measurement *HSVA15_002* (monochromatic waves): Comparison of the spectrum from the polarimeter and the wave wire.

shorter wave lengths. Since the height distribution is computed from the slope distribution (see Sec. 6.6) the mean height is lost with this method. Waves cannot be measured if the assumption, that the mean wave height is zero in every image, is not valid. This effect is responsible for the underestimation of the energy below 0.9 Hz.

Figure 7.18 shows the power spectrum of monochromatic waves for two polarimeter series (*HSVA15_001, HSVA15_002*), where the first one was taken about 130 s before the second one.

Although the second time sequence (*HSVA15_002*) matches with the wave wire very well, the energy above 2.5 Hz is increased in the second sequence compared to the first one. This situation is depicted in Fig. 7.18. However it should be noted that in this frequency band there is hardly any energy and therefore the deviations are very small in total. The additional energy in the high frequency range comes from disturbances, which develop over time with the propagating waves. These disturbances could come from an inhomogeneity in the wave generation, from the already discussed ring waves or from reflections of the waves at the end of the tow-

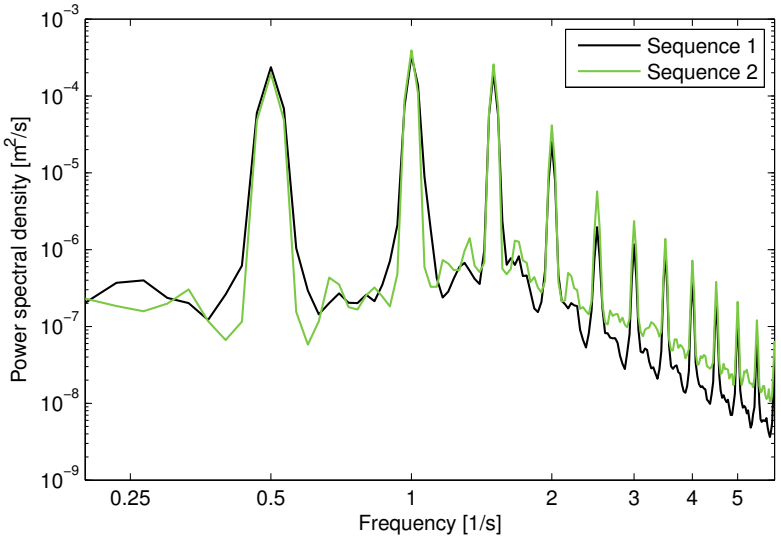

Figure 7.18.: Spectra from two sequences of the measurement *HSVA15*, where the first sequence was taken before the second one. A clear rise of the energy at higher frequencies can be seen.

ing tank. Since this effect evolves with time and can be seen in the wave wire data, it is a real physical effect and not an error in the data processing chain of the polarimeter.

7.2.6. Continuous Height Spectra

A continuous wave spectrum was generated by combining many waves with different frequencies and random phase relations. Figure 7.19 and Fig. 7.20 demonstrate the comparison of a wave wire spectrum with a polarimeter spectrum of the series *HSVA16_001* and the series *HSVA16_002* respectively. The continuous spectra were computed with logarithmically spaced bins (Tröbs and Heinzel, 2006) to obtain a smoother curve for the higher frequency range.

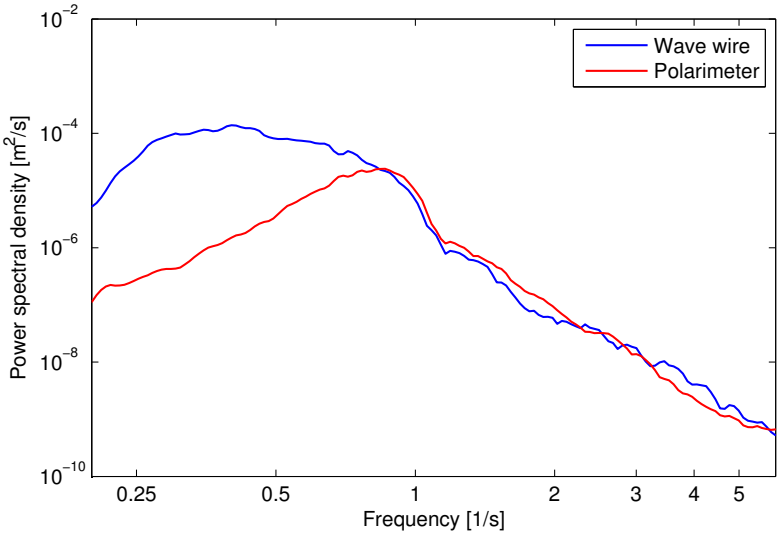

Figure 7.19.: Continuous wave spectra of the series *HSVA16_001* of wave wire and polarimeter. The incline below 0.9 Hz becomes obvious.

As seen in Fig. 7.19 and Fig. 7.20 the continuous spectra show the same attitude below 0.9 Hz as the monochromatic spectra Fig. 7.16 and Fig. 7.17. This effect was already discussed in the previous section 7.2.5. There is evidence that 0.9 Hz is the lower limit of the polarimeter due to

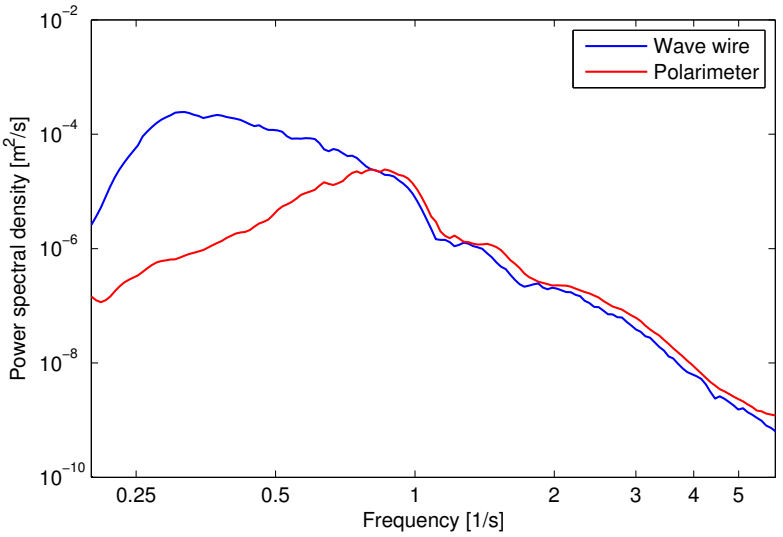

Figure 7.20.: Continuous wave spectra of the series *HSVA16_002* of wave wire and polarimeter. The incline below 0.9 Hz becomes obvious.

the area of interest at the water. Above this limit the spectrum of the polarimeter fits quite well to the spectrum of the wave wire.

In Fig. 7.20 the energy of the polarimeter spectrum is slightly increased for the higher frequencies compared to the wave wire spectrum. This effect can be seen in almost all continuous spectra from the second measurement series. Therefore is seems likely that increase comes from the disturbances of ring waves or the reflection of the waves at the end of the towing tank.

Figure 7.21 shows the same behavior as Fig. 7.18, but with a continuous wave spectrum. The first sequence (*HSVA16_001*) was taken about 130 s before the second sequence (*HSVA16_002*).

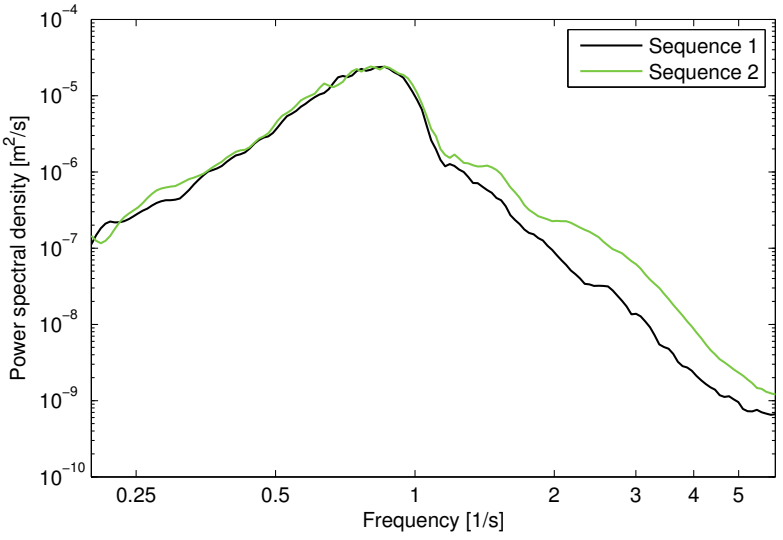

Figure 7.21.: Comparison of two spectra of the same series (*HSVA16*) but from different sequences. The build up of the high frequency disturbances over time is observable here.

For the continuous spectrum the consequence of the build up of the small scale waves is enforced due to the interference of many different wave lengths. Therefore the influence of the increase of the small scale waves over time can be seen clearly in the comparison of the two sequences in Fig. 7.21.

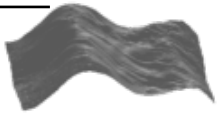

7.2.7. Polarimeter Characteristics

As discussed already in the previous sections the polarimeter has some immanent properties, which are given by the setup and the monitored water surface area. There are some external characteristics as well which result from the position at the towing tank and the disturbing effects on waves from ring waves, surface films or reflections of the water waves. To isolate these effects is very hard. Yet it is possible to determine the characteristics or transfer function of the polarimeter for this setup.

The transfer function of the polarimeter is obtained by dividing the many continuous wave spectra from the polarimeter by the corresponding wave spectra of the wave wire. This was done for nine continuous logarithmic spectra. The mean of these nine spectra can be seen in Fig. 7.22.

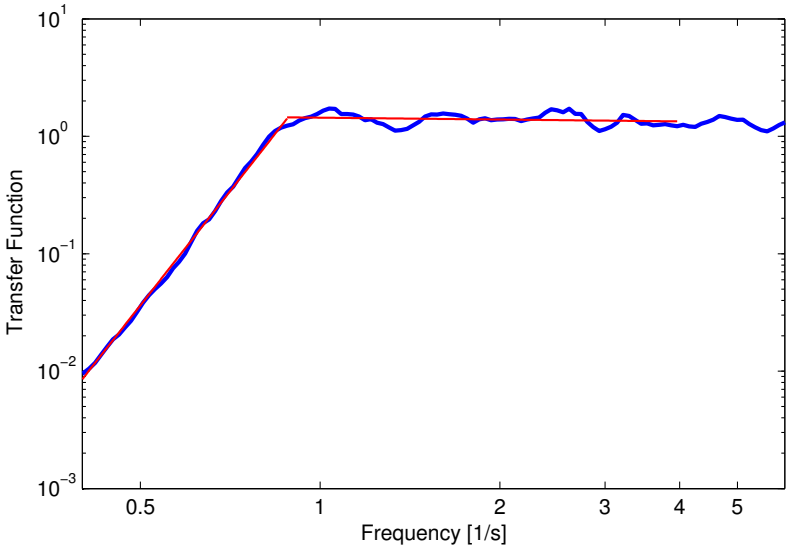

Figure 7.22.: Response function of the polarimeter at the towing tank. The response function was calculated by the mean of nine continuous spectra. The polarimeter shows a filtering behavior below the cutoff frequency of 0.88 Hz. The cutoff frequency was determined as intersection of the two red lines fitted to the transfer function.

Figure 7.22 shows the response of the polarimeter in Fourier space. The cutoff at 0.88 Hz is explicitly visible by the roll-off below this frequency. This decrease could be corrected by measuring the long scale waves, which could be done by combining height measurements with the polarimeter data. It is sufficient to know the height information at one known point in a polarimeter image to correct the lost mean height which is lost due to integration.

It is possible to apply the transfer function to the monochromatic spectrum, like in Fig. 7.16. Figure 7.23 shows a polarimeter spectrum corrected with the response function. Since the response function is calculated with the continuous spectra, the correction is independent of the monochromatic spectrum.

As expected, with the correction the spectra fit quite well even at the main peak at 0.5 Hz.

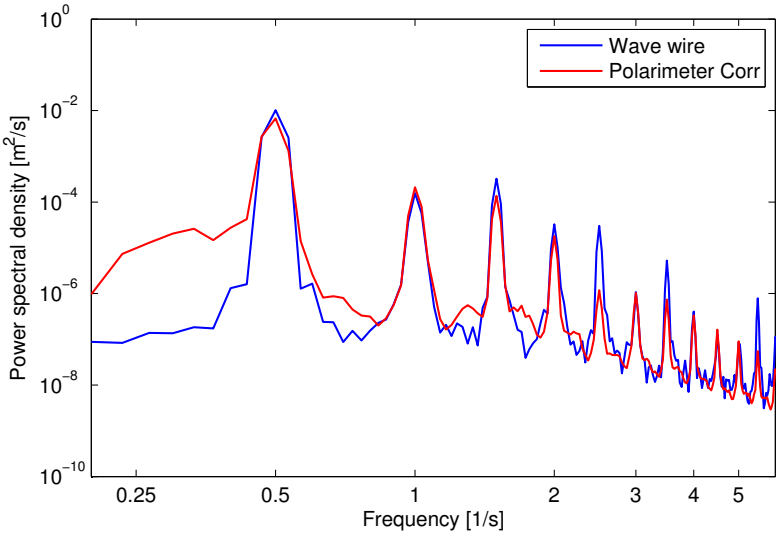

Figure 7.23.: Spectrum of the series *HSVA15_001* (see Fig. 7.16). The spectrum of the polarimeter is corrected by the response function of the polarimeter which was calculated independently of this spectrum.

8. Conclusion and Outlook

8.1. Conclusion

The approach of this thesis was to develop a simple polarimetric slope sensing instrument for water waves. Unlike common imaging polarimeters, where multiple cameras share a single custom lens, it consists of three cameras aligned in parallel, each equipped with a polarization filter and a standard lens (Sec. 4.2).

Due to the simple setup additional expenses have to be paid in the image processing part. Especially the calibration of the intrinsic, extrinsic, and distortion camera parameters (Sec. 5) was one of the key points for successful measurements. Since three images have to be mapped onto each other with a projective transformation (Sec. 6.4), the correction of the distortion from the lenses was crucial, see Sec. 5.4.4. To gain the intrinsic and distortion parameters of the cameras, a special calibration procedure with a custom built target was performed, see Sec. 5.5.The heart of the polarimeter is the analyzer matrix (Sec. 3.1), which transforms the incoming intensities into the parameters of the Stokes vector (Sec. 2.2.2). The calibration of the analyzer matrix (Sec. 5.6) was verified in a specifically designed inclination test (see Sec. 5.6.1).

The polarimeter was deployed to two experiments (Sec. 4.1 and 4.4) where its capabilities were tested. The instrument was collecting data during the M91 cruise on board of the German research vessel *Meteor*. While the full evaluation of this data set is beyond the scope of this thesis, an analysis of the polarimetric slope imaging measurements is presented in Sec. 7.1. The second experiment was conducted at the small towing tank at the Hamburgische Schiffsbau-Versuchsanstalt (HSVA) in Hamburg. This tank is equipped with a mechanical wave generator and a wave wire for reference measurements (see Sec. 4.5.1). The polarimeter was modified to fit the needs of laboratory measurements (Sec. 4.5).

The capabilities of the polarimeter in capturing the slope distribution of mechanically generated waves are demonstrated (Sec. 7.2). The necessity of a powerful illumination and perturbations of the measurements due to imperfections of the laboratory setup are discussed (Sec. 7.2.2). The effect of data gaps on the reconstruction of surface elevation (wave height) from the measured wave slope is discussed and different approaches are compared (Sec. 7.2.4).

Comparative measurements of the polarimeter with the wave wire are presented both for nearly monochromatic waves (Sec. 7.2.5) and for continuous spectra consisting of a random superposition of waves with different frequencies (Sec. 7.2.6). Wave height power spectra computed from the polarimeter data are shown to agree with reference measurements for wave frequencies above 0.9 Hz. Since longer waves have wavelengths comparable to the dimensions of the footprint of the polarimeter, their mean height is no longer zero at all times as was assumed in the height reconstruction. This leads to a sharp cutoff in the transfer function of the polarimeter (see Sec. 7.2.7). The derived transfer function can be applied to correct measured spectra, allowing the polarimeter to measure waves for a wide range of frequencies.

8.2. Outlook

The simple design of the imaging polarimeter presented in this thesis allows for building inexpensive measurement instruments. The trade-off is the inherent stereo disparity, which causes problems especially for shipborne measurements in which the relative variations of the distance to the water surface are large. To avoid the use of an expensive custom lens (as described by Pezzaniti et al. (2009)), the three cameras could be placed behind a system of beam splitters so they are virtually placed in the same position.

The experiences with the polarimeter during the M91 cruise show, that it is crucial to include measurements of the polarization of the sky in the data processing scheme to reduce the constraints on environmental conditions under which the polarimeter can operate.

Apart from its potential to measure small-scale waves on the ocean, an imaging polarimeter might also be useful in other scientific disciplines, e.g. the inspection of clouds (Pust and Shaw, 2006), the sky (Lee, 1998) or the detection of volcanic plumes (Sassen et al., 2007). In all these areas, the strength of the polarimeter technique, to make the normally invisible polarization visible, could gain new insights into the mysteries of our world.

Bibliography

G. Balschbach. *Untersuchungen statistischer und geometrischer Eigenschaften von Windwellen und ihrer Wechselwirkung mit der wasserseitigen Grenzschicht.* Dissertation, Institut für Umweltphysik, Fakultät für Physik und Astronomie, Univ. Heidelberg, 2000.

P. Barsic and C. Chinn. Sea surface slope recovery through passive polarimetric imaging. In *Oceans, 2012*, pages 1–9, 2012.

A. Benetazzo. Measurements of short water waves using stereo matched image sequences. *Coastal Engineering*, 53(12):1013–1032, Dec. 2006.

J.-Y. Bouguet. Camera calibration toolbox for matlab, http://www.vision.caltech.edu/bouguetj/calib_doc/. 2008.

C. Brosseau. *Fundamentals of polarized light.* A Wiley-Interscience publication. Wiley, New York [u.a.], 1998. Includes indexes.

M. Daimon and A. Masumura. Measurement of the refractive index of distilled water from the near-infrared region to the ultraviolet region. *Appl. Opt.*, 46(18):3811–3820, Jun 2007.

M. A. Donelan, J. Hamilton, and W. H. Hui. Directional spectra of wind-generated waves. *Royal Society of London Philosophical Transactions Series A*, 315:509–562, Sept. 1985.

M. A. Donelan and R. Wanninkhof. Gas transfer at water surfaces - conepts and issues. In M. A. Donelan, W. M. Drennan, E. S. Saltzman, and R. Wanninkhof, editors, *Gas Transfer at Water Surfaces*. American Geophysical Union, 2002.

D. A. Forsyth and J. Ponce. *Computer Vision: A Modern Approach.* Prentice Hall, 2002.

R. T. Frankot and R. Chellappa. A method for enforcing integrability in shape from shading algorithms. *IEEE Trans. Pattern Anal. Mach. Intell.*, 10(4):439–451, 1988.

N. M. Frew, E. J. Bock, U. Schimpf, T. Hara, H. Haußecker, J. B. Edson, W. R. McGillis, R. K. Nelson, B. M. McKeanna, B. M. Uz, and B. Jähne. Air-sea gas transfer: Its dependence on wind stress, small-scale roughness, and surface films. *J. Geophys. Res.*, 109:C08S17, 2004.

D. Fuß. *Kombinierte Höhen- und Neigungsmessung von winderzeugten Wasserwellen am Heidelberger Aeolotron.* Dissertation, Institut für Umweltphysik, Fakultät für Physik und Astronomie, Univ. Heidelberg, Heidelberg, Germany, 2004.

H. Haferkorn. *Optik.* Johann Ambrosius Barth, Leipzig, 3 edition, 1994.

R. Hartley and A. Zisserman. *Multiple View Geometry in Computer Vision.* Cambridge Univ Press, 2 edition, 2003.

J. Heikkilä and O. Silven. A four-step camera calibration procedure with implicit image correction. In *IEEE Conference on Computer Vision and Pattern Recognition*, pages 1106–1112, 1997.

G. Horváth, A. Barta, J. Gál, B. Suhai, and O. Haiman. Ground-based full-sky imaging polarimetry of rapidly changing skies and its use for polarimetric cloud detection. *Appl. Opt.*, 41(3): 543–559, Jan 2002.

J. D. Jackson. *Classical Electrodynamics*. Wiley, 3rd edition, 1998.

B. Jähne. *Digital Image Processing*. Springer, Berlin, 6 edition, 2005.

B. Jähne, P. Geißler, and H. Haußecker, editors. *Handbook of Computer Vision and Applications*. Academic Press, San Diego, 1999.

B. Jähne, J. Klinke, and S. Waas. Imaging of short ocean wind waves: a critical theoretical review. *J.Opt.Soc.Am.*, 11:2197–2209, 1994.

B. Jähne, K. O. Münnich, R. Bösinger, A. Dutzi, W. Huber, and P. Libner. On the parameters influencing air-water gas exchange. *J. Geophys. Res.*, 92:1937–1950, Feb. 1987.

G. Kattawar and C. Adams. Stokes vector calculations of the submarine light field in an atmosphere-ocean with scattering according to a rayleigh phase matrix: effect of interface refractive index on radiance and polarization. *Limnology and oceanography*, 34(8):1453–1472, 1989.

D. Kiefhaber, R. Rocholz, and B. Jähne. Improved optical instrument for the measurement of water wave statistics in the field. In S. Komori, W. McGillis, and R. Kurose, editors, *Gas Transfer at Water Surfaces 2010*, pages 524–534, 2011.

R. L. Lee. Digital imaging of clear-sky polarization. *Appl. Opt.*, 37(9):1465–1476, Mar 1998.

M. S. Longuet-Higgins, D. E. Cartwright, and N. D. Smith. Observations of the directional spectrum of sea waves using the motions of a floating buoy. In *Ocean Wave Spectra, proceedings of a conference, Easton, Maryland*, pages 111–136. National Academy of Sciences, Prentice-Hall, 1963.

T. Luhmann. *Nahbereichsphotogrammetrie: Grundlagen, Methoden und Anwendungen*. Wichmann, Heidelberg, 3 edition, 2010.

J. L. Pezzaniti, D. Chenault, M. Roche, J. Reinhardt, J. P. Pezzaniti, and H. Schultz. Four camera complete Stokes imaging polarimeter. In *Polarization: Measurement, Analysis, and Remote Sensing VIII*, volume 6972 of *SPIE Proc.*, page 69720J, 2008.

J. L. Pezzaniti, D. Chenault, M. Roche, J. Reinhardt, and H. Schultz. Wave slope measurement using imaging polarimetry. In *Ocean Sensing and Monitoring*, volume 7317 of *SPIE Proc.*, page 73170B, 2009.

N. Pust and J. A. Shaw. Imaging spectropolarimetry of cloudy skies. *Proc. SPIE*, 6240:624006–624006–5, 2006.

R. Rocholz. *Spatiotemporal Measurement of Short Wind-Driven Water Waves*. Dissertation, Institut für Umweltphysik, Fakultät für Physik und Astronomie, Univ. Heidelberg, 2008.

K. Sassen, J. Zhu, P. Webley, K. Dean, and P. Cobb. Volcanic ash plume identification using polarization lidar: Augustine eruption, alaska. *Geophysical Research Letters*, 34(8):n/a–n/a, 2007.

U. Schimpf, L. Nagel, and B. Jähne. First results of the 2009 sopran active thermography pilot experiment in the baltic sea. In S. Komori, W. McGillis, and R. Kurose, editors, *Gas Transfer at Water Surfaces 2010*, pages 358–367, 2011.

J. R. Schott. *Fundamentals of Polarimetric Remote Sensing*. SPIE Press, 2009.

A. Schumacher. Stereophotogrammetrische wellenaufnahmen. *Wissenschaftliche Ergebnisse der Deutschen Atlantischen Expedition auf dem Forschungs- und Vermessungsschiff Meteor*, 1925 - 1927, 1939.

D. J. Stilwell. Directional energy spectra of the sea from photographs. *J.Geophys.Res.*, 74:1974–1986, 1969.

R. Szeliski. *Computer Vision Algorithms and Applications*. Springer, London, 2011.

M. Tröbs and G. Heinzel. Improved spectrum estimation from digitized time series on a logarithmic frequency axis. *Measurement*, 39(2):120 – 129, 2006.

E. Trucco and A. Verri. *Introductory Techniques for 3D Computer Vision*. Prentice Hall, Upper Saddle River, New Jersey, 1998.

R. Y. Tsai. A versatile camera calibration technique for high-accuracy 3D machine vision metrology using off-the-shelf tv cameras and lenses. *IEEE journal of Robotics and Automation*, 3(4): 323–344, 1987.

G. Videen, Y. Yatskiv, and M. Mishchenko. *Photopolarimetry in Remote Sensing*. NATO Science Series II: Mathematics, Physics and Chemistry ; 161 ; SpringerLink : Bücher. Springer Netherlands, Dordrecht, 2005.

C. Zappa, M. Banner, H. Schultz, A. Corrada-Emmanuel, L. Wolff, and J. Yalcin. Retrieval of short ocean wave slope using polarimetric imaging. *Meas. Sci. Technol.*, 19:055503 (13pp), 2008.

C. J. Zappa, M. L. Banner, H. Schultz, J. Gemmrich, R. P. Morison, D. LeBel, and T. Dickey. An overview of sea state conditions and air-sea fluxes during RaDyO. *J. Geophys. Res., Oceans*, 117:C00H19, 2012.

X. Zhang. An algorithm for calculating water surface elevations from surface gradient. *Experiments in Fluids*, 21:43–48, 1996.

Z. Zhang. A flexible new technique for camera calibration. Technical Report MSR-TR-98-71, Microsoft, Redmond, WA, USA, 1998.

Z. Zhang. A flexible new technique for camera calibration. *IEEE Transactions on Pattern Analysis and Machine Intelligence*, 22(11):1330–1334, November 2000.

W. Zinth and U. Zinth. *Optik*. Oldenbourg, München, 4., aktualisierte auflage edition, 2013.

A. Appendix

A.1. Rotation Matrices

In this thesis this convention for rotational matrices is used.

1. Rotation around the Z-axis with the angle κ

$$\boldsymbol{X} = \boldsymbol{R}_\kappa \cdot \boldsymbol{x}$$
$$\begin{bmatrix} X \\ Y \\ Z \end{bmatrix} = \begin{bmatrix} \cos\kappa & -\sin\kappa & 0 \\ \sin\kappa & \cos\kappa & 0 \\ 0 & 0 & 1 \end{bmatrix} \cdot \begin{bmatrix} x \\ y \\ z \end{bmatrix} \tag{A.1}$$

2. Rotation around the Y-axis with the angle φ

$$\boldsymbol{X} = \boldsymbol{R}_\varphi \cdot \boldsymbol{x}$$
$$\begin{bmatrix} X \\ Y \\ Z \end{bmatrix} = \begin{bmatrix} \cos\varphi & 0 & \sin\varphi \\ 0 & 1 & 0 \\ -\sin\varphi & 0 & \cos\varphi \end{bmatrix} \cdot \begin{bmatrix} x \\ y \\ z \end{bmatrix} \tag{A.2}$$

3. Rotation around the X-axis with the angle ω

$$\boldsymbol{X} = \boldsymbol{R}_\omega \cdot \boldsymbol{x}$$
$$\begin{bmatrix} X \\ Y \\ Z \end{bmatrix} = \begin{bmatrix} 1 & 0 & 0 \\ 0 & \cos\omega & -\sin\omega \\ 0 & \sin\omega & \cos\omega \end{bmatrix} \cdot \begin{bmatrix} x \\ y \\ z \end{bmatrix} \tag{A.3}$$

In general rotation matrices are orthonormal, which means:

$$\boldsymbol{R} \cdot \boldsymbol{R}^T = \boldsymbol{R}^T \cdot \boldsymbol{R} = \boldsymbol{I} \qquad \boldsymbol{R}^{-1} = \boldsymbol{R}^T \qquad und \qquad \det(\boldsymbol{R}) = 1 \tag{A.4}$$

A general rotation can be described as a rotation first around the Z-axis, then the Y-axis and at last the X-axis. This gives for the general rotation matrix:

$$\boldsymbol{R} = \boldsymbol{R}_\omega \cdot \boldsymbol{R}_\varphi \cdot \boldsymbol{R}_\kappa = \begin{bmatrix} r_{11} & r_{12} & r_{13} \\ r_{21} & r_{22} & r_{23} \\ r_{31} & r_{32} & r_{33} \end{bmatrix}$$
$$= \begin{bmatrix} \cos\varphi\cos\kappa & -\cos\varphi\sin\kappa & \sin\varphi \\ \cos\omega\sin\kappa + \sin\omega\sin\varphi\cos\kappa & \cos\omega\cos\kappa - \sin\omega\sin\varphi\sin\kappa & -\sin\omega\cos\varphi \\ \sin\omega\sin\kappa - \cos\omega\sin\varphi\cos\kappa & \sin\omega\cos\kappa + \cos\omega\sin\varphi\sin\kappa & \cos\omega\cos\varphi \end{bmatrix} \tag{A.5}$$

The rotation angles can be determined by the coefficients of the rotation matrix $\boldsymbol{R}$.

$$\begin{aligned} \sin\varphi &= r_{13} \\ \tan\omega &= -\frac{r_{23}}{r_{33}} \\ \tan\kappa &= -\frac{r_{12}}{r_{11}} \end{aligned} \quad \text{or} \quad \begin{aligned} \sin\varphi &= r_{13} \\ \cos\omega &= \frac{r_{33}}{\cos\varphi} \\ \cos\kappa &= \frac{r_{11}}{\cos\varphi} \end{aligned} \tag{A.6}$$

A.2. Target in Hanau

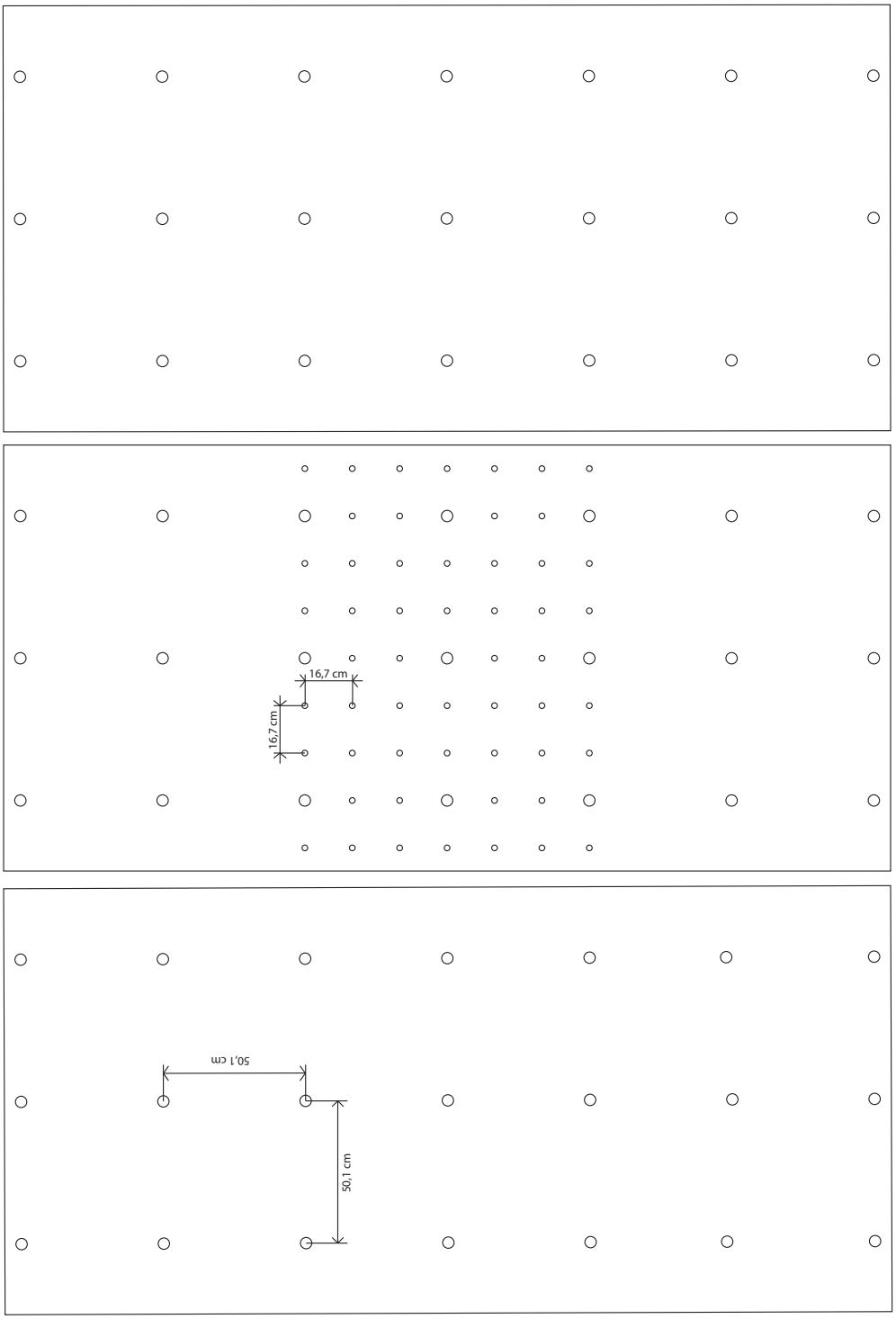

Figure A.1.: 2D-drawing of the target in Hanau for the geometric calibration

A.3. Intrinsic Parameters

The intrinsic parameters where calculated with the *Camera Calibration Toolbox for Matlab* (Bouguet, 2008). Table A.1 shows all parameters for the setup in Hamburg, table A.2 shows all parameters for the setup at the *Meteor*. The specifications of the different setups with pixel size and lens properties can be found in Tab. 4.5 for the Hamburg setup and in Tab. 4.3 for the *Meteor*setup.

Table A.1.: All important parameters of the *Camera Calibration Toolbox for Matlab* for the setup in Hamburg

		buf1A	buf1B	buf1C
Image Size	N_x	648	648	648
[pixel]	N_y	486	486	486
Focal length	f_x	895.55 ± 8.58	902.33 ± 9.09	900.45 ± 9.11
[pixel]	f_y	898.53 ± 8.74	904.41 ± 9.25	902.38 ± 9.26
Principal Point	cc_x	297.61 ± 8.41	296.61 ± 8.97	290.14 ± 9.04
[pixel]	cc_y	240.06 ± 7.41	250.61 ± 7.82	253.34 ± 7.75
Radial	$k1$	-0.22546 ± 0.01039	-0.22637 ± 0.01083	-0.22648 ± 0.01042
distortion	$k2$	0.09437 ± 0.05434	0.08929 ± 0.05449	0.09834 ± 0.04815
Tangential	$k3$	0.00063 ± 0.00089	0.00007 ± 0.00092	-0.00072 ± 0.00091
distortion	$k4$	-0.00139 ± 0.00088	-0.00183 ± 0.00093	-0.00277 ± 0.00094
Pixel	err_x	0.07688	0.08212	0.08937
error	err_y	0.23094	0.23628	0.23747

Table A.2.: All important parameters of the *Camera Calibration Toolbox for Matlab* for the setup at the *Meteor*

		buf0A	buf0B	buf0C	buf1A	buf1B	buf1C
Image Size	N_x	2592	2592	2592	2592	2592	2592
[pixel]	N_y	1944	1944	1944	1944	1944	1944
Focal length	f_x	7248.82 ± 8.56	7228.17 ± 8.18	7227.83 ± 8.33	7266.24 ± 8.24	7229.58 ± 8.20	7207.72 ± 8.29
[pixel]	f_y	7252.13 ± 8.57	7229.88 ± 8.18	7229.15 ± 8.34	7272.49 ± 8.26	7235.45 ± 8.22	7215.01 ± 8.32
Principal Point	cc_x	1203.79 ± 13.22	1181.97 ± 12.69	1172.29 ± 12.88	1161.67 ± 12.30	1201.99 ± 12.01	1214.14 ± 15.89
[pixel]	cc_y	1044.38 ± 10.66	1056.05 ± 9.95	1027.34 ± 10.49	1042.77 ± 10.16	1037.89 ± 8.79	1138.04 ± 8.97
Radial	$k1$	-0.14323 ± 0.00478	-0.16024 ± 0.00457	-0.14743 ± 0.00466	-0.17536 ± 0.00458	-0.18418 ± 0.00398	-0.17187 ± 0.00415
distortion	$k2$	0.00000 ± 0.00000	0.00000 ± 0.00000	0.00000 ± 0.00000	0.00000 ± 0.00000	0.00000 ± 0.00000	0.00000 ± 0.00000
Tangential	$k3$	-0.00392 ± 0.00035	-0.00389 ± 0.00032	-0.00412 ± 0.00034	-0.00504 ± 0.00030	-0.00598 ± 0.00026	-0.00489 ± 0.00029
distortion	$k4$	0.00665 ± 0.00040	0.00772 ± 0.00036	0.00642 ± 0.00039	0.00810 ± 0.00034	0.00893 ± 0.00028	0.00774 ± 0.00040
Pixel	err_x	0.47947	0.45109	0.46587	0.46208	0.49416	0.42433
error	err_y	0.51058	0.49252	0.49707	0.48969	0.52405	0.52919

Danksagung

Ich möchte mich ganz herzlich bei Prof. Dr. Bernd Jähne für die Betreuung dieser Arbeit bedanken. Es wurde mir ermöglicht an einer spannenden Messkampagne in Hamburg sowie an einer interessanten Kalibrierkampagne in der Studiohalle von AEON teilzunehmen. Vielen Dank!

Des Weiteren möchte ich mich für die freundliche Übernahme der Zweitkorrektur bei Herrn Priv.-Doz. Dr. Christoph S. Garbe bedanken.

Ein ganz großer Dank geht natürlich an die gesamte Arbeitsgruppe der "Windis" am IUP für die gute Atmosphäre, die netten Kaffeepausen, die hilfreichen wissenschaftlichen Diskussionen und die große Hilfsbereitschaft.

Bedanken möchte ich mich außerdem bei Roland Rocholz, der mir beim flotten Aufbau des Polarimeters tatkräftig und mit Sachverstand geholfen hat.

Ein großer Dank geht besonders an Leila Nagel, die zusammen mit Daniel Kiefhaber das Polarimeter auf der Meteor aufgebaut und betrieben hat.

Daniel Kiefhaber gebührt mein allergrößter Dank. Als betreuender Doktorand war er mir stets mit einem sehr großen Engagement zur Seite und half mir mit seiner Expertise. Trotzdem ließ er mir den nötigen Freiraum, so dass ich meine eigenen Ideen ausprobieren und so wichtige Erfahrungen im Bereich der Bildverarbeitung sammeln konnte. Er hat auch das Polarimeter auf der Meteor erfolgreich aufgebaut und betrieben. Des Weiteren half er mir bei der Planung und Durchführung der Messkampagne in Hamburg und der Kalibrierkampagne in Hanau. Dafür und für viele Kleinigkeiten, die hier leider keinen Platz finden, vielen Dank.

Zu guter Letzt möchte ich noch meiner Freundin, Svenja Reith, meinen Eltern, Maria und Franz Bauer, meinen Geschwistern, Benedikt, Mirjam und Teresa, meinen Freunden, Clemens Schwingshackl und Neta Tsur, von ganzen Herzen für die großartige Unterstützung in den letzten Monaten bedanken.

Allen, die mir bei meiner Arbeit geholfen haben und hier aber leider nicht explizit erwähnt sind, auch ein herzliches DANKE!

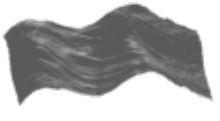

Erklärung:

Ich versichere, dass ich diese Arbeit selbstständig verfasst habe und keine anderen als die angegebenen Quellen und Hilfsmittel benutzt habe.

Heidelberg, den 4. November 2013 .....